UNIVERSITÀ
DEGLI STUDI
DI PADOVA

Head Office: Università degli Studi di Padova
CISAS - Center of Studies and Activities for Space “G. Colombo”

Ph.D. COURSE IN: SPACE SCIENCES, TECHNOLOGIES AND MEASUREMENTS
CURRICULUM: SCIENCES AND TECHNOLOGIES FOR AERONAUTIC AND SATELLITE APPLICATIONS
XXX SERIES

DYNAMICS AND CONTROL OF HIGHLY FLEXIBLE STRUCTURES FOR AEROSPACE APPLICATIONS

Coordinator: Prof. Giampiero Naletto
Supervisor: Prof. Alessandro Francesconi

Ph.D. student: Laura Bettiol

Abstract

Highly flexible space structures such as thin-film solar arrays, deployable antennas, solar concentrators, solar and drag sails, are typically made of very thin tensioned membranes. These deployable structures are considered promising technologies for their lightness, high deployed-to-packed volume ratio, and low cost. These advantages make them an extremely interesting technology for satellites of small classes, such as nanosatellites (including CubeSats) that are becoming more and more common because of their capability to provide many of the services that were performed by larger satellites in the past with a fraction of their cost. However, the size of deployable structures is not proportional to the dimension of the hosting satellite but depends on the specific mission and application. In addition, the miniaturization of satellites comes very often with the reduction of the performance of their attitude control system. Therefore, large appendages mounted on a nanosatellite can be an issue in terms of attitude control, with a possible reduction of the stability and pointing precision, or even the loss of the whole mission. For this reason, control systems must be envisaged in order both to limit or avoid the oscillations of these structures and to reduce the transmission of disturbing forces from the deployable appendage to the central body of the satellite.

This Ph.D. research is focused on the analysis of the dynamic behavior of highly flexible space structures, and the study of the effectiveness of possible methods to control their oscillations, both in terms of damping techniques directly applied to the appendage, and vibrations transmission reduction at the interface between the deployed structure and the main body of the satellite. Two test cases with completely different approaches were identified for this study, both based on solar arrays.

The *first test case* focuses on a membrane solar array not supported by an ex-

ternal structure. Numerical simulations explore the effectiveness of controlling the oscillations of this membrane, subject to a sinusoidal force and non-flat initial conditions with the use of thin patches of piezoelectric material. This study confirms the possibility to apply the robust H_∞ closed-loop control system, in order to correct the initial non-horizontal shape of the membrane to reach a flat deployed configuration.

The *second test case* studies the dynamics of a solar array structure that is deployed and kept in tension by two external composite tape springs. Bistable boom prototypes have been manufactured and their theoretical dynamic behavior is studied in detail. Numerical simulations and experimental tests focus on the analysis of the dynamics of the system and the exploration of possible control strategies in terms of active oscillations reduction directly applied to the appendage structure and passive vibration isolation between the deployed structure and the main body of the satellite. The main results confirm the concern that uncontrolled deployment of deployable appendages on a small spacecraft with limited attitude control capabilities exploiting only the stored strain energy of the tape springs can generate torques that can lead to uncontrolled rotations and mission failure. Hence, the dynamic behavior of controlled deployments using a small motor is studied and compared to the previously mentioned case. Although mass and complexity are added to the system, this approach brings many benefits such as disturbance reduction and the possibility of retracting the deployed structure whenever needed. Moreover, the effectiveness of two different strategies to control the oscillations of the booms is confirmed, respectively following a numerical and an experimental approach.

Summary

In these last decades highly flexible structures, also called *gossamer structures*, are gaining significant interest in the space field. Considered as one of the most promising structures that will make innovative space missions possible, these structures are being more and more used in various applications, such as thin-film solar arrays, deployable antennas, solar concentrators, solar and drag sails, etc. These structures are typically made of a very thin layer of material kept in tension by a supporting structure that is generally made of deployable or inflatable booms, telescopic structures or articulated mechanisms. Their ultra-low areal density makes them attractive for achieving high packaging efficiency, which is unattainable by other conventional structures. In addition, their lower mass with respect to traditional bulky structures makes their launch less expensive. These advantages make them an extremely interesting technology for satellites of small classes, such as nanosatellites (including CubeSats).

These satellites are becoming more and more common because of their capability to provide many of the services that were performed by larger satellites in the past. While the avionics and instruments have decreased in size in the past decades, with a tendency towards a general miniaturization of the spacecraft, deployable structures such as solar panels or antennas remain large, since their size does not vary with the dimension of the hosting satellite but depends on the specific mission and application. Nevertheless, with the miniaturization of satellites sizes there is a tendency to reduce the capabilities of the attitude control system, typically because of power or available volume limitations. Therefore, large appendages mounted on a small spacecraft can be an issue in terms of attitude control. For this reason, precautions must be taken in order to limit or avoid the oscillations of these structures to reduce

the transmission of disturbing torques from the deployable appendage to the central body of the satellite.

Two completely different test cases were identified for this study, both focusing on solar arrays structures. The first test case is based on a membrane solar panel that can provide up to 0.5-1 kW of power, while the second one considers a rollable and deployable solar wing with 0.3 m^2 of area.

This thesis is organized as follows: after an introduction to highly flexible structures in Chapter 1, the *first test case* is presented in Chapter 2, and the *second test case* is discussed in Chapters 3 and 4. Conclusions are given in Chapter 5.

In particular, Chapter 1 presents the state-of-the-art of gossamer space structures, with a focus on thin-film solar arrays, solar and drag sails, and antennas. Then, the thesis motivation and objectives as well as the two test cases are introduced. Finally, the thesis workflow is outlined to guide the reader throughout the work.

Chapter 2 presents the *first test case*, that focuses on a membrane solar array that can produce up to 0.5-1 kW of power. The aim of this chapter is to explore a possible strategy for controlling the oscillations on a membrane not supported by an external structure. First, an overview on piezoelectric materials is given to introduce their properties and capabilities when used as sensors and/or actuators. The following section presents the numerical simulations that demonstrate the feasibility to reduce the oscillations provoked by an external sinusoidal disturbance and non-flat initial conditions with the use of thin patches of piezoelectric material distributed on the surface of the panel. Results of the simulations confirmed the possibility to apply the robust H_∞ closed-loop control system, in order to correct the initial non-horizontal shape of the membrane to reach a flat deployed configuration. This first test case is based on previous studies carried out by the Author in the Master's thesis project, where the dynamic behavior of a large membrane subjected to Low Earth Orbit (LEO) typical disturbances was investigated.

Chapter 3 and 4 present the *second test case*, that focuses on a solar array of 0.3 m^2 of area deployed and kept in tension by two external composite tape spring booms. Tape spring booms are a structural element similar to tape measure that

presents two stable configuration of minimum energy: rolled up and deployed. The transformation between these two configurations takes place in a short transition zone that moves along the structure during the deployment and can be triggered adding a substantial amount of energy to the system, for example, by mechanical loading. These deployable elements are typically made with ultra-thin composite laminates, low weight materials that allow storage in a very small volume and provide good stiffness when in the deployed configuration. Firstly, the state-of-the-art of these structures is presented. Then, a mathematical description of the system is provided, with the computation of the ABD matrix for the specific material used for the actual prototypes used in the experimental tests and the calculation of physical quantities such as forces and torques experienced by these structures during their deployment. This first part of the work is based on the theory developed in particular by S. Pellegrino and his research group. Being these structures very complicated to mathematically model and being subjected to many variables that are difficult to control and predict such as viscoelastic relaxation of the material after long stowage time, friction and microcracks, three preliminary tests were carried out to study the actual properties of the prototypes in terms of elastic and damping characteristics, torques needed to be exerted by a motor to control the deployment of the booms and the torques transmitted to an external structure at the end of the deployment when a shock load occurs. The results of these preliminary tests were used in following numerical simulations and experimental tests. In particular, simulations of the dynamic behavior of a nanosatellite orbiting in LEO and subjected to typical environmental disturbances during the deployment of the solar panels are presented. Results for both controlled (slow and motorized) and uncontrolled deployment (fast, that exploits the strain energy of the booms and ends with a shock load) are given. Results show that the typical attitude control system of a nanosatellite is not enough to sustain the shock load that can be experienced by the central structure at the end of an uncontrolled deployment. A slow and motorized deployment of such a structure is preferred, since the torques that it transmits to the whole system can be damped easily with very small reaction wheels. The last section of chapter 3 presents the results of numerical simulations on a boom simulated with a multibody

system, fixed on one side and free on the other. This study confirmed the feasibility of damping boom oscillations applying an ideal force to counteract them near the boom fixed side (where a possible actuator can be actually placed) with a Proportional Derivative (PD) control loop. Damping the oscillations of the appendage would reduce the transmission of vibration to the central body of the spacecraft. Chapter 4 presents the experimental tests to analyze the dynamic behavior of the system during uncontrolled deployments as well as controlled extensions and retractions of the appendage. The effectiveness of passive dampers positioned at the interface with a dummy external structure to reduce the vibration transmission was investigated. The dynamic behavior of the system was recorded using two MEMS sensors that included a 3-axis accelerometer and gyroscope. The data was collected and processed by the microprocessor Arduino Uno. A Gravity Offloading System (GOLS) based on the Marionette Paradigm theorized by G. Greshick and W.K. Belvin was realized with fly beams and long cables to suspend the system in order to simulate the absence of gravity during the tests. During uncontrolled deployments, shock loads were noticed to occur only when the structure was released short time after being rolled up. In the other cases, on the contrary, the stored strain energy was not enough to extend the structure, leading to incomplete deployments. This happened because the tests were done many months after manufacturing the booms and viscoelastic relaxations became very influent. Other tests were done with a motorized deployment, using a small stepper motor to provide a slower and more controllable vibrations environment. The small amplitude vibrations generated by the motor during controlled deployment were reduced very efficiently with the passive dampers. The last section of Chapter 4 reports the results of a test where a Proportional Integral Derivative (PID) control scheme was used to damp more quickly the oscillations of a tape spring around its equilibrium position. In this experiment, the same sensor used in the previous tests was placed at the tip of the boom, while the motor was used as actuator. The tests highlighted the feasibility of reducing the oscillations simply deploying or retracting the boom by a small number of motor steps.

In conclusion, numerical simulations and experimental tests have been performed

to study two test cases: the *first test case* was analyzed from a numerical point of view, while the *second test case* was both numerically simulated and experimentally tested. Dynamic analyses of the behavior of flexible structures were carried out, and the feasibility of different control systems to damp vibrations or reduce their transmission to the central body of a small spacecraft was validated.

Sommario

Negli ultimi anni, le strutture estremamente flessibili, tecnicamente chiamate *gossamer structures*, stanno acquisendo un notevole interesse nel campo spaziale. Considerate come uno dei tipi di strutture più promettenti per rendere possibili missioni spaziali innovative, queste strutture vengono sempre più spesso utilizzate in diverse applicazioni, come ad esempio i pannelli solari a film sottile, antenne dispiegabili, concentratori solari, vele solari, ecc. Generalmente, queste strutture sono composte da un sottile strato di materiale tenuto in tensione da una struttura di supporto, tipicamente composta da sistemi dispiegabili o gonfiabili, telescopici o meccanismi articolati. Tali strutture sono dunque molto attraenti, in quanto occupano un volume ridotto, cosa spesso non possibile con altri tipi di strutture convenzionali. Inoltre, la loro massa è inferiore, quindi il loro costo di lancio risulta ridotto. Questi vantaggi li rendono una tecnologia estremamente interessante per i satelliti di piccole dimensioni, come ad esempio i nanosatelliti (inclusi i CubeSat).

Questi veicoli stanno diventando sempre più comuni grazie alla loro capacità di fornire molti dei servizi che in passato erano effettuati da satelliti più grandi. Mentre le dimensioni dell'avionica e degli strumenti sono diminuiti negli ultimi decenni con una generale tendenza alla miniaturizzazione, le dimensioni delle strutture dispiegabili come i pannelli solari o le antenne non possono essere similmente ridotti, poichè le loro dimensioni non variano con la grandezza del satellite ma sono dipendenti dalle specifiche di missione e di applicazione. Tuttavia, con la miniaturizzazione delle dimensioni dei satelliti, le performance del sistema di controllo di assetto sono soggette a una consistente limitazione, generalmente per restrizioni in termini di potenza e di volume disponibili. Pertanto, grandi appendici montate su un satellite di piccole dimensioni possono essere un problema in termini di controllo di assetto. Per questo

motivo occorre limitare o evitare le oscillazioni di queste strutture per poter ridurre la trasmissione di coppie di disturbo dall'appendice dispiegabile al corpo centrale del satellite.

Due diversi casi sono stati identificati per questo studio, entrambi focalizzati su pannelli solari. Il primo caso è basato su un pannello solare a membrana che può fornire fino a 0.5-1 kW di potenza, mentre il secondo considera un pannello solare arrotolabile e dispiegabile di 0.3 x 1 m^2 di area.

Questa tesi è organizzata nel modo seguente: dopo un'introduzione alle strutture altamente flessibili nel Capitolo 1, viene presentato il primo caso nel Capitolo 2, mentre il secondo caso è discusso nei Capitoli 3 e 4. Le conclusioni sono riportate nel Capitolo 5.

In particolare, il Capitolo 1 presenta lo stato dell'arte delle strutture spaziali flessibili, focalizzandosi su i pannelli solari a film sottile, le vele solari e le antenne. In seguito, sono presentati in dettaglio le motivazioni e gli obiettivi della tesi e i due casi sono descritti in dettaglio. Infine è riportato il flusso di lavoro della tesi, con l'obiettivo di guidare il lettore ad una maggiore comprensione delle attività descritte.

Il capitolo 2 presenta il primo caso studiato, che si concentra su un pannello solare a membrana in grado di produrre fino a 0.5-1 kW di potenza. Lo scopo di questo capitolo è quello di esplorare una possibile strategia per controllare le oscillazioni su una membrana non supportata da una struttura esterna. In primo luogo, viene fornita una panoramica sui materiali piezoelettrici, introducendone le proprietà quando vengono utilizzati come sensori e/o attuatori. La sezione seguente presenta le simulazioni numeriche che dimostrano la fattibilità di ridurre le oscillazioni provocate da un disturbo esterno sinusoidale e da condizioni iniziali non "piatte" tramite l'utilizzo di sottili patch di materiale piezoelettrico distribuiti sulla superficie del pannello. I risultati delle simulazioni hanno confermato la possibilità di applicare il robusto sistema di controllo H_∞ a loop chiuso, al fine di correggere la forma iniziale non orizzontale della membrana per raggiungere una configurazione piatta. Questo primo caso si basa su studi precedentemente condotti dall'autrice nel contesto della tesi magistrale, dove è stato studiato il comportamento dinamico di una membrana di grandi dimensioni sottoposta ai disturbi tipici in orbita terrestre bassa.

I capitoli 3 e 4 presentano il secondo caso studiato, focalizzato su un pannello solare di 0.3 m^2 di area, dispiegato e mantenuto in tensione da due *tape spring*. Le *tape spring* sono un elemento strutturale, il cui principio di funzionamento è paragonabile a un metro a nastro e che presentano due configurazioni stabili di energia minima, nella condizione di arrotolamento e dispiegata. La trasformazione tra queste due configurazioni avviene in una breve zona di transizione che si muove lungo la struttura durante il dispiegamento e può essere attivata aggiungendo una quantità notevole di energia al sistema, ad esempio tramite un carico meccanico. Questi elementi dispiegabili sono tipicamente realizzati con laminati compositi ultra-sottili, materiali a basso peso che permettono l'immagazzinamento in un volume molto piccolo e forniscono buona rigidità nella configurazione dispiegata. In primo luogo, viene presentato lo stato dell'arte di queste strutture. Viene poi fornita una descrizione matematica del sistema, con il calcolo di proprietà specifiche per il materiale utilizzato per i prototipi effettivi utilizzati nelle prove sperimentali, con il calcolo di quantità fisiche come forze e coppie sperimentate da queste strutture durante il loro dispiegamento; questa prima parte del lavoro si basa in particolare sulla teoria sviluppata da S. Pellegrino e dal suo gruppo di ricerca. Essendo queste strutture molto complesse da modellare matematicamente e sottoposte a molte variabili difficili da controllare e prevedere, quali il rilassamento viscoelastico del materiale dopo lunghi tempi di stivaggio, l'attrito e l'effetto di microcricche, sono state condotte tre prove preliminari per studiare le proprietà reali dei prototipi in termini di (1) caratteristiche elastiche e di smorzamento, (2) coppie che devono essere esercitate da un motore per controllarne il dispiegamento e (3) coppie trasmesse ad una struttura esterna alla fine del dispiegamento, quando si verifica un carico impulsivo. I risultati di questi test preliminari sono stati quindi utilizzati in successive simulazioni numeriche e prove sperimentali. In particolare, in questo documento vengono presentate simulazioni del comportamento dinamico di un nanosatellite in orbita bassa terrestre sottoposto a disturbi ambientali tipici durante il dispiegamento dei pannelli solari, introducendo la dinamica sia di dispiegamenti controllati (lenti e motorizzati) che di dispiegamenti incontrollati (veloci, che sfruttano l'energia di deformazione delle *tape spring* e si concludono con un carico impulsivo). I risultati mostrano che il sistema

di controllo d'assetto tipico di un nanosatellite non è sufficiente a sostenere il carico d'urto che può essere sperimentato dalla struttura centrale alla fine di un dispiegamento incontrollato. Al contrario, un dispiegamento lento e motorizzato di una tale struttura fa sì che le coppie che vengono trasmesse all'intero sistema posano essere facilmente smorzate con ruote di reazione molto piccole. L'ultima sezione del Capitolo 3 presenta i risultati delle simulazioni numeriche su una *tape spring* simulata con un sistema multibody, fissata da un lato e libera di oscillare dall'altro. Questo studio ha confermato la fattibilità di smorzamento di possibili oscillazioni della *tape spring* applicando una forza vicino al lato fisso (dove un eventuale attuatore può essere posizionato) con un loop di controllo Proporzionale Derivativo. Lo smorzamento delle oscillazioni dell'appendice ridurrebbe la trasmissione della vibrazione al corpo centrale del satellite.

Nel Capitolo 4 vengono presentati i test sperimentali, dove viene analizzato il comportamento dinamico del sistema durante i dispiegamenti non controllati, nonché le estensioni e le retrazioni controllate dell'appendice. Inoltre è stata valutata l'efficacia degli ammortizzatori passivi posizionati all'interfaccia con una struttura esterna per ridurre la trasmissione di vibrazioni. Il comportamento dinamico del sistema è stato studiato utilizzando due sensori MEMS che includono un accelerometro e un giroscopio a tre assi. I dati sono stati raccolti e processati dal microprocessore Arduino Uno. Un sistema di sospensione basato sul "Marionette Paradigm" teorizzato da G. Greshick e W.K. Belvin è stato realizzato tramite aste e lunghi cavi per sospendere il sistema al fine di ridurre l'effetto della gravità durante i test. Durante i dispiegamenti incontrollati, i carichi di shock sono stati notati solo quando la struttura è stata rilasciata pochi istanti dopo essere stata arrotolata. Negli altri casi, al contrario, l'energia immagazzinata non era sufficiente ad estendere la struttura, portando a dispiegamenti incompleti. Ciò si può spiegare con il fatto che i test sono stati eseguiti molti mesi dopo la produzione dei prototipi e i rilassamenti viscoelastici sono diventati molto influenti. Altri test sono stati effettuati con un dispiegamento motorizzato, utilizzando un piccolo motore passo-passo, che forniva un ambiente di vibrazioni più lento e più controllabile. Le vibrazioni di piccola ampiezza generate dal motore durante il dispiegamento controllato sono state smorzate in modo

molto efficiente tramite gli ammortizzatori passivi. L'ultima sezione del Capitolo 4 riporta i risultati di un test in cui è stato utilizzato uno schema di controllo Proporzionale Integrativo Derivativo per smorzare più rapidamente le oscillazioni di una *tape spring* intorno alla posizione di equilibrio. In questo esperimento, lo stesso sensore utilizzato nei test precedenti è stato posto all'estremità della *tape spring*, mentre il motore è stato utilizzato come attuatore di controllo. I test hanno messo in evidenza la fattibilità di ridurre le oscillazioni facendo semplicemente estrarre o ritrarre la *tape spring* controllando il numero di passi del motore.

In conclusione, sono state eseguite simulazioni numeriche e prove sperimentali per studiare due casi: il caso # 1 è stato analizzato da un punto di vista numerico, mentre il caso # 2 è stato simulato numericamente e testato sperimentalmente. Sono state eseguite analisi dinamiche del comportamento delle strutture flessibili ed è stata validata la fattibilità di due diversi sistemi per controllare le vibrazioni o ridurne la loro trasmissione al corpo centrale di un piccolo satellite.

Acknowledgements

This PhD experience has been very tough, but at the same time extremely meaningful both from a professional and a personal point of view. These three years have brought huge challenges and so many times I thought I would not have been able to make it to the end. However, with the encouragement and support of so many, I have been able to see the light at the end of the tunnel.

First of all, I would like to express my special gratitude and appreciation to my supervisor, Prof. Alessandro Francesconi, who has given me the opportunity to conduct my research as part of this amazing team.

The aspect of the PhD life I have treasured the most has been spending time with my amazing colleagues, who always listened to my doubts and tried to answer my questions, supported me in the lab and gave me suggestions on how to move forward when I got stuck with my work. I would definitely not be here now without their support and patience.

In particular, I want to thank Lorenzo, who has been a fantastic colleague and friend: with him I was able to talk about everything, discuss crazy ideas, laugh and cry. He has always been available to help me on professional matters and taught me many things. During these past few years we spent a lot of time together, from organizing a symposium, to eating a lot of ice-cream. Lorenzo, you have my deepest gratitude.

Another special thank you goes to Giulia: I will never forget the times she spent helping me, even on Sundays and in the evenings, and all the great times we spent together running and chatting about everything. I am lucky to have you as a friend, Giulia!

I have also been blessed to spend these three years with Matteo (or Teo, as I

always call him), who has walked alongside me during this PhD. He has been an amazing friend and I could not have had a better office colleague. We shared happy and difficult moments, and even visited Mexico together after a conference. We were not only able to support each other by discussing our problems, but also happily hanging out and talking about things other than just work. Thank you for being my right hand, Teo!

I also wish to thank my friends and colleagues Francesco B., Francesco S., Francesco F., Mattia and Andrea A. who have dedicated a considerable amount of time helping and supporting me with technical matters during these years. A special mention of appreciation goes to Andrea C. who worked with me during his free time on the first test case presented in the thesis.

A special mention goes also to my friends, in particular to Annagiulia, Lorenza, Martina, Anna, Francesca, Giulia P., Vittoria and Katia: although we have been mostly far away from each other during these years, you have been a precious (remote) support, making my days brighter and happier.

And last but by no means least, a special thank you goes to my family and in particular to my brother Nicola and my father, who patiently supported me when I needed help, especially towards the end of the third year. And Reinhard, my love, you are the bright star that has made this little odyssey of mine possible.

Thank you all for always believing in me.

Contents

List of Figures

List of Tables

Acronyms

a-Si amorphous Silicon

CdTe Cadmium Telluride

CFRP Carbon Fiber Reinforced Plastic

CIGS Copper Indium Gallium Selenide

CLT Classical Lamination Theory

DLR German Aerospace Center

DSS Deployable Space Systems

EPDM Ethylene-Propylene Diene Monomer

ESA European Space Agency

FFT Fast Fourier Transform

GEO Geostationary Earth Orbit

GOLS Gravity Offloading System

HST Hubble Space Telescope

IAE Inflatable Antenna Experiment

ISS International Space Station

ITSAT Inflatable Torus Solar Array Technology

JPL Jet Propulsion Laboratory

LEO Low Earth Orbit

NASA National Aeronautics and Space Administration

OSS Oxford Space Systems

PD Proportional Derivative

PID Proportional Integral Derivative

PVDF Polyvinylidene fluoride

ROSA Roll-Out Solar Array

SAR Syntethic Aperture Radar

SSC Surrey Space Center

TRAC Triangular Rollable and Collapsible

Chapter 1

Introduction

The recent trend towards the miniaturization of spacecraft components and instruments highlights the need of simple, low mass and compactly stowed structures. Nanosatellites can now provide many of the services that were performed by large satellites in the past. Consequently, mission applications that were achievable in the past only with large satellites can be performed with small ones at a fraction of their costs. While the avionics and instruments have decreased in size, deployable structures must necessarily remain large. These structures are, for example, solar arrays, solar and drag sails, antennas... In order to be functional, these structures need to be miniaturized in terms of mass and stowed volume, including all their stowage and deployment systems. One important observation is that the dimensions of deployable structures are not scaling with the dimensions of their hosting satellite, but their required size depends on the specific mission and application [1].

Gossamer structures are expected to meet these requirements. They are defined as structures with extremely low mass and high deployed-to-packed volume ratios. These structures are typically composed of membranes, usually made of thin and low modulus materials such as polymer films. These structures are considered breakthrough space structures that will enable future innovative space missions. Their ultra-low areal density makes them attractive for achieving a high packaging efficiency, which is unattainable by other conventional structures. This allows the launch of a bigger payload in the same total volume. In addition, their lower mass with respect to traditional bulky structures makes their launch less expensive. Considering an average launch cost per kilogram to LEO between $2,720 (current cost

per kg of a Falcon 9 launch [2]) and $10,300 (current cost per kg of an Ariane 5 launch [3]), a reduced mass system allows more affordable missions.

Beside all the advantages mentioned above, their principal drawbacks are their very little inherent bending stiffness and their incapacity of carrying compressive loads. This is the reason why they are commonly found associated with tensioning structures such as deployable booms (tape springs, telescopic masts, etc.) or inflatable structures. In addition, the low vibration frequencies and small damping ratio make the vibration control of these structures extremely challenging.

It is important to point out that the name 'flexible' can be a misnomer. It is the membrane components that are flexible, not the supporting structure, that can be very rigid.

1.1 Overview of Membrane Structures in Aerospace

In the past decades, many examples of gossamer structures have been designed and tested. Typical gossamer structures for space applications are commonly found as solar arrays and concentrators, solar sails, deep space antennas and radars, telescopes, sun shields, etc... There has been an interest in (inflatable) deployable space structures since the 1950s, with the launch of the Goodyear antennas in the early 1960s [4].

1.1.1 Thin-Film Solar Arrays

Space solar arrays generate the required power to run all electric subsystems of the satellite with the conversion of solar light into electricity. The amount of power generated, measured in W (or kW), depends largely on the efficiency of the cells and the area of the solar array. The tendency towards the miniaturization of the satellites and the need of high amount of power to run the satellite systems lead to opposite directions. Considering that a typical power subsystem requires very often a large percentage of the total mass of the spacecraft, the research to advance the technology related to lighter solar panels is essential to decrease the impact on the total mass and volume of these structures, thus their cost.

Thin-film solar panels are a promising technology that has been investigated

since the 1960s, with the launch of the first communication satellites. However, these early attempts were abandoned due to their excessive degradation over time and low efficiency of the cells. For the next three decades, satellites employed mostly silicon solar panels thanks to their higher efficiency and stability. Since the nineties, researchers have made important advances in the thin-film technology and they are still an intense area of investigation today, because of their higher specific power and lower projected costs compared to the conventional solar arrays [5].

This-film solar cells are typically made of Copper Indium Gallium Selenide (CIGS), Cadmium Telluride (CdTe) or amorphous Silicon (a-Si) as active materials to collect the sunlight. In particular, CIGS absorption coefficient is higher than other semiconductor materials, therefore they require a much thinner film of material to absorb the same amount of sunlight, on the order of 1-2 μm. By comparison, a typical crystalline silicon wafer requires a thickness of about 160-190 μm, while a silicon thin cell requires up to 30 μm [6]. Thus, the layers result thin enough to allow their deposition on flexible substrates. Normally, the best performances are achieved when active layers are deposited at high temperature. This would require a substrate able to withstand high temperature, such as glass. However, in the past years, advances in the deposition of CIGS cells at low temperature have reduced the gap of this performance difference. These cells can be deposited, for example, on Kapton films, a polymeric material able to remain stable up to 400°C developed by DuPont®. CIGS photovoltaic cells have reached an efficiency of 20.4% at cell level deposited on a polymeric substrate [7] and 15.7% on larger modules (under AM1.5 light spectrum) [8].

This technology offers a number of advantages with respect to bulk solar panels:

- lightness;
- reduced volume;
- reduced launch cost;
- lower manufacturing cost (reduced amount of material needed and exploitation of the technology studied for terrestrial solar panels).

These advantages come together with some drawbacks that are being studied in order to make this technology sufficiently appealing and effective. These disadvantages are:

- Lower efficiency with respect to traditional solar panels;
- Their extreme flexibility, hence very low fundamental frequency, when deposited on a very thin substrate, on the order of tens of microns in thickness.

This last drawback can be overcome using different types of booms and/or specifically designed control systems, in order to withstand the typical orbital disturbances and satellite maneuvers that occur after the launch phase.

Brief history and state-of-the-art of thin-film solar arrays

Launched in 1990, the Hubble Space Telescope (HST) was the first satellite that used the rolled-out solar array technology. Its ESA-made solar arrays needed to be flexible to fit in an extremely small volume between the round-shaped telescope and the Shuttle cargo bay. Its solar arrays were 210 μm thick, 12.1-m long and 2.5-m wide in full extension. Another requirement was that they had to be retractable, in order to be rolled back up and to be brought back to Earth during the following servicing missions for further studies. Therefore, the HST initially used roll-out arrays made of a 14%-efficiency solar cells, deposited on a flexible polyimide blanket (Kapton) encapsulated in silicone coating and deployed by a tubular, extendable boom (Bi-STEM) deployment system, made from two circularized steel sheets in a C-shape to form a cylindrical boom. The operations altitude, around 600 km, imposed around 30,000 thermal cycles from -100°C to 100°C during a 5-year expected lifetime, i.e. 16 times per day, which was extremely challenging in the early 1990s. Several problems connected to this technology had to be overcome in the following servicing missions: the bi-stem booms used to deploy and tension the arrays were flexing at each passage through the day-night terminator due to the temperature differential between the two C-shaped components, causing a disturbance torque that exceeded the allowable limits. In addition to this, another failure in the compensation mechanism made it necessary to replace the whole array during the first Hubble Servicing Mission in December 1993 with 0.7-mm thick blankets. In December 1999,

(a)

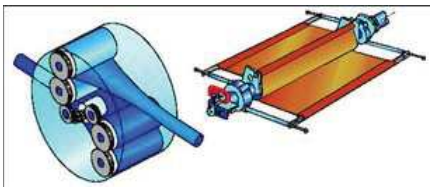

(b)

Figure 1.1: (a) HST first solar arrays and (b) detailed view of the deployer of HST first solar array. Photos: ESA

during an emergency Servicing Mission (3A), astronauts noticed another failure in the hinge pins that connected different segments of the solar blanket. The solar arrays were then replaced in 2002 during Servicing Mission 3B with the US-made third set of more efficient and rigid solar arrays. [9]

From the 1990s, after the HST experience, many options have been explored and important advances have been made in the solar array technology.

In addition to rigid booms, in the last three decades inflatable systems have been widely studied in order to provide deployment to space structures. This technology has the advantage of reduced stowage volume, mass and costs over current mechanically deployed solar arrays, as well as higher specific power (greater than 100 W/kg) [10]. However, some complete inflatable systems are not simple because they must include a gas container(s), the plumbing, a launch restrainer, a controlled deployment device, etc. that increase the total weight, stowage volume and complexity [11,12]. In addition, inflatables are vulnerable to micrometeorites and debris strikes that may damage their structures [13].

The two pioneering companies in the field of large inflatable structures were ILC Dover and L'Garde, that designed, in the nineties, solar arrays supported by an inflatable structure.

ILC Dover designed and built a full-scale prototype of inflatable structure to support a 3 x 10 m^2 solar array, that was originally planned to be mounted on the 288-satellite constellation of the Teledesic program. The full-scale prototype is shown in Figure 1.2. The structure was composed by 3 inflatable masts, mounted on

Figure 1.2: Teledesic Solar array. Image extracted from [14]

the backside of the solar array: the central one was designed with the only function to deploy the array, while the two external composite rigidizable inflatable tubes were designed to provide structural support to the entire array [10]. However, the Teledesic program was canceled and this structure never flew into space.

Another example of inflatable solar array was designed by L'Garde at the end of the 1990s. The **Inflatable Torus Solar Array Technology (ITSAT)** [15] was designed to supply power to small spacecraft, in the 0.2-1.0-kW class for a mission of 3 years in LEO to Geostationary Earth Orbit (GEO). The solar panel, shown in Figure 1.3 was 0.74-m wide and 3.25-m long, with two external inflatable cylinders

Figure 1.3: ITSAT Solar array. Image extracted from [15].

made of an aluminum sheet sandwiched between two layers of Kapton foils. This prototype was fully tested in vacuum chambers with different types of solar cells.

The most recent tests aboard the International Space Station (ISS) have been performed in June 2017 on the state-of-the-art flexible solar array developed by another US-based company, *Deployable Space Systems (DSS)*, sponsored by NASA's Space Technology Mission Directorate as part of its Solar Electric Propulsion project [16–18]. The **Roll-Out Solar Array (ROSA)** was extracted from the SpaceX Dragon supply ship using the Canadarm2 and deployed successfully into space (see Figure 1.4) with a two-stage process that took about 10 minutes. The orbital testing were envisioned to characterize the deployment loads and kinematics, the structural dynamics, the behavior of the structure during the passage from eclipse to illumination, the survivability and performance of the blanket and the retraction loads and kinematics. However, after one week of tests, ROSA was jettisoned after it failed to retract into its stowed configuration at the end of its planned testing operations. DSS patented this elastically deployable solar array in 2014. ROSA started its initial development tests several years ago in terrestrial vacuum chambers. It is sized to provide nominally 20 kW of electric power per array, with a total size of 6 m x 13.7 m. The patent includes different types of longitudinal structure: it can be made of tubular thin-walled open section roll-out booms, metallic or composite reinforced slit tube (open section) or closed section hollow members, that self-deploy under their own strain energy, without the use of motorized systems [19, 20]. The flexible solar panel is uncoupled from the longitudinal members. In this way, it can be stowed

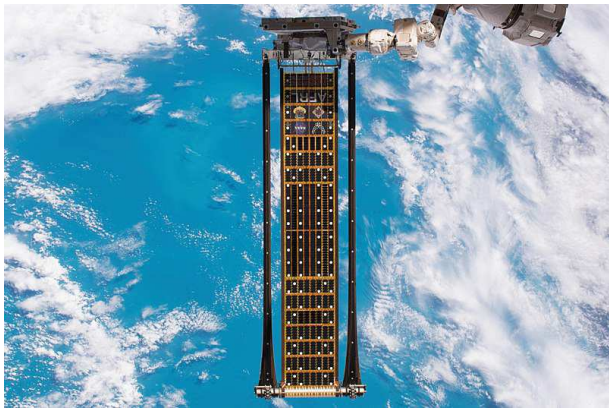

Figure 1.4: ROSA after deployment from ISS/CANADARM. Image credits: NASA.

either in a rolled form or Z-fold (accordion flat shape).

1.1.2 Solar Sails and Drag Sails

Solar and drag sails are another type of gossamer structures that are very similar in terms of shape but have two very different working principle and different requirements.

Solar sails are propellantless propulsion systems that exploit the solar radiation pressure to move in space. Solar protons generate thrust when they are reflected on the surface of the sail. Therefore, these structures require very large reflective surfaces to maximize the force induced by the solar pressure. For this reason, they are typically made of very thin membranes, coated with a metallic layer. On the other hand, they need to be extremely light to maximize the acceleration imparted to the satellite.

Drag sails are passive deorbiting devices that typically employ a similar design with huge deployable surfaces. They exploit the drag force caused by the thin residual atmosphere in LEO to decelerate the satellite at the end of its primary mission, lowering its orbit until re-entry and burn-up. These structures need to withstand long stowage times, requiring a specific material selection and reliable mechanism design.

Brief history and state-of-the-art of solar/drag sail technologies

JAXA's Small Solar Power Sail Demonstrator **IKAROS** [21] is the first spacecraft to successfully demonstrate solar sail technology in interplanetary space. After its launch in 2010, IKAROS deployed its 14x14 m^2 sail via spinning motion with 0.5 kg tip masses positioned the corners of the sail. It is made of a 7.5 μm thick sheet of polyimide with a mass of about 10 g/m^2 and is provided with a thin film solar array embedded in the sail. Along its edges, 80 liquid crystal devices (LCD) are used for demonstrating a new attitude control concept, with the adjustment of their reflectance properties by turning on and off the power of the device and without the use of additional propellant. An artist depiction is shown in Figure 1.5a and its schematic design in Figure 1.5b.

The German Aerospace Center (DLR) developed the booms for the CubeSat

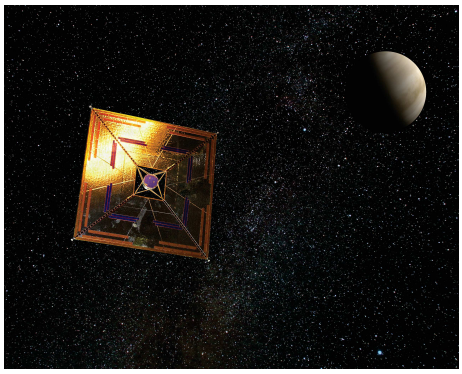

(a)

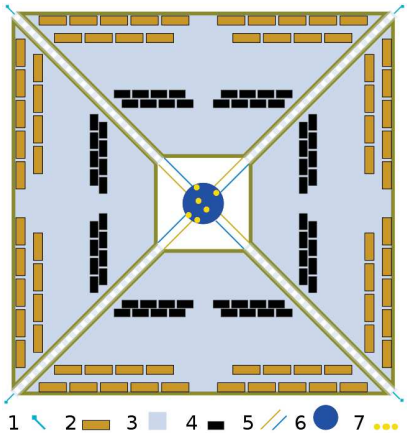

(b)

Figure 1.5: (a) Artist's depiction of JAXA's IKAROS satellite [22] and (b) schematic design.

DeorbitSail launched in the summer of 2015. In this project, led by Surrey Space Center, U.K., DLR designed, built and qualified new CFRP booms and its deployment system. For this application the booms and mechanism were designed, as

(a)

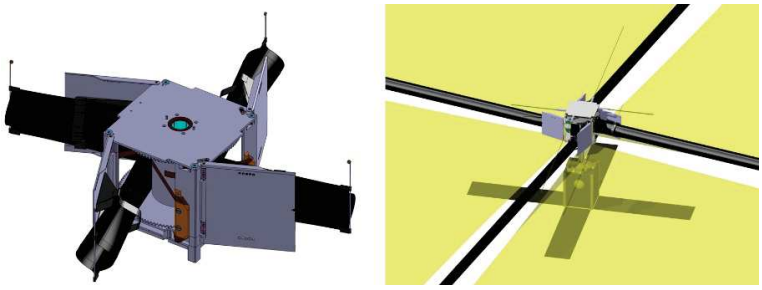

(b)

Figure 1.6: (a) DLR composite booms of different sizes and (b) Deorbitsail deployment mechanism. Source: DLR.

depicted in Figure 1.6, to demonstrate rapid deorbiting using a 4 m x 4 m square drag sail suitable for small size satellites. The sail is deployed by four booms positioned at 90° from each other. Each supporting boom consists of two Ω-shaped elements bonded on their edges, made of carbon fiber 0.1-mm thick and with 62 g/m linear density. This type of booms is shown in Figure 1.6a and its deployment mechanism in Figure 1.6b. It was demonstrated that the boom deployment needs to be controlled as excessive strain energy leads to a chaotic deployment [23]. They have used two different controlled deployment schemes. The first method uses an inflatable polymer hose inside the boom and the second one employs an electromechanical uncoiling device. Despite many attempts, the team has not been able to deploy the sail.

Gossamer Deorbiter is an European Space Agency (ESA) funded project that consisted on the development of three drag sails of increasing size. The 5x5 m^2 sail developed by Surrey Space Center (SSC) was kept in tension by 4 bistable carbon fiber booms, C-shaped to increase the bending stiffness and two minimum energy states (rolled and deployed). The manufactured Carbon Fiber Reinforced Plastic (CFRP) booms have a nominal thickness of 0.245 mm, while the cross-section has

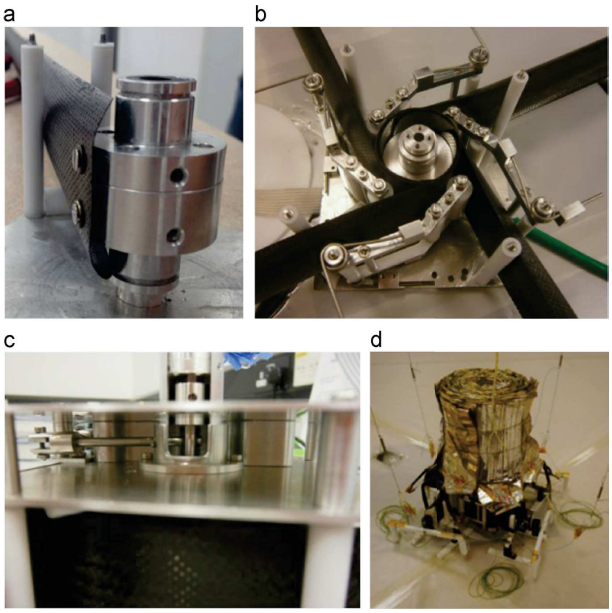

Figure 1.7: Deployment mechanism of the Gossamer Deorbiter. Image extracted from [24].

a radius of curvature of 16 mm and subtends an angle of approximately 160°. The stored height of the booms is therefore 45 mm, and the four co-coiled booms have an outer diameter of 85 mm. The mass per unit length of this boom concept is 15 g/m, with each of the four 3.6 m booms therefore weighing 65 grams. The deployment mechanism is shown in Figure 1.7.

Both NASA's **Nanosail D-2** satellite, launched in 2010, and the Planetary Society's **Lightsail-1**, launched in 2015, deployed a square solar sail, with AFRL-developed Triangular Rollable and Collapsible (TRAC) booms technology, shown in Figure 1.8. These booms have the highest bending rigidity per spool height of any rollable mast. They are made of ELGILOY (stainless steel, 8.30 g/cm^3) metal strips, C-shaped.

Figure 1.8: TRAC boom. Image credit: NASA

1.1.3 Antennas

Space antennas can be used for different tasks: communication antennas are used to exchange signals with ground stations or with other satellites, while radar antennas used for surveillance and reconnaissance tasks as well as scientific exploration missions, scanning the ground below or adjacent to the ground path. Communication with high data rates and low power consumption requires large reflectors. Usually, antennas for high volume data transfer are realized with parabolic reflectors, or, in some cases, with flat array antennas. In both cases, the size of the antenna and the required surface accuracy are related to the frequency band: higher

frequencies signals (therefore, shorter wavelengths) require a smaller antenna, but higher surface accuracy. Radar antennas use also the interferometric effect to enhance the quality of the acquired image: this is the so called Syntethic Aperture Radar (SAR) [25].

Brief history and state-of-the-art of space antennas

Different concepts of membrane antennas and reflectors have been studied in the past decades. The Inflatable Antenna Experiment (IAE) [26] was the first example of deployment in space of a low-cost parabolic reflector antenna through its three 28 m inflatable struts. Typically, inflatable structures are manufactured with in-situ rigidizable materials. This means that the booms are packaged in a flexible configuration, they are deployed with inflation gas and then made rigid with external factors such as heat or UV light. This 14-m lenticular structure was developed by National Aeronautics and Space Administration (NASA) and based on the L'Garde concept. It flew aboard the Space Shuttle Endeavour in 1996 and was conceived to study and verify the accuracy of the system. It is shown in Figure 1.9 after it achieved full deployment, in an unexpectedly uncontrolled and chaotic way.

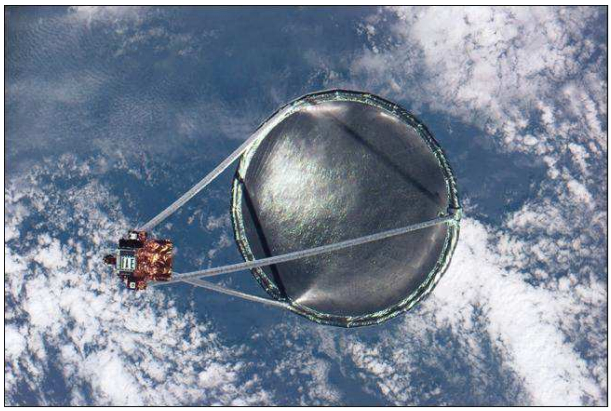

Figure 1.9: Inflatable Antenna Experiment. Image credit: NASA

Another example of membrane antenna is shown in Figure 1.10. This 3.3 x 10 m inflatable SAR [14] is an ultra-lightweight, low packing volume antenna developed by ILC Dover and Jet Propulsion Laboratory (JPL). It is supported by a frame of inflatable booms, initially rolled towards the center of the structure (see Figure 1.10a). The booms contain constant force springs inside the inflatable structure to

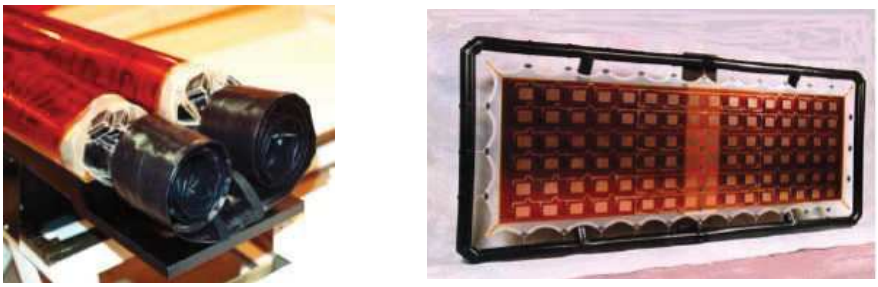

(a) (b)

Figure 1.10: Antenna stowed (a) and deployed (b), developed by ILC Dover and JPL. Images extracted from [14]

deploy it in a controlled manner and simultaneously on both sides.

1.2 Thesis Motivations and Objectives

In these last decades highly flexible structures, also called *gossamer structures*, are gaining significant interest in the space field. Considered as one of the most promising systems that will make innovative space missions possible, these structures are being more and more used in various applications, such as thin-film solar arrays, deployable antennas, solar concentrators, solar and drag sails, etc. These structures are typically made of a very thin layer of material kept in tension by a supporting structure that is generally made of deployable or inflatable booms, telescopic structures or articulated mechanisms. Their ultra-low areal density makes them attractive for achieving high packaging efficiency, which is unattainable by other conventional structures. In addition, their lower mass with respect to traditional bulky structures makes their launch less expensive. These advantages make them an extremely interesting technology for satellites of small classes, such as nanosatellites (including CubeSats) that are becoming more and more common because of their capability to provide many of the services that were performed by larger satellites in the past.

While the avionics and instruments have decreased in size in the past decades, with a tendency towards a general miniaturization of the spacecraft, deployable structures such as solar panels or antennas must remain large, with a size that does not vary with the dimension of the hosting satellite but depends on the specific mis-

sion and application. Nevertheless, with the miniaturization of satellite sizes there is a tendency to reduce the capabilities of the overall attitude control system, typically because of power or available volume limitations. Therefore, large appendages mounted on a nanosatellite can be an issue in terms of attitude control, with a possible reduction of the stability and pointing precision, or even the loss of the whole mission. For this reason, control systems must be envisaged in order both to limit or avoid the oscillations of these structures and to reduce the transmission of disturbing forces from the deployable appendage to the central body of the satellite.

Considering the previously mentioned concerns on the use of deployable structures on satellites of small sizes, the purposes of this Ph.D. research are twofold:

- the analysis of the dynamic behavior of highly flexible space structures (1-2) and the effects that these deployable structures have on the dynamics of the whole satellite (2), and
- the study of the effectiveness of possible methods to control their oscillations, both in terms of damping techniques directly applied to the appendage (1-2), and vibrations transmission reduction at the interface between the deployed structure and the main body of the satellite (2)

where (1) and (2) refer to the test case in which they are studied. The two selected test cases are presented in Section 1.3.

1.3 Identification of Test Cases

Two test cases with completely different approaches were identified for this study, both based on solar arrays.

The *first test case* focuses on a membrane solar array not supported by an external structure subject to a sinusoidal force and non-flat initial conditions. Its size is such that it can provide up to 0.5-1 kW of power. Numerical simulations explore the effectiveness of controlling the oscillations by means of thin patches of piezoelectric material used as sensors and actuators. Solar panels with different sizes and different numbers of piezoelectric patches are simulated. This first study explores the possibility to apply the robust closed-loop algorithm H∞ to correct the initial

non-horizontal shape of the membrane and to reject external disturbances to reach a flat deployed configuration.

The *second test case* studies the dynamics of a CubeSat-sized solar array structure that is deployed and kept in tension by two external composite tape springs. This type of booms has been selected because they can be stored extremely efficiently on a spool during launch and easily deploy when in orbit, meeting the size constraints of nanosatellites. Comparisons will be made considering a controlled and uncontrolled deployment. In the first case, a small motor controls the deployment of the two booms, while in the second case they deploy thanks to their stored strain energy. Numerical simulations and experimental tests investigate the dynamics of the system in these two situations. Moreover, possible control strategies in terms of active oscillations reduction directly applied to the appendage structure as well as passive vibration isolation between the deployed structure and the main body of the satellite are studied.

1.4 Thesis workflow

Figure 1.11 visually shows the thesis workflow, to guide the reader throughout the work.

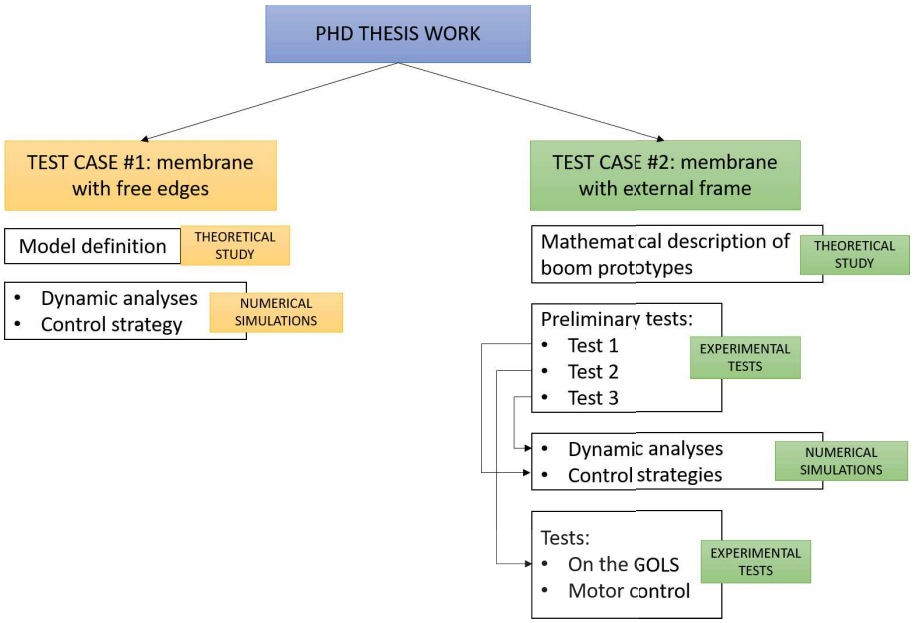

Figure 1.11: Thesis workflow.

Chapter 2

Numerical dynamic analyses on a membrane with free edges

This Chapter presents the *first test case* considered in this thesis. It focuses on a membrane solar array not supported by an external structure, subjected to a sinusoidal force and non-flat initial conditions. Such a membrane that extends from a satellite should avoid to transmit unwanted oscillations to the central body. This can be obtained with the rejection of the external disturbances, reaching and maintaining a flat, non-oscillating configuration.

Objective The purpose of this study is to explore the possibility to apply the robust closed-loop algorithm H∞ to modify an initial non-flat shape of the membrane and to reject external disturbances to reach a flat deployed configuration.

Method Numerical simulations based on the lumped-mass method explore the effectiveness of controlling the oscillations by means of thin patches of piezoelectric material used as sensors and actuators. Solar panels with different sizes and different numbers of piezoelectric patches are simulated.

2.1 Introduction

Smart materials are defined as materials that change their properties as a reaction to external stimuli. In particular, when a piezoelectric material is mechanically deformed, it polarizes redistributing its electric charge. Consequently, it generates

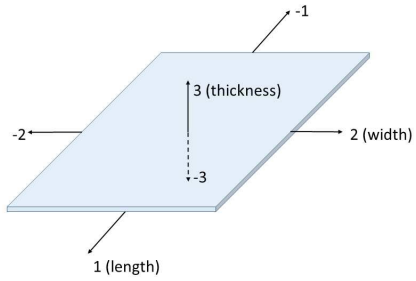

Figure 2.1: Symmetry axes nomenclature on a piezoelectric patch.

a voltage difference in output (direct effect). Vice versa, when piezoelectric materials are exposed to an electric field, they change their atomic configuration. This results in a change of physical shape (reverse effect). This dual behavior allows their utilization both as sensors and actuators. Generally, piezoelectric materials show a different polarization along the directions of the three symmetry axes [27]. The axes definition of a piezoelectric patch is shown in Figure 2.1.

In the past, research focused especially on vibrations damping of beams and plates made of aluminum, steel, composite, etc. as supporting material [28]. Notable work has been done on the vibration suppression on a flexible cantilever composite plate, where both the bending and torsional modes were controlled with piezoelectric patches. This study showed that bending vibrations can be efficiently suppressed with piezoelectric elements with their longitudinal axis aligned with the longitudinal axis of plate, while torsional vibrations are counteracted well by patches positioned at a 45° angle with respect to the previous [29–32]. Another interesting work was carried out on an aluminum beam comparing the PID and LQR control schemes using two different piezoelectric materials [33].

Some research on the use of smart materials on membrane structures has been done as well, not only using piezoelectric materials but also shape-memory alloys. The most common solutions use a tensioning system in the external frame of the membrane. Researches have been carried out using piezo-elements located in the suspension cables to modify their tension and reduce the vibrations of the overall structure [34–36]. Also the Canadian Space Agency studied the problem of keep-

ing a membrane flat for the design of a space Synthetic Aperture Radar. In this study, shape-memory alloys actuators were placed on the boundaries of the antenna, in order to apply tension forces to the membrane [37]. Another study proposes to control the vibrations of a pre-tensioned membrane with piezoelectric films evenly distributed on its surface. It employs an energy-recycling semi-active method (LR-switching method) [38]. A finite-element study was carried out to study the behavior of a square membrane bi-axially pre-stressed with bonded piezoelectric materials as both sensors and actuators. It showed that a single patch with different thickness can suppress the vibrations on a membrane more efficiently than applying many transducers [28]. Another study proposes to employ the Dynamic Vibration Absorber to suppress micro-vibrations on a tension-stabilized structure [39].

This study investigates a different configuration of smart control system. Patches of smart material that act as both sensors and actuators connect different portions of the membrane. When the membrane deforms, the patches deform as well, and a voltage is measured at the terminals of the sensors circuit. At the same time, the control system deforms the actuators to counteract this deformation. Numerical simulations are performed on a system based on the lumped mass method. Each element is composed of a mass and a joint, that takes into account the elasticity and damping properties of the material. A control system applied on the joints simulates the behavior of the smart material. In these simulations the behavior of the system is investigated in terms of deformation and requested control authority.

2.2 Piezoelectric materials theory

In this work, Polyvinylidene fluoride (PVDF) patches are considered as sensors and actuators. PVDF is a thermoplastic, ferroelectric polymeric material available in films that exhibits piezoelectric properties after opportune conditioning with a strong electric field. In this specific application, it has some advantages with respect to the traditionally used ceramic materials, such as lower density (1780 kg/m^3, more similar to the density of the membrane polymeric material). Moreover, with their lower stiffness PVDF patches are more sensitive with respect to piezo-ceramic elements when used as sensors, and they influence less the dynamics of the host

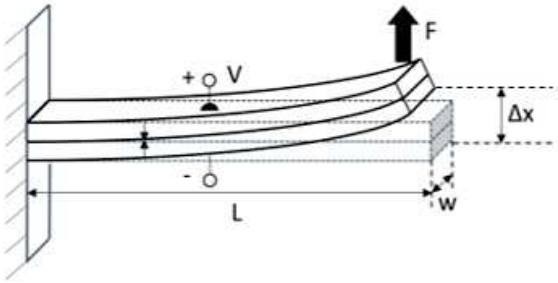

Figure 2.2: Bimorph configuration for piezoelectric actuators with the layers connected in parallel.

structure [37, 40].

When a voltage is applied to its electrodes, the PVDF patch bends. A configuration with two or more layers of piezoelectric material of opposite polarization bonded together is called bimorph. It is shown in Figure 2.2. If a voltage difference is applied to the electrodes, one element tends to lengthen, the other to shorten, resulting in an overall bending of the unit. Compared to a single-layer element, with a bimorph configuration it is possible to have larger deformations with a lower applied voltage [27]. On the other hand, when a piezoelectric sensor undergoes a compressive load, it generates a positive voltage. Vice versa, when it is stretched, it generates a negative voltage.

The generated force for such element is:

$$F = \frac{3}{2} E_k w d_{31} \frac{t}{l} V \tag{2.1}$$

where w is the width of the patch and E_k represents its Young's modulus, d_{31} is the piezoelectric coefficient in the '1' direction (see Figure 2.1), l and t are respectively the length and the thickness of the unit and V corresponds to the applied voltage. As it was previously mentioned, the advantage of this configuration is that it produces sizable deflections. On the other hand, the produced forces are low [27]. For example, forces achievable by an actuator with dimensions of 3x1.5 cm with 28 μm of thickness are on the order of $10^{-3} \div 10^{-4}$ N.

In addition to the previously mentioned properties, PVDF patches can operate in a very wide dynamic range, from 0.001 Hz to 10^9 Hz [27]. The performed simulations

refer to a system that undergoes low frequency disturbances, included in the range of operation of PVDF sensors.

2.3 Numerical simulations

This section reports the system configuration and the results of the simulations performed on the first test case, introduced in Section 1.3. The simulations show the behavior of a rectangular membrane representing a thin-film solar panel that extends from a satellite. This innovative type of solar panels is becoming more common in these last decades, because the efficiency of thin-film solar modules is increasing thanks to the continuous research in this field: this results in a higher power density, lower mass and reduced stowage volume with respect to traditional solar panels. These advantages will make them a possible alternative for use on satellites in the future, especially on satellites of small sizes, where the needed solar cells area is small and the available volume to store them is reduced.

The purpose of this work is the study of the feasibility to control the bending oscillations of such a panel using piezoelectric sensors and actuators, controlled with the robust algorithm H_∞ [41]. The advantage of using an optimal control instead of a simple PID (Proportional Derivative Integral) control system is that being the system MIMO (Multi-Input Multi-Output) it is easier to find the controller parameters. In fact, being the system components strongly coupled, a standard PID is hard to tune. Moreover, the control law given by this routine is guaranteed to be optimal.

In these simulations, only the bending motion of the panel in the direction perpendicular to its length was considered, as if all the disturbance forces were directed perpendicular to it. This is explained in Figure 2.3.

Numerical simulations were carried out with Matlab® changing the parameters of the panel such as its length, its thickness as well as the number of sensors/actuators.

Previous works demonstrated that bending vibrations can be suppressed by piezoelectric patches attached to the panel with its polarized direction parallel to the direction of its length [30–32].

In the simulations, the mass-spring-damper model with n masses and joints

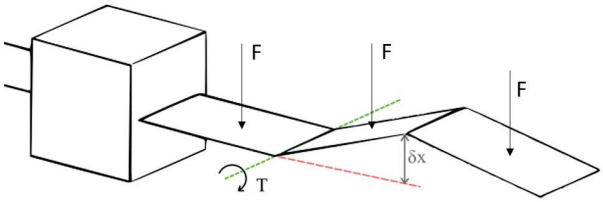

Figure 2.3: Sketch of the solar panel configuration. F is the disturbance force, T is the torque needed to counteract it.

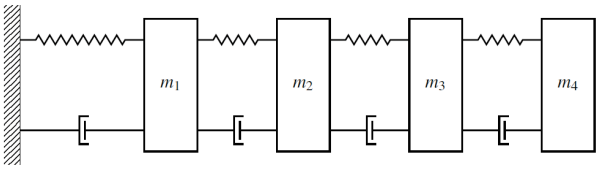

Figure 2.4: Mass-spring-damper system with 4 elements.

(spring and dampers) is considered. It is shown in Figure 2.4. It is possible to easily change all the parameters within the model. Each element of the panel includes a mass, a spring and a damper. The properties of the system correspond to the material properties and to its size (see Table 2.1 and 2.2).

A rectangular Kapton polyimide film was chosen among several materials that can be fabricated as thin foils to simulate the substrate of the solar cells. Kapton shows excellent mechanical, electrical and physical properties as well as good chemical resistance over a very broad temperature range, where other organic polymers do not show good performances or cannot even be used [28]. The latter property makes Kapton an ideal polymeric substrate for solar cells, that typically need high temperature for the deposition process [42]. Table 2.1 reports the standard properties of Kapton and the piezoelectric material PVDF. The dimensions of the considered system are shown in Table 2.2.

2.3.1 Control Algorithm

The following equations refer to a system with n degrees of freedom, with n masses and joints (spring and dampers). Equations 2.2 and 2.3 represent respectively the kinetic and potential energy:

Parameters	Kapton	PVDF	[ ]
Density	1420	1780	kg/m^2
Young's Modulus	2.5 E9	2 E9	N/m^2
Poisson's Ratio	0.34	0.20	-
Quality Factor	40	12	-

Table 2.1: Properties of the materials used in the simulations.

Parameters	Dimensions	[ ]
Length	3, 4, 5, 6	m
Width	0.4	m
membrane thickness	25, 50 E-6	m

Table 2.2: Dimensions of the simulated panels and piezoelectric patches.

$$K = \frac{1}{2}\sum_{i=0}^{n} J_i \ddot{\theta}_i^2 \tag{2.2}$$

$$U = \frac{1}{2}\sum_{i=0}^{n} k_i \theta_i^2 \tag{2.3}$$

where J_i are the moments of inertia of the section of the membrane, k_i are the elastic constants of the material and θ_i is the rotation of the element with respect to the horizon. The geometric, elastic and damping properties of each element were calculated in first approximation with the equations:

$$J_i = \frac{m_i}{12}(w^2 + t^2) \tag{2.4}$$

$$K_i = \frac{3E_k}{a_i^3}\frac{wt^3}{12} \tag{2.5}$$

$$c_i = 2\xi\sqrt{K_i m_i} \tag{2.6}$$

where the damping coefficient is:

$$\xi = \frac{1}{2Q} \tag{2.7}$$

m_i is the mass of each element, w is the width, t is the thickness, a_i is the length of each element, and Q is the mechanical quality factor of the material. The properties were validated in first approximation with the software Ansys®.

Euler-Lagrange equations lead to the following dynamic system:

$$\ddot{x} = Fx + G_1\tau + G_2\tau_D \tag{2.8}$$

where

$$x = \{\dot{\theta}_1 \dots \dot{\theta}_n \;\; \theta_1 \dots \theta_n\}^T \tag{2.9}$$

$$\tau = \{\tau_1 ... \tau_n\}^T \tag{2.10}$$

$$\tau_D = \{\tau_{D1} ... \tau_{Dn}\}^T \tag{2.11}$$

and

$$F = \begin{bmatrix} F_{11} & F_{12} \\ \mathbb{I}_n & 0_n \end{bmatrix} \tag{2.12}$$

where

$$F_{11} = \begin{bmatrix} -(c_1+c_2) & c_2 & 0 & 0 & \dots & 0 & 0 & 0 \\ c_2 & -(c_2+c_3) & c_3 & 0 & \dots & 0 & 0 & 0 \\ 0 & c_3 & -(c_3+c_4) & c_4 & \dots & 0 & 0 & 0 \\ \vdots & & & \ddots & & & & \vdots \\ 0 & 0 & 0 & 0 & \dots & c_{n-1} & -(c_{n-1}+c_n) & c_n \\ 0 & 0 & 0 & 0 & \dots & 0 & c_n & -c_n \end{bmatrix} \tag{2.13}$$

$$F_{12} = \begin{bmatrix} -(k_1+k_2) & k_2 & 0 & 0 & \dots & 0 & 0 & 0 \\ k_2 & -(k_2+k_3) & k_3 & 0 & \dots & 0 & 0 & 0 \\ 0 & k_3 & -(k_3+k_4) & k_4 & \dots & 0 & 0 & 0 \\ \vdots & & & \ddots & & & & \vdots \\ 0 & 0 & 0 & 0 & \dots & k_{n-1} & -(k_{n-1}+k_n) & k_n \\ 0 & 0 & 0 & 0 & \dots & 0 & k_n & -k_n \end{bmatrix} \tag{2.14}$$

and

$$G_1 = G_2 = \begin{bmatrix} \mathbb{I}_n \\ 0_n \end{bmatrix} \tag{2.15}$$

where x is the system state vector, τ is the control torque, which is non-zero only where the actuators are present. The parameter τ_D represents the external disturbances in terms of torques. The parameters c_i are the damping factors due to the material properties, and are calculated for each element of the panel.

It is assumed that the system state x (orientations θ and angular velocities $\dot{\theta}$) is known, with x_0 representing the initial parameters of the position of each portion of the panel. The sensors ideally bonded on the panel would provide information about the system state. Given the following cost function:

$$J(\tau, x_0) = \int_0^{+\infty} [x^T(t)Qx(t) + \tau^T(t)R\tau(t)]dt \tag{2.16}$$

where Q is a symmetric positive semi-definite matrix and R is a symmetric positive definite matrix, the objective is to find the optimal control law that minimizes:

$$u_{opt} = argmin_\tau J(\tau, x_0) \tag{2.17}$$

Considering the system in equation 2.17 and a matrix:

$$Q = diag(q_1 \dots q_n) = C^T C \tag{2.18}$$

where:

$$C = diag(\sqrt{q_1} \dots \sqrt{q_n}) \tag{2.19}$$

with $q_i > 0$, $\forall i$, then the system in Equation 2.17 is reachable and the matrix:

$$\begin{bmatrix} s\mathbb{I}_n - F \\ C \end{bmatrix} \tag{2.20}$$

is full rank for any parameter $s \in C$ with $Re[s] \geq 0$. System 2.8 is reachable because $G_1 = \mathbb{I}_n$, while the matrix 2.20 is always full rank being Q diagonal and full rank. Therefore, there exists a unique symmetric semi-definite positive solution M_∞ of the Algebraic Riccati Equation:

$$Q + F^T M + MF - MGR^{-1}G^T M = 0 \tag{2.21}$$

such that the control law:

$$\tau(t) = -R^{-1}G_1^T M_\infty x(t) \tag{2.22}$$

is stabilizable and minimizes the cost function 2.16 [41].

2.3.2 Simulations

This section reports the procedure followed in the simulations of a discretized version of the system 2.8, controlled with the control input 2.22.

The properties of the elements (mass, spring, damper) were calculated from the material characteristics of the membrane, listed in Table 2.1. Since the piezoelectric patches cover a small portion of the surface of the membrane, it was assumed that the overall properties of the Kapton membrane (Figure 2.5a) do not change significantly after the integration of the piezoelectric elements (Figure 2.5b). The validity of

Configuration	**K$_i$ [N/m]**	**Ref.**
Without patches	3.27 E-5	Figure 2.5a
With two rows of patches	3.29 E-5	Figure 2.5b

Table 2.3: Comparison between the stiffness coefficients obtained with Ansys® in a simple configuration without and with patches.

this assumption was confirmed by structural simulations performed with Ansys®. In the second model, the element with dimensions 3 cm (length) x 40 cm (width) considered a weighted average between the properties of the membrane and six 3 cm x 1.5 cm PVDF patches bonded in the direction of the width (see Figure 2.5c). These simulations confirmed the possibility of neglecting the increased stiffness introduced by the piezoelectric elements. The results of the simulations in the case without

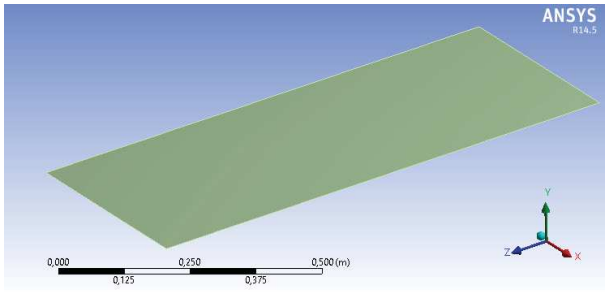

(a)

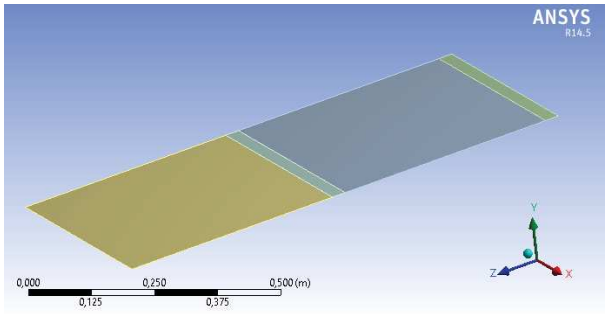

(b)

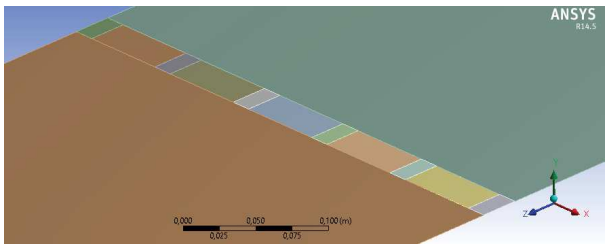

(c)

Figure 2.5: Simple rectangular geometry model with Kapton membrane dimensions 1x0.40 m (a) and geometry model with two rows of piezoelectric patches (b). The short right edge is fixed to the satellite. The smaller rectangles correspond to the PVDF patches (3x1.5 cm in size). In the simulations, the properties of the row along the width (X axis) were calculated as a weighted average of the properties of the patches and the membranes that separate them. (c)

patches and with 2 series of patches (that correspond to two springs and dampers) are shown in Table 2.3. The shortest membrane side showed on the right in the Figures 2.5a and 2.5b is fixed to the satellite. Finally, the control algorithm performance was evaluated with transient dynamical simulations realized with Matlab®. The sampling time was set to T=0.01 s, the control weight matrix was $R = 80 \cdot \mathbb{I}_n$ and the state weight matrix was $Q = 0.1 \cdot \mathbb{I}_n$, where the size n of the identity matrix $\mathbb{I}_n$ corresponds to the number of modeled masses.

In order to assess the performance of the control system, it is essential to establish some parameters that the system has to satisfy. In these simulations, it is necessary to consider the force that a piezoelectric patch can exert with a reasonable amount of voltage applied to its electrodes. This limit was fixed at 1.2 kV. This means that, considering 6 piezoelectric patches in parallel, their overall force that can be exerted is 6 times the force of a single actuator. Equation 2.1 was used to calculate the total force that could be achieved. Therefore, the maximum allowable force considered was 5.6 E-3 N. The initial conditions in terms of angles were set to 0.2 rad (about 11.5°) for all the elements of the panel. This means that the panel is bended.

2.3.3 Results summary

A certain amount of damping due to the material properties was observed in the simulations without control system. According to the results, under certain conditions, some configurations do not need a control architecture to damp the oscillations. This is particularly true for short panels, where the intrinsic elasticity and damping properties of the material damp the oscillations due to the external disturbances in a short time. Tables 2.4 to 2.7 report the time needed to achieve a 10% value of the initial condition of the oscillation with and without a control system for 25 μm and 50 μm thick panels. In the first case, 3 to 5 meters long panels were considered (see Tables 2.4 to 2.6), while 4 to 6 meters long panels were considered in the second case (Tables 2.5 to 2.7). The time needed to achieve a 10% value of the initial oscillation refers to the evolution of the amplitude of the peaks of oscillation of the center of mass of the last element of the panel, since the last element is the one that undergoes the highest oscillations. In particular, n is the number of

n	Time nc [s]	Time c [s]	%
	25 μm thickness		
4	760	375	50.66
6	703	477	32.15
8	675	542	19.70
10	652	566	13.19
12	647	582	10.05
14	640	594	7.19
16	635	598	5.83
18	630	601	4.60
20	629	603	**4.13**

Table 2.4: Oscillations of a 3-meter long panel (25 μm thickness). n is the number of elements, time nc and time c correspond to the time needed to reduce the initial oscillation to the 10% respectively in a "non controlled" and in a "controlled" system, and % is the percentage of reduction of the oscillations in the controlled system with respect to the non controlled one.

elements, *time nc* and *time c* are the times needed to reduce the initial oscillation to the 10% respectively in a "non controlled" and in a "controlled" system, and % is the percentage of oscillations damping in the controlled system with respect to the non controlled one. The numbers in bold in the tables highlight the percentage of reduction of the oscillation when the system is at regime. Small numbers show that the damping of the oscillations is mostly due to the intrinsic damping properties of the material, while higher values show that the control system is contributing to the reduction of the oscillations. In general, a control system is more useful and effective when applied to thinner (25 μm) and longer panels. This translates in a shorter time needed to reach a horizontal and flat configuration. Figures 2.6 and 2.7 show the data reported in the Tables 2.4 to 2.7 in a visual manner, with a comparison between the time for oscillation reduction to 10% with and without control system for panels of different length.

Figures 2.8 to 2.10 show an example of the output of the simulations. In particular, Figures 2.8 and 2.9 show the position state components referred to each element of a 5 m long panel, i.e. the angles with respect to the horizontal. The simulations start with the panels in a non-flat position. Figure 2.8 shows the evolution of the

n	Time nc [s]	Time c [s]	%	Time nc [s]	Time c [s]	%
	50 μm thickness			25 μm thickness		
4	680	395	41.91	1357	230	83.05
6	628	485	22.77	1245	350	71.89
8	605	518	14.38	1195	465	61.09
10	590	527	10.57	1171	562	52.01
12	582	542	6.87	1161	638	45.05
14	575	546	5.04	1139	700	38.54
16	573	548	4.36	1135	761	32.95
18	571	552	3.33	1125	802	28.71
20	570	553	**2.98**	1119	840	**24.93**

Table 2.5: Oscillations of a 4-meter long panel (50 μm and 25 μm thickness).

n	Time nc [s]	Time c [s]	%	Time nc [s]	Time c [s]	%
	50 μm thickness			25 μm thickness		
4	1060	293	72.35	2086	185	91.13
6	977	425	56.50	1956	250	87.22
8	949	532	43.94	1875	317	83.09
10	915	603	34.10	1829	400	78.13
12	900	660	26.67	1815	475	73.83
14	889	703	20.92	1793	555	69.05
16	883	729	17.44	1770	617	65.14
18	876	750	14.38	1755	690	60.68
20	875	767	**12.34**	1749	749	**56.78**

Table 2.6: Oscillations of a 5-meter long panel (50 μm and 25 μm thickness).

n	Time nc [s]	Time c [s]	%
	50 μm thickness		
4	1505	235	84.39
6	1405	330	76.51
8	1335	435	67.42
10	1319	525	60.20
12	1300	600	53.85
14	1282	675	47.35
16	1279	744	41.83
18	1276	803	37.07
20	1259	849	32.57
22	1255	887	29.32
24	1252	925	26.12
26	1251	950	**24.06**

Table 2.7: Oscillations of a 3-meter long panel (25 μm thickness). n is the number of elements, time nc and time c correspond to the time needed to reduce the initial oscillation to the 10% respectively in a "non controlled" and in a "controlled" system, and % is the percentage of reduction of the oscillations in the controlled system with respect to the non controlled one.

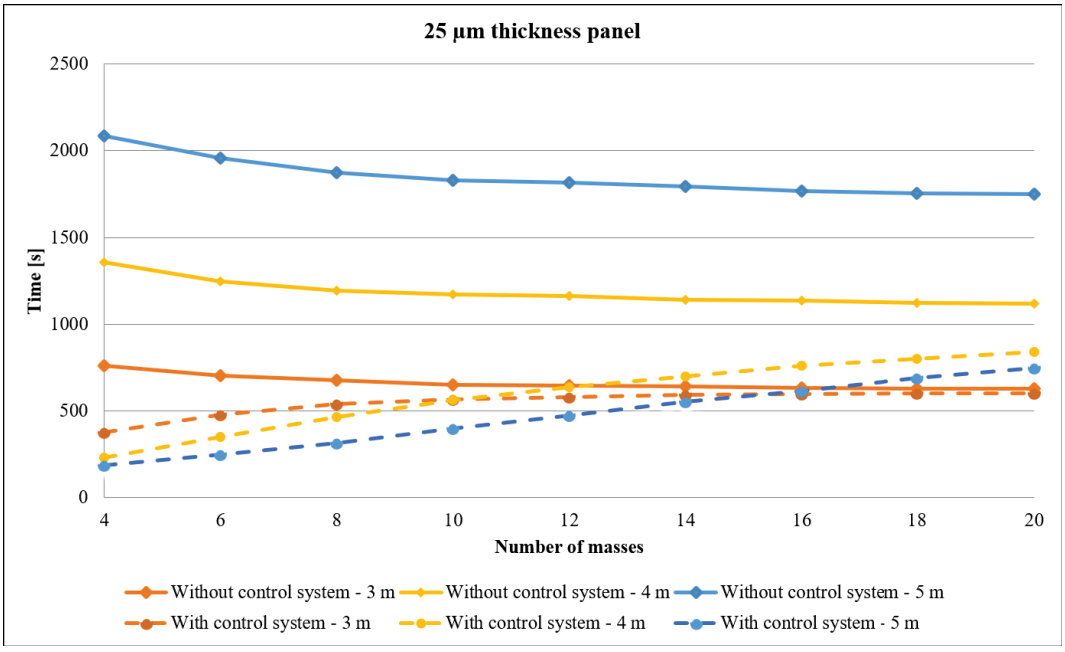

Figure 2.6: The columns time nc and time c of Tables 2.4 to 2.6 for a 25 μm thick panel are reported in this figure.

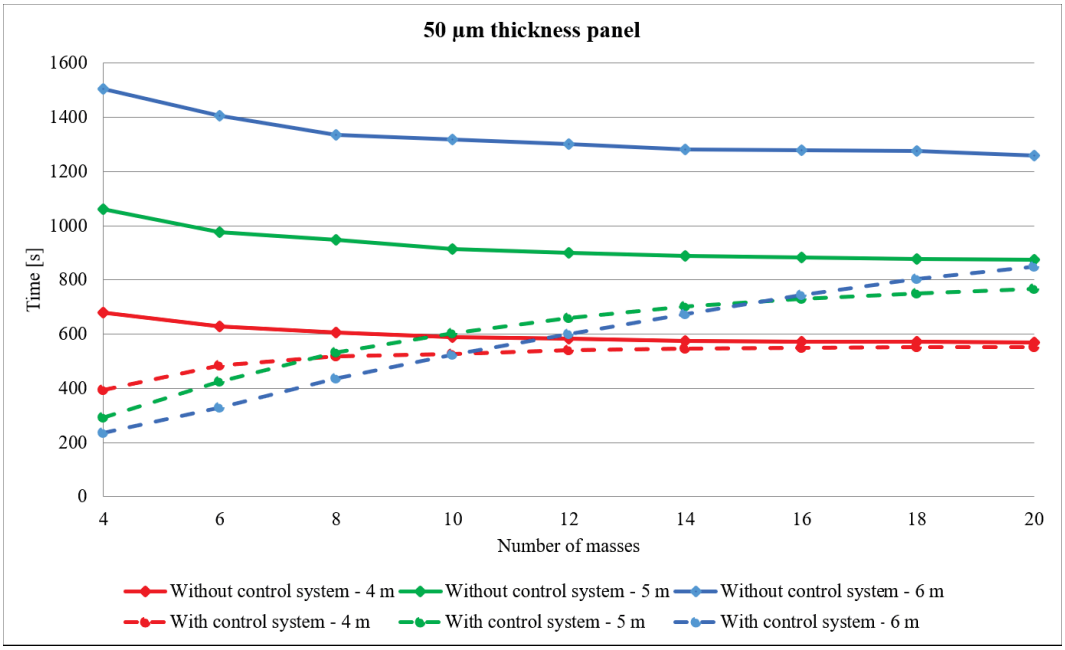

Figure 2.7: The columns time nc and time c of Tables 2.5 to 2.7 for a 50 μm thick panel are reported in this figure.

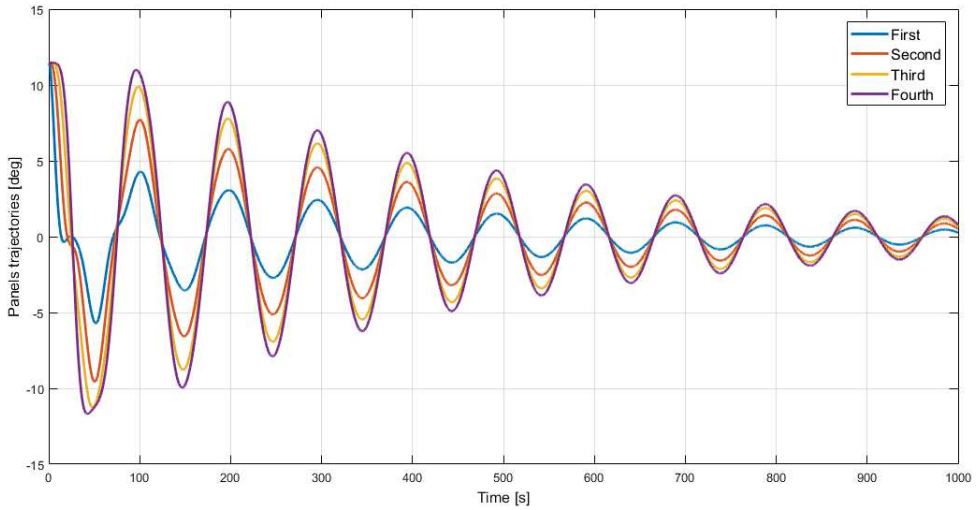

Figure 2.8: Evolution of the position state components (angles) of a 5 m long panel in a "non-controlled" configuration. Each curve refers to one of the masses, being the one that oscillates the most the outer one.

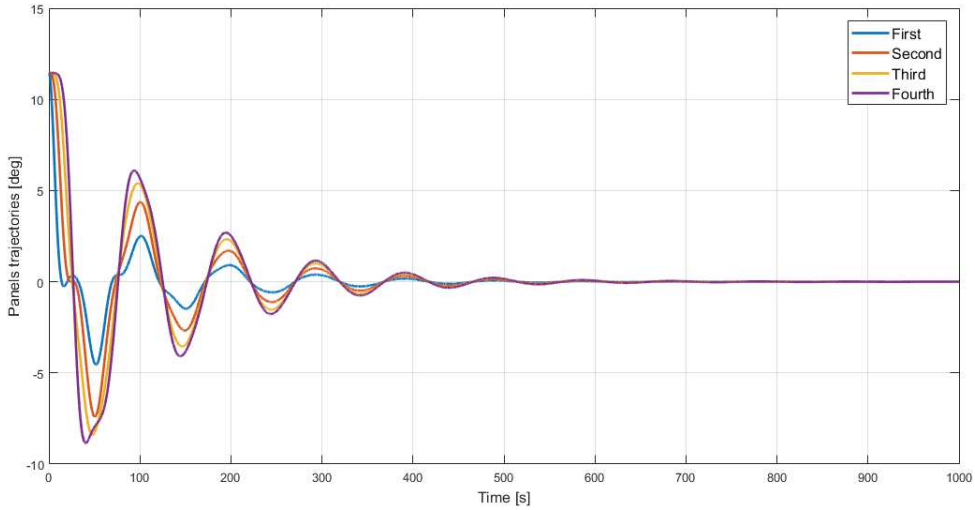

Figure 2.9: Evolution of the position state components (angles) of a 5-m long panel controlled with 4 rows of piezoelectric patches.

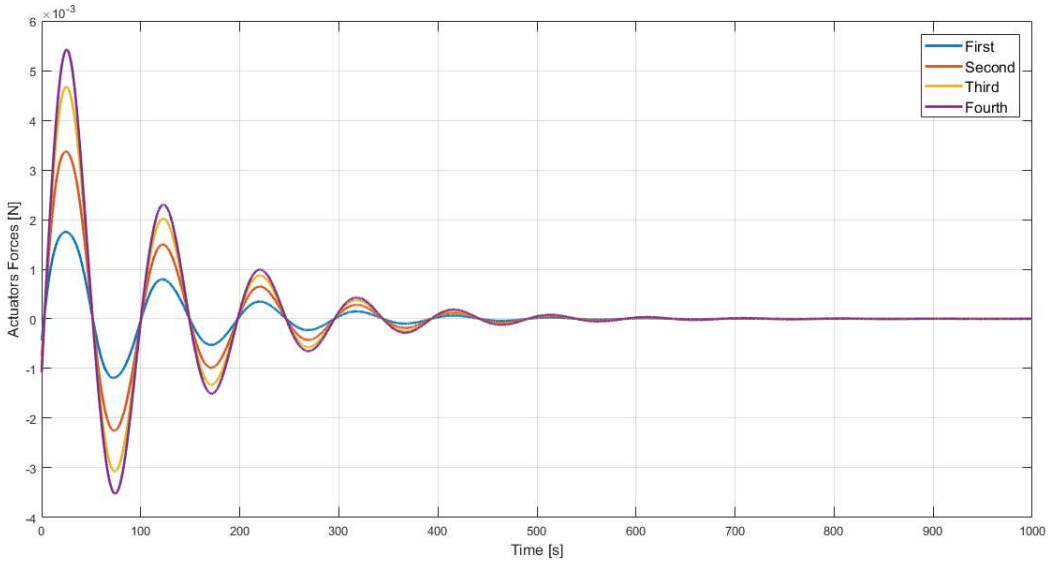

Figure 2.10: Evolution of the actuation forces in case of a 5 m panel with 4 rows of actuators.

L [m]	P_{max} [W]
3	515
4	687
5	858
6	1030

Table 2.8: Power production of two membrane solar panels installed on a satellite, where L is the total length.

displacement of each element in a non-controlled configuration. Figure 2.9 shows the same situation when actuators are used to counteract the oscillations of the panel. Figure 2.10 shows the forces that the actuators are required to exert in order to counteract the external disturbances.

2.4 Possible implementation

Applying this configuration to a possible satellite with two solar panels as appendages that extends from its main body, the power that can be produced from such panels can be calculated as follow:

$$P_{max} = 2 \cdot A \cdot J \cdot \eta \tag{2.23}$$

where A is the area exposed to the solar flux, J is the solar constant, that corresponds to $J = 1367 W/m^2$ and the current record efficiency η for thin-film CIGS solar modules is 15.7% [8]. Therefore, this configuration can be applied to a satellite of small size, with a maximum power available reported in Table 2.8.

2.5 Conclusions

The aim of this first test case is to investigate the behavior of a membrane structure, fixed on one edge, not in tension. This membrane is subjected to a sinusoidal force and non-zero initial conditions on the angular position of its elements. The effectiveness of utilizing piezoelectric actuators distributed on the surface of the membrane was investigated.

This study confirmed the possibility to apply the robust H_∞ closed-loop control

algorithm to actuate a set of piezoelectric patches in order to correct an initial non-horizontal shape of a membrane to reach a flat and well-deployed configuration. The results suggest that applying such a control system to counteract the applied disturbance forces is feasible, and the forces that can be exerted by the actuators are sufficient to reduce the oscillations. In particular, two cases can be identified:

- for *short and thick* membranes, results suggest that the intrinsic damping and elastic behavior of the material is sufficient to counteract such external disturbances;
- when a *thin and long* panel is considered, the piezoelectric patches are more useful to reach a flat deployed configuration in a reduced amount of time compared to a non controlled case.

Further studies are suggested to be carried out in particular for the second case, when a long and thin membrane is used, in order to validate the results of this research and the assumptions that were made in the numerical simulations.

Chapter 3

Membrane with external frame

This Chapter presents numerical simulations and preliminary tests carried out on the *second test case*, that considers a membrane structure deployed and kept in tension by means of two external composite tape springs.

Objective The purpose is to investigate the dynamics of the system from a numerical point of view and to explore the effectiveness of vibration control directly applied to the deployable boom in order to reduce the transmission of vibrations to the central body of the satellite.

Method After manufacturing two tape springs, the mathematical description of these prototypes is presented, to calculate some physical quantities that will be used in following tests and compared to experimental results. Preliminary experimental tests are carried out to obtain some data that will be used in the following numerical simulations and experimental tests.

3.1 Introduction

The system considered in Chapters 3 and 4 includes two tape spring booms, with bistability properties, that deploy from a rotating spool. The current tendency is to miniaturize the system using booms that deploy elastically without the use of a motor. In this thesis, both cases with and without motor were considered. On one side, an uncontrolled deployment allows to save space, mass and power, on the other side the use of a motor allows the control of the deployment speed and to

reduce unwanted shock torques. Previous deployment tests of a membrane structure showed that shock loads due to fast deployments of the booms were a concern for the integrity of the membrane [43]. In addition, the use of a motor allows an easy retraction of the membrane structure whenever needed. The motor, the motion transmission devices and the driving electronics were designed and positioned in such a way to minimize the occupied volume.

3.2 Bistable tape springs

First of all, the booms are analyzed. Composite tape springs employed in the designed system present a characteristic behavior that will be presented in this section. Their dynamics depend deeply on the material and on the size of the booms. Preliminary tests are presented and numerical simulations results are discussed.

3.2.1 Mechanics of bistable composite tape springs

Tape springs are a structural element that has been extensively studied and used for decades in deployable structures in the aerospace industry. Typically, tape springs have a tubular shape. They can be rolled up and deployed, like a standard tape measure, with the difference that they present two stable configurations, both in the coiled and the extended configuration [44]. Tape springs can be made of different materials, from metals [45, 46] to ultra-thin composites.

Bistable tape springs are suitable as deployable structures thanks to their high packaging ratio that allows their storage in a very small volume, low cost, low weight and good stiffness [47]. In addition, they can be stored elastically and the stored energy is released through a single kinematic path [48, 49]. In this work, tape springs made of CFRP are utilized.

A bistable structure presents two configurations of local minima in its stored strain energy, and, therefore, two stable configurations: rolled-up and deployed. The strain energy that they store is released only during the transition between the two stable states. Usually, the local minima do not store the same amount of energy: the higher strain configuration is found typically in the rolled cylindrical configuration, while the low (or zero) energy state is found when the structure has been completely

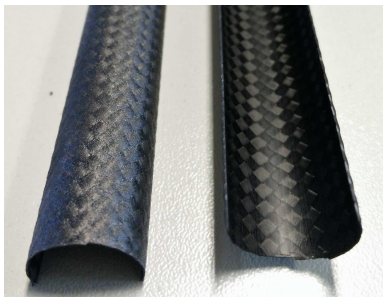

Figure 3.1: Two booms with a focus on the plain weave composite layout.

deployed, which is also the shape they obtain when they are manufactured. The transformation between the two minimum energy configurations takes place in a short transition zone that moves along the structure during the deployment and can be triggered adding a substantial amount of energy to the system, for example, by mechanical loading.

Typically, tape springs used in the aerospace sector are made with traditional fiber-reinforced composites with high strength fibers and aerospace-grade resin systems. The thickness of these laminates is usually very small, because they need to resist large strains without failure. In general, it is desirable that the fibers are arranged anti-symmetrically with respect to the mid plane of the laminate to exhibit a bi-stable behavior and to avoid undesired twisting. Generally, plain weave composites are employed in these structures. In a plain-weave lamina, the material is made of interlacing perpendicular fiber strips, i.e. each warp fiber passes alternately over and under each fill (weft) fiber, like the arrangement of fibers in a textile material. These fabrics are impregnated with a polymer matrix to maintain the integrity of the structure and to distribute the external loads to the fibers. The plain-weave texture is clearly visible in Figure 3.1.

3.2.2 State-of-the-art of bistable tape spring structures

A. Daton-Lovett discovered the key to the bistable behavior of composite shells in 1996 and patented them the next year [50]. His findings have been studied and developed further by Iqbal and Pellegrino [48] and Guest [51]. All these studies attempt to better understand the structural mechanics of these structures, as well as to develop analytical and numerical models to predict their behavior. A lot of

research has been carried out on both the quasi-static and dynamic behavior of tape-springs, but their deployment dynamics has not been fully understood yet, as many variables come into play such as micro-buckling mechanics, viscoelastic effects that cause significant energy relaxation after long stowage periods, and deployment latency [47, 48, 52]. Viscoelastic effects cause a reduction in deployment force and torque after a long period of stowage [47, 53–57]. A reduction of as much as 60% of the stored energy was experimentally observed [58]. This effect might be beneficial in the reduction of the deployment forces and torques due to a fast deployment, but might also fail to deploy from a coiled to an extended state [56, 57].

The uncontrolled dynamics of self-deployed bistable structures can also cause damage to the structure or to the spacecraft and is prone to jamming and failure. The end-of-deployment shock may involve buckling and large rotations [59]. For example, the Mars Advanced Radar for Subsurface and Ionosphere Sounding (MARSIS) mounted on Mars Express that included bistable hinges only partially deployed because of viscoelastic and thermal effects [53, 55]. As it was already mentioned in Section 1.1.1 also the self-deployable ROSA tested by DSS aboard the ISS experienced a failure during retraction after multiple tests in June 2017. However, this was a structure intended to be used on a large satellite, requiring an amount of power on the order of kWs.

Uncontrolled deployments In addition to the ROSA that was tested aboard the ISS, studies on self-deployable booms have been carried out on tape springs at the KTH Royal Institute of Technology in Stockholm with the realization of the Self-Contained Linear Meter-Class deployable (SIMPLE) boom [49, 60–62], a highly compact deployment mechanism with a stowed volume of 38 x 38 x 50 mm^3 to be mounted on a CubeSat. Other deployment tests have been recently carried out by H. Mao [63] for the deployable booms of the Small Explorer for Advanced Missions (SEAM) project. A self-deployed diffraction telescope was also studied by Footdale et al. [43, 64, 65]. This structure self-deploys into an approximately 0.5 m tetrahedron. Concerns were raised when deploying a membrane structure with uncontrolled deployment because of the shock loads that occur at the end of the deployment phase.

Controlled deployments Some motorized deployment have also been performed. Oxford Space Systems (OSS) developed the AstroScale boom [66] for mounting it on the AlSat-Nano [67] and for the Remove Debris Mission [68], as well as to deploy a magnetometer and two RADFET (Radiation-Sensing Field-Effect Transistor) [69]. Another company, ROCCOR LLC worked on deployable booms [70], in particular developing the High Strain Composite (HSC) slit-tube boom system [71].

3.3 Booms prototypes

The booms used for the experimental tests have been manufactured using a single layer of prepreg produced by Hexcel, the HexPly M49, with plain weave P200 carbon fibers. HexPly M49 is a 120°C curing toughened epoxy matrix with 3K high strength carbon. This material was chosen after a careful evaluation of the properties of woven materials readily available at the company selected for manufacturing the booms (SITA Compositi).

The booms were nominally 1 m long, with an internal radius of 7.5 mm. The nominal shape was a half cylindrical tube (C profile). The manufacturing process was similar to the one described by Ekelow in [72]. A pre-preg strip was positioned on the "male" aluminum forming mold (shown in Figure 3.2a) at 45° with respect to its longitudinal direction. The material was cured in an autoclave at 120°C and 5 bar of pressure inside a vacuum bag as shown in Figure 3.2b.

The two booms used for the experiments were observed to be cut about 2 mm away from the perfectly half-cylindrical shape. In addition, the fibers of one of the two booms were not perfectly aligned with the $45°/-45°$ directions with respect to the longitudinal one. This led to a non-perfectly cylindrical shape when the boom was rolled-up and a slightly twisted shape when it was deployed. The booms are shown in Figure 3.3 in both their rolled and deployed configurations.

As expected, the manufactured booms have two configurations of minimum energy: rolled and deployed. The next subsection will give more details about the mathematical description of the tape springs behavior and is needed to calculate physical quantities such as forces and torques that will be compared with experimental results in the next sections.

(a)

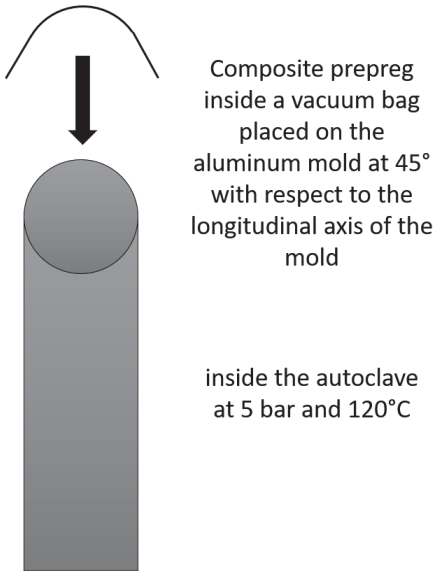

(b)

Figure 3.2: (a) Photo of the mold used to manufacture the bistable boom and (b) sketch of the manufacturing process.

Figure 3.3: Photo of the booms in coiled and deployed configurations.

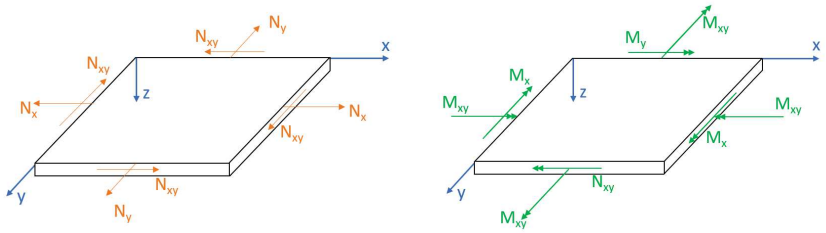

(a) (b)

Figure 3.4: Signs and nomenclature convention for force and moments resultants in the ABD matrix.

3.3.1 Mathematical description of bistable cylindrical shells

Bistable behavior can be described mathematically. Since their behavior is fairly linear within the strain range of interest [44], it is possible to use the Classical Lamination Theory (CLT). The constitutive equations for a thin laminated plate element described by the CLT can be used to describe the linear-elastic behavior of the system, where the main axes coincide with the longitudinal and transverse directions of the shell. The stiffness matrix that relates the generalized strain vector to the generalized stress vector showing the coupling between stress and strain and between moment and curvature is called ABD matrix [73] and follows the convention shown in Figures 3.4. Figure 3.4a refers to the forces, Figure 3.4b to the moments. Each sub-matrix A, B and D is a 3x3 matrix as follows:

$$\begin{bmatrix} N_x \\ N_y \\ N_{xy} \\ \cdots \\ M_x \\ M_y \\ M_{xy} \end{bmatrix} = \left[\begin{array}{ccc:ccc} A_{11} & A_{12} & A_{16} & B_{11} & B_{12} & B_{16} \\ A_{12} & A_{22} & A_{26} & B_{12} & B_{22} & B_{26} \\ A_{16} & A_{26} & A_{66} & B_{16} & B_{26} & B_{66} \\ \cdots & \cdots & \cdots & \cdots & \cdots & \cdots \\ B_{11} & B_{12} & B_{16} & D_{11} & D_{12} & D_{16} \\ B_{12} & B_{22} & B_{26} & D_{12} & D_{22} & D_{26} \\ B_{16} & B_{26} & B_{66} & D_{16} & D_{26} & D_{66} \end{array}\right] \Delta \begin{bmatrix} \epsilon_x \\ \epsilon_y \\ \gamma_{xy} \\ \cdots \\ \kappa_x \\ \kappa_y \\ \kappa_{xy} \end{bmatrix} \tag{3.1}$$

The A portion of the matrix defines the stretching stiffness (in-plane) of the laminate, relating the in-plane forces per unit length to the mid-surface strains. The B-portions of the matrix define the coupling between the bending and extensional stiffnesses. The D portion of the matrix defines the bending stiffnesses of the shell,

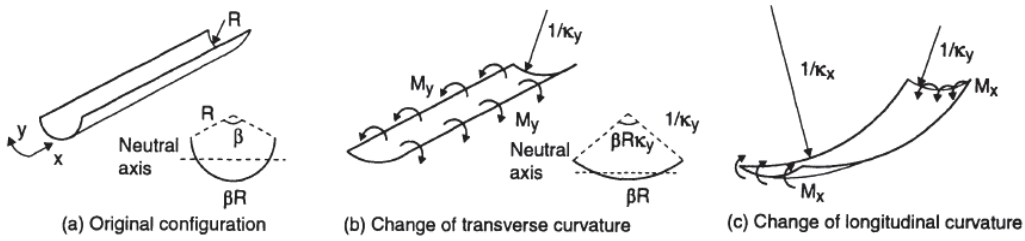

Figure 3.5: Nomenclature used for the bistable boom during its two-step deformation. Image taken from [44].

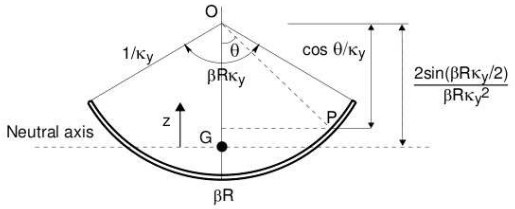

Figure 3.6: Cross-section of the cylindrical shell. Image taken from [44].

relating moments per unit length and change of mid-surface curvature. The properties of each laminate are obtained by integrating the in-plane properties of a single ply through the thickness.

The described ideal model considers a general configuration of the boom with constant longitudinal curvature (κ_x, the inverse of the radius of curvature R_x) and has a radius of curvature $R_y = 7.5$ mm in the transverse, y-direction, and subtends an angle $\beta{=}\pi$. Being the laminate antisymmetric, twisting is not allowed, hence $\kappa_{xy} = 0$. For simplification purposes, stretching-bending coupling is neglected, therefore it is assumed that the B portions of the matrix are 0. The deformation of the shell is divided in two phases:

- bending the shell to flatten it;
- stretching and bending it into the rolled stable configuration.

This process and the nomenclature introduced in this paragraph are shown in Figures 3.5 and 3.6.

3.3.2 Plain weave material properties

This subsection presents the computation of some mechanical properties of the plain weave composite used in the experiments.

As it was mentioned in section 3.3, the composite material is made of 3K high strength carbon fibers. It has an areal weight of 200 g/m^2. A unit cell is formed by warp and weft fibers with a period L=4 mm (according to the datasheet - 5 yarns/picks per cm). The homogenized material properties have been estimated using the fiber volume fraction, that can be found in the prepreg datasheet and it corresponds to $V_f = 0.55$. It can also be calculated and the two values are compared below. The nominal thickness of the fibers bundle (without matrix) is 0.200 mm. The thickness of the yarn t_y is approximated to be half of the thickness of the composite. The cross-sectional area of the yarn A_y can be calculated as:

$$A_y = L \cdot t_y = \frac{4mm}{2} \cdot \frac{0.2mm}{2} = 0.2mm^2 \tag{3.2}$$

where f denotes the fibers, m the matrix, and y the yarn. The diameter of a single filament of carbon fiber is 6.9 μm, therefore, considering a 3K bundle, the area of 3000 fibers is A_f= 0.11 mm^2. The fiber volume fraction is then:

$$V_f = \frac{A_f}{A_y} = \frac{0.11}{0.2} = 0.55 \tag{3.3}$$

which corresponds to the value given by the manufacturer on the datasheet. The matrix volume will be then:

$$V_m = 1 - V_f = 0.45 \tag{3.4}$$

Using the CLT, it is possible to compute the Young's modulus of the composite in 1-direction, that corresponds to the direction perpendicular to the fibers:

$$E_{1y} = V_f E_{1f} + V_m E_m = 0.55 \cdot 231 + 0.45 \cdot 1.06 = 127.53GPa \tag{3.5}$$

with E_{1f} the fiber's longitudinal modulus, E_m the resin elastic modulus, and V_f the fiber volume fraction.

The transverse modulus and the shear modulus cannot be calculated accurately with the CLT, in the 2-direction. They are calculated with the Halpin-Tsai equations:

$$E_{2y} = E_{3y} = \frac{(1 + \xi\eta V_f)E_m}{1 - \eta V_f} = 3.57GPa \tag{3.6}$$

where $\xi = 2$ for circular sections of the filament and η can be calculated as follow:

$$\eta = \frac{E_{2f}/E_m - 1}{E_{2f}/E_m + \xi} \tag{3.7}$$

$$\nu_{12y} = \nu_{13y} = V_f\nu_{12f} + V_m\nu_m = 0.55 \cdot 0.2 + 0.45 \cdot 0.41 = 0.245 \tag{3.8}$$

$$\nu_{21y} = \nu_{12y}\frac{E_{2y}}{E_{1y}} \tag{3.9}$$

The equation to calculate the coefficient ν_{32y} is [74]:

$$\nu_{23y} = \nu_{32y} = \nu_{12y}\frac{1 - \nu_{21y}}{1 - \nu_{12y}} = 0.322 \tag{3.10}$$

$$G_{12y} = G_{13y} = G_m\frac{G_{12f} + G_m}{V_f G_m + V_m G_{12f}} = 1.23GPa \tag{3.11}$$

where G_m and G_{12f} are shear moduli of the matrix and the fibers respectively. in the direction 2-3, the shear modulus is:

$$G_{23y} = \frac{E_{2y}}{2(1 + \nu_{23y})} = 1.35GPa \tag{3.12}$$

3.3.3 Computation of the ABD matrix

With the material properties calculated above, it is now possible to compute the ABD matrix. The two-dimensional approach of the *Mosaic Model* presented by O. Soykasap in [77] was used. In this model, the composite material is considered as a repetition of eight unidirectional subcells, as shown in Figure 3.7. Considering one quarter of the model, with each subcell having the properties of resin-infiltrated yarns with fibers either at 0° or 90°, it is possible to calculate the three matrices A, B and D of the quarter of the model relative to the midplane. In this case, the

Properties	HexTow AS4C GP 3K	Matrix HexPly M49
E_{11} [GPa]	230	3.1*
E_{22} [GPa]	12.97	3.1*
G_{12} [GPa]	11.28	1.1*
ν_{12}	0.3*	0.41*
ρ [kg/m^3]	1780	1180
σ [MPa]	4480	
ϵ_{max}	1.8%	

Table 3.1: Properties of the components of the composite material [75,76]. * values could not be found in the datasheets, hence, they were assumed from typical values.

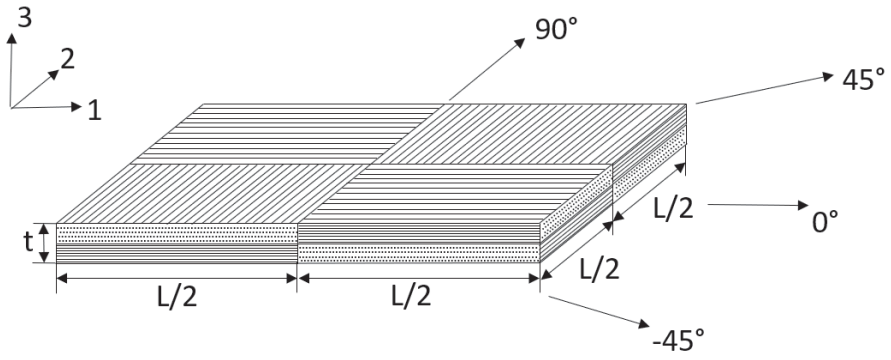

Figure 3.7: Mosaic model of a unit cell.

requested A, B and D matrices need to be calculated at $-45°$ and $45°$ with respect to the unidirectional fibers. This can be done with the following formulas:

$$(A_{ij}, B_{ij}, D_{ij})_q = \sum_{k=1}^{N} \int_{z_k}^{z_{k+1}} \bar{Q}_{ij}^k (1, z, z^2) dz \tag{3.13}$$

where Q_{ij}^{-45} and Q_{ij}^{45} are stiffnesses of the resin-infiltrated fibers respectively at $-45°$ and $45°$ and q indicates the quarter model.

To obtain the homogenized properties, Equation 3.1 is converted to the mixed form:

$$\begin{bmatrix} \varepsilon^0 \\ \dots \\ M \end{bmatrix}_q = \begin{bmatrix} A^* & \vdots & B^* \\ \dots & & \dots \\ C^* & \vdots & D^* \end{bmatrix}_q \begin{bmatrix} N \\ \dots \\ \kappa \end{bmatrix}_q \tag{3.14}$$

where

$$A_q^* = [A_q]^{-1}, B_q^* = -[A_q]^{-1}B_q, C_q^* = B_q[A_q]^{-1}, D_q^* = D_q - B_q[A_q]^{-1}B_q \tag{3.15}$$

where D_q^* represents the bending stiffness with respect to the neutral plane (where N=0). Using the homogenized properties of the yarns, in the case of the fibers in [45°, −45°] direction it results:

$$\Big[A_q\Big] = \begin{bmatrix} A_{11} & A_{12} & 0 \\ A_{12} & A_{22} & 0 \\ 0 & 0 & A_{66} \end{bmatrix} = \begin{bmatrix} 8890.7 & 7525.8 & 0 \\ 7525.8 & 8890.7 & 0 \\ 0 & 0 & 7650.6 \end{bmatrix} N/mm \tag{3.16}$$

$$\Big[B_q\Big] = \begin{bmatrix} 0 & 0 & B_{16} \\ 0 & 0 & B_{26} \\ B_{16} & B_{26} & 0 \end{bmatrix} = \begin{bmatrix} 0 & 0 & -417.21 \\ 0 & 0 & -417.21 \\ -417.21 & -417.21 & 0 \end{bmatrix} N \tag{3.17}$$

$$\Big[D_q\Big] = \begin{bmatrix} D_{11} & D_{12} & 0 \\ D_{12} & D_{22} & 0 \\ 0 & 0 & D_{66} \end{bmatrix} = \begin{bmatrix} 40.568 & 34.34 & 0 \\ 34.34 & 40.568 & 0 \\ 0 & 0 & 34.91 \end{bmatrix} N \cdot mm \tag{3.18}$$

The only difference in the [−45°, 45°] direction consists in the sign of the components of the matrix B_q. The homogenized stiffnesses of the single-ply woven composite in the direction at 45° with respect to the symmetry axes can be obtained by averaging the effective stiffnesses of both [45°, −45°] and [−45°, 45°] quarter models. In conclusion, the ABD matrix of the composite material results:

$$\begin{bmatrix} A & \vdots & B \\ \cdots & & \cdots \\ B & \vdots & D \end{bmatrix}_{comp} = \begin{bmatrix} 8890.7 & 7525.8 & 0 & 0 & 0 & 0 \\ 7525.8 & 8890.7 & 0 & 0 & 0 & 0 \\ 0 & 0 & 7650.6 & 0 & 0 & 0 \\ 0 & 0 & 0 & 17.8 & 11.6 & 0 \\ 0 & 0 & 0 & 11.6 & 17.8 & 0 \\ 0 & 0 & 0 & 0 & 0 & 13.7 \end{bmatrix} \tag{3.19}$$

where the units are N and mm.

3.3.4 Strain energy and bistability properties

The coefficients A_{ij} and D_{ij} computed in the previous paragraph will be used to calculate some coefficients that characterize the employed booms, in particular the strain energy and the S coefficient. The average strain energy per unit area written in non-dimensional form [51] is given by the expression:

$$\hat{U} = \frac{\hat{A}_{11}}{4}\frac{\hat{\kappa}_x^2}{\hat{\kappa}_y^2}\left[1+\frac{\sin(\beta\hat{\kappa}_y)}{\hat{\kappa}_y}-\frac{8\sin^2(\beta\hat{\kappa}_y/2)}{\hat{\kappa}_y^2}\right]+\frac{1}{2}\left[\hat{\kappa}_x^2+2\hat{D}_{12}\hat{\kappa}_x(\hat{\kappa}_y-1)+\hat{D}_{22}(\hat{\kappa}_y-1)^2\right] \tag{3.20}$$

where:

$$\hat{U} = \frac{UR^2}{D_{11}} \qquad \hat{A}_{11} = \frac{A_{11}R^2}{D_{11}} \qquad \hat{D}_{12} = \frac{D_{12}}{D_{11}} \qquad \hat{D}_{22} = \frac{D_{22}}{D_{11}} \tag{3.21}$$

$$\hat{D}_{66} = \frac{D_{66}}{D_{11}} \qquad \hat{\kappa}_y = \kappa_y R \qquad \hat{\kappa}_x = \kappa_x R \tag{3.22}$$

The stability criterion for shells with no coupling between bending and twisting can be computed with the following equation [51]:

$$S = 4\hat{D}_{66} + 2\hat{D}_{12} - 2\frac{\hat{D}_{22}}{\hat{D}_{12}} \tag{3.23}$$

The structure is bistable for $S > 0$. In the case-study presented in this thesis, $S = 1.30 > 0$.

Computing the values of the strain energy $\hat{U}$ from equation 3.20, varying the values of κ_x and κ_y between their minimum and maximum values, it is possible to obtain the plot shown in Figure 3.8. This plot shows:

- the existence of two energy minima in the coiled and deployed configurations;
- a saddle point near $\kappa_x = 0$ and $\kappa_y = 0$.

In addition, it is possible to distinguish the position of the two energy minima (shown with blue and red circles in the plot):

- for $\kappa_x = 0$ and $\kappa_y = 1/R = 1/(7.5mm) = 133.33/mm$, that corresponds to the deployed configuration;

- for $\kappa_x = \frac{1}{R}\frac{D_{12}}{D_{11}} = 86.7/mm$ (i.e. $R_s = 11.5mm$) and $\kappa_y = 0$, that corresponds to the stowed configuration.

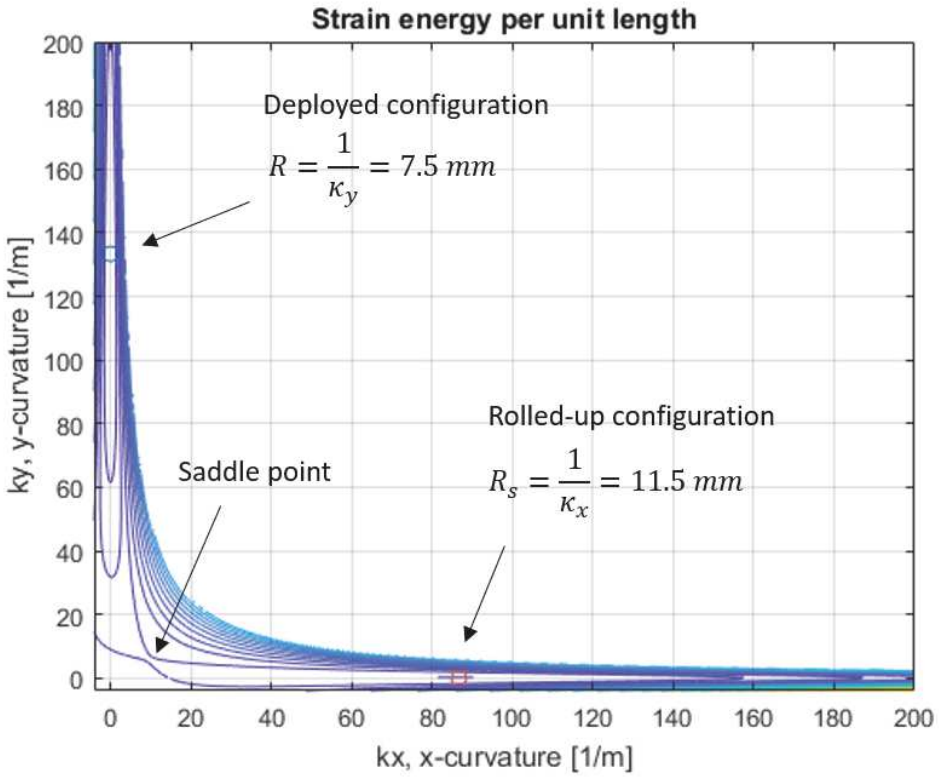

Figure 3.8: Strain energy plot based on the actual properties of the prototypes.

The theoretical deployment force of the tape springs booms can be calculated with the equation [48]:

$$\frac{dU_b}{dL} = \frac{1}{2}\beta R\left(\frac{D_{11}}{R_c^2} - \frac{2D_{12}}{R_c R} + \frac{D_{22}}{R^2}\right) \tag{3.24}$$

with the coiling radius calculated as function of the tape spring length:

$$R_c = \sqrt{\left(R_{spool} + \frac{t_b}{2}\right)^2 + \frac{L_c t_b}{\pi}} \tag{3.25}$$

where R_{spool} is the radius of the spool, t_b is the thickness of the tape spring, L_c is the length of the coiled portion of the boom, and R is the radius of the deployed configuration. The coefficients of the D matrix are $D_{11} = D_{22} = 0.0178$ Nm and $D_{12} = 0.0137$ Nm (see Equation 3.19). The theoretical deployment force derived

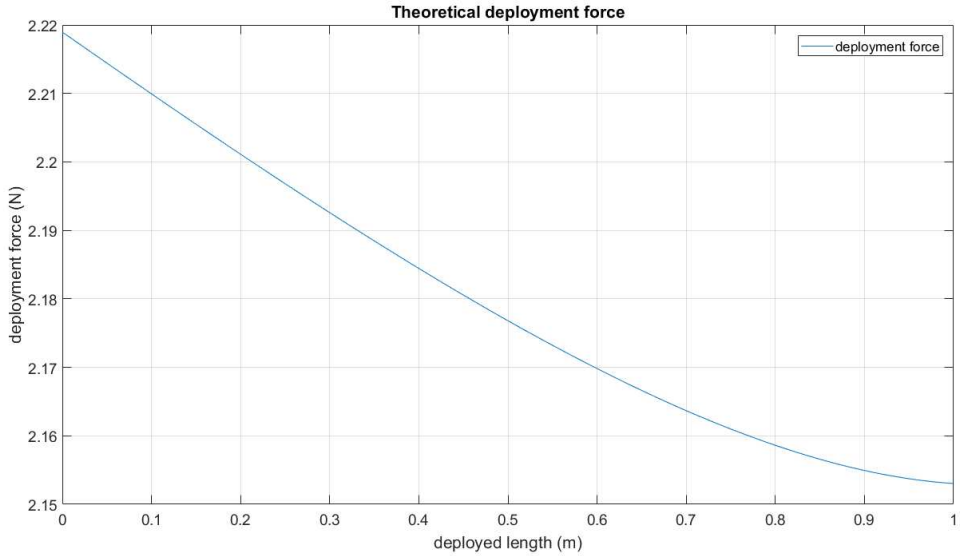

Figure 3.9: Theoretical deployment force.

from Equation 3.24 with the properties of the actual prototypes is shown in Figure 3.9.

Since the deployment force is generated in the unstable transition zone, the deployment torque is related to the wrap thickness, which decreases as the deployment progresses. Therefore, the minimum torque can be found just before the end of the deployment. It can be approximated with:

$$\tau = \frac{R_H \beta}{2R}\left[D_{22} - \frac{D_{12}^2}{D_{11}}\right] \tag{3.26}$$

and in this specific case it results $\tau = 24.8mNm$.

The dynamic equations of a controlled and motorized system based on Equation 3.20 and computed with the Lagrange Equation as the sum of the potential and kinetic energies are reported in Appendix A.

3.4 Preliminary tests

Some preliminary tests were carried out to evaluate the actual properties of the prototypes, considering that it is difficult to calculate them mathematically.

3.4.1 Test 1: evaluation of the elastic and damping properties of the boom

In order to perform the simulations that are presented in Section 3.6 to validate the possibility to damp the oscillations that can occur with a control force directly applied on the boom, it is necessary to evaluate the elastic and damping properties of the actual prototype, that are difficult to find mathematically.

One side of the boom was rigidly fixed to a heavy steel block using a 3D printed structure that held it firmly. The boom was placed in vertical position to minimize the influence of gravity on the measurements, that, as it could be seen in the previous section, influences sensibly the bending of the prototype.

The free length of the boom was 100 cm. The setup can be seen in the 3D model in Figure 3.11a. A small white dot was drawn near the tip of the boom.

To avoid any disturbance to the measurements (and not having other more sophisticated instruments available), a vision system was used. A video camera was placed in front of the tip of the boom, and its first fundamental mode was excited. The video was recorded at **60 frames per second** and was then studied to extrapolate the position of the white dot. An example of frame extracted from the recorded video is shown in Figure 3.11b. 60 frames per seconds are acceptable because, according to the theorem of Shannon-Nyquist, the sampling frequency needs to be:

$$f_s \geq 2 \cdot f_{max} \tag{3.27}$$

where f_{max} was assumed to be between 4 Hz and 5 Hz, according to preliminary simulations performed with Abaqus®, as shown in Figure 3.10. These simulations are not expected to be very accurate because it is difficult to model the properties of the plain weave composite in any FEM software, especially if the principal directions of the material are rotated by 45° with respect to the symmetry axis. However, these preliminary numerical simulations are used as reference for f_{max}.

The results of the measurements are shown in Figure 3.12. A force was applied perpendicularly to the length of the boom to bend it in order to excite its first bending mode. The damping ratio δ was evaluated with the logarithmic decrement

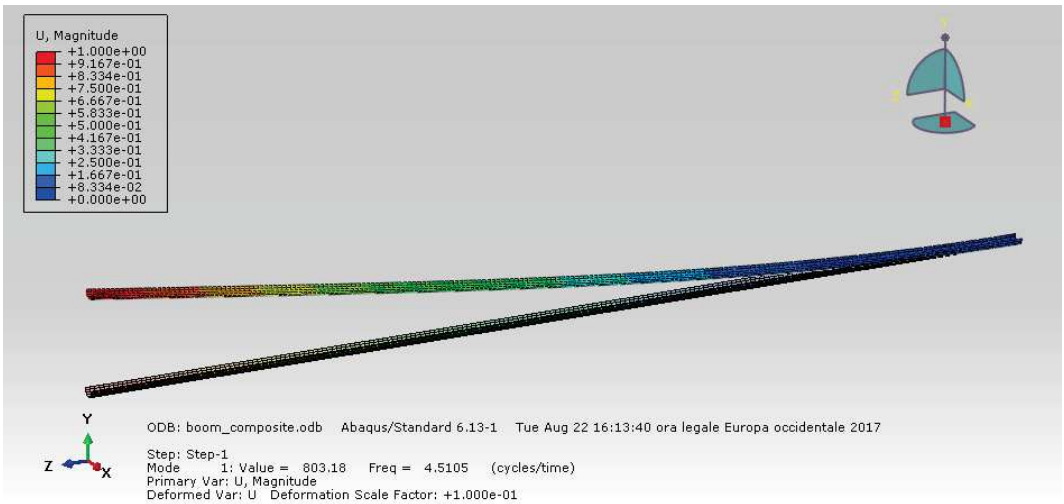

Figure 3.10: Fundamental frequency simulated with Abaqus®.

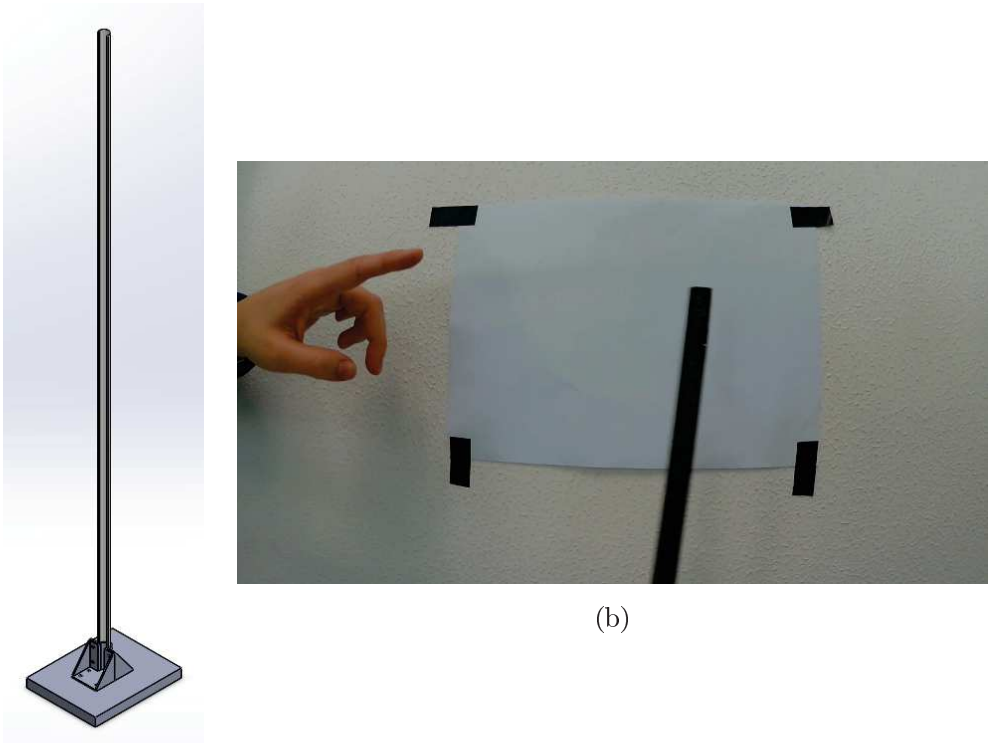

(a) (b)

Figure 3.11: 3D model of the setup (a) and example of captured frame (b).

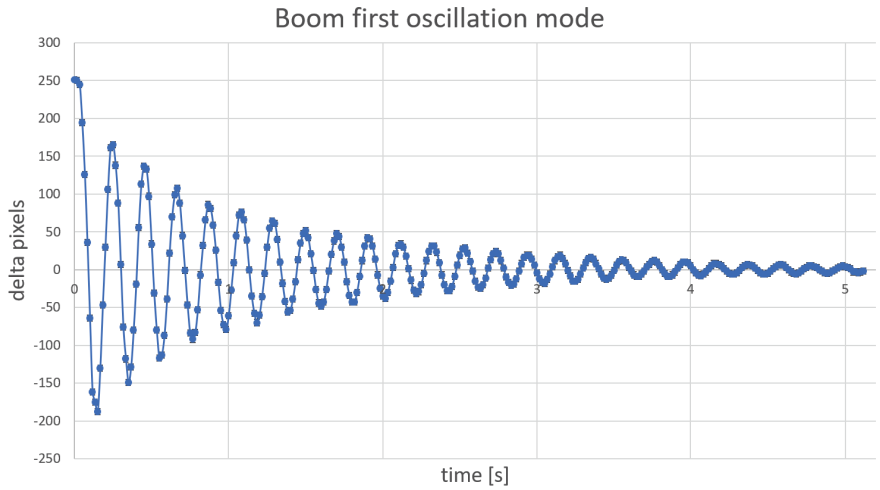

Figure 3.12: Plot of the first fundamental frequency of the boom showing damped oscillations.

method for underdamped systems, that analyzes the y values corresponding to the peaks in the oscillations as follows:

$$\delta = \frac{1}{n} \ln \frac{y(t)}{y(t+nT)} \tag{3.28}$$

where y(t) is the amplitude at time t and y(t+nT) is the amplitude of the peak n periods away, where n corresponds to any integer number of successive, positive peaks. The damping ratio ζ is then calculated from the logarithmic decrement by:

$$\zeta = \frac{1}{\sqrt{1 + \left(\frac{2\pi}{\delta}\right)^2}} = 0.16. \tag{3.29}$$

The damped frequency can be found from the experimental values and corresponds to:

$$\omega_d = \frac{2\pi}{T} = 4.85Hz \tag{3.30}$$

while the natural frequency ω_n can be calculated as:

$$\omega_n = \frac{\omega_d}{\sqrt{1-\zeta^2}} = 4.92Hz \tag{3.31}$$

Analyzing the captured frames, the maximum error in the determination of the position of the small white dot near the tip of the boom used to measure the instan-

taneous displacement was estimated to be ±2 pixels. Considering that every pixel in the captured frames corresponded to 0.15 mm, during the test, the first value of Figure 3.12 corresponds to 250 · 0.15 mm = 37.5 mm. Therefore, the error is negligible compared to the total displacement, especially in correspondence to the first oscillations.

3.4.2 Test 2: boom torques on a fixed spool

The objective of this experimental test is to measure the torque that the motor needs to exert during the deployment of the boom, during the passage from one stable configuration (rolled) to the second one (deployed). This is needed to dimension the motor, that has to be very small in size, but capable to sustain the required torques.

Calibration of the 100g load cell

A micro load cell (Phidget CZL639HD, with max weight capacity = 100 g) was calibrated using three objects with precisely known masses (measured with a scale with 0.0001 g of precision). The cell was connected to the acquisition system Adlink USB-2401 that collected samples at 1000 samples/s. Table 3.2 reports the object numbers (# obj 1, 2, 3 and their sum 1+2 and 2+3; # obj 0 corresponds to the measurement at rest, without mass) with the corresponding measured masses respectively in column 1 and 2. This initial procedure was needed to find the constitutive law of the cell in the range of values of interest (low force values). A set of 50x3 measurements was carried out for each row of Table 3.2, where the average values and the standard deviations are reported.

# obj	m [g]	F[mN]	Average values [mV]	Standard deviations
0	0	0	-4.8931	0.0019
1	2.3031	22.5934	-4.8648	0.0017
2	3.9545	38.7936	-4.8450	0.0020
1+2	6.2576	61.3871	-4.8170	0.0016
2+3	18.4325	180.8228	-4.6700	0.0020
3	14.478	142.0292	-4.7175	0.0020

Table 3.2: Results of the calibration of the 100g load cell.

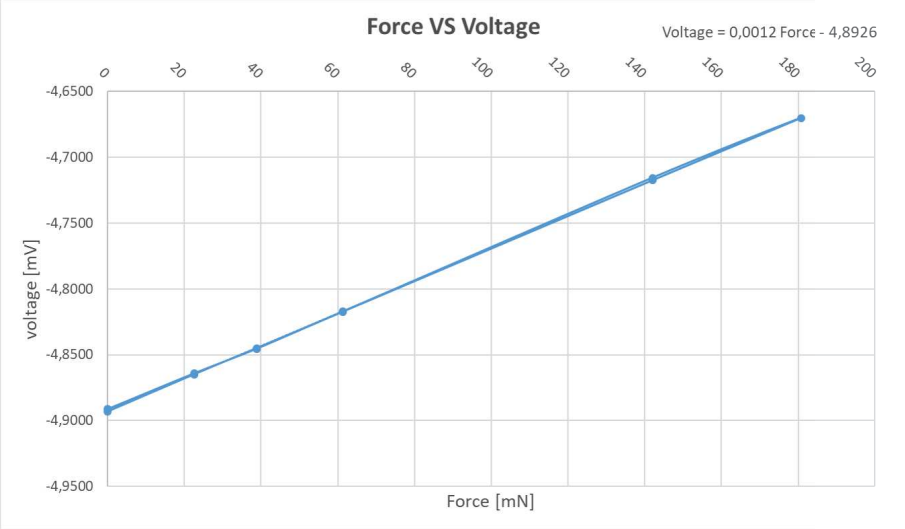

Figure 3.13: Calibration chart of the 100g load cell.

According to the measurements, the cell showed a linear behavior as can be seen in the graph in Figure 3.13 (the one reported here is for the first set of measurements). The third set of measurements was discarded because it showed a different behavior, probably due to systematic errors occurred during the measurements. The constitutive law was then found interpolating the average values:

$$V = 0.0012F - 4.8929 \tag{3.32}$$

with the force measured in mN and the voltage in mV.

Measurement procedure and results

In order to measure this quantity, the boom was rolled up on a fixed 3D printed cylindrical hub, and fixed to it on the tip inside the roll. The load cell was mounted in a fixed position on a support structure (as can be seen in Figure 3.14a), and connected to the acquisition system. The boom was mounted vertically, to avoid the influence of the gravity component in the same direction of the force. If the boom is partially unrolled, it tends to deploy completely, exerting a force in the horizontal direction (as shown in Figure 3.14b). The component of the position vector from the center of the fixed spool to the center of the load cell was measured to be 6.5 cm in the vertical direction. This value, multiplied by the force measured

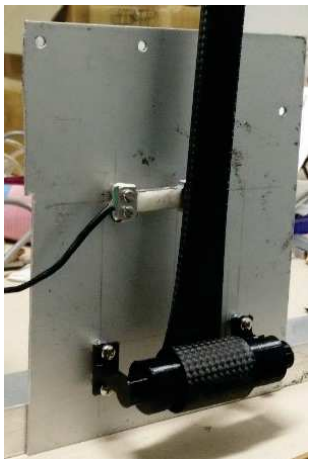

(a)

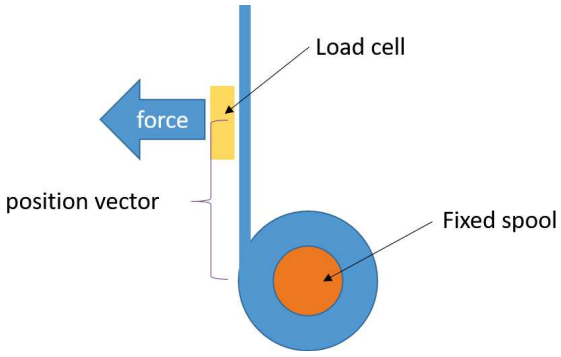

(b)

Figure 3.14: Experimental setup for the load cell.

by the cell, gives the value of the torque needed to keep the boom in that specific position. The measurements were done unwrapping the boom by one wrap for each set of measurements.

The test results showed an irregular behavior, but with a tendency for the force to reduce increasing the deployed length of the boom as expected. The irregular curve could be due to two main reasons:

- imperfections due to manufacturing of the boom;
- the boom was not touching perfectly the load cell (not perfectly vertical).

The results of the measurements are shown in Table 3.3. The graph that shows this behavior (non-linear interpolation line) is shown in Figure 3.15. However, assuming that the behavior is linear (dotted line in the graph), the constitutive law was found to be:

$$T = -0.1021 \cdot length + 13.786 \tag{3.33}$$

with the torque T in mNm and the length measured as the free length from the free tip to the center of the load cell (in the vertical direction) in cm.

However, these measurements were done to have a general idea of the required motor, with the opportune safety factor, so the absolute precision was not regarded

# wraps	d [mm]	Voltage [mV]	F [mN]	T [mNm]
1	28	-4.6673	179.2	11.6
2	127	-4.6497	193.9	12.6
3	209	-4.6633	182.5	11.9
4	294	-4.6988	152.9	9.9
5	381	-4.7388	119.6	7.8
6	461	-4.7052	147.6	9.6
7	540	-4.7419	117.1	7.6
8	615	-4.7608	101.3	6.6
9	689	-4.7702	93.4	6.1
10	758	-4.7867	77.2	5.0

Table 3.3: Results of the measurements of the force on the load cell.

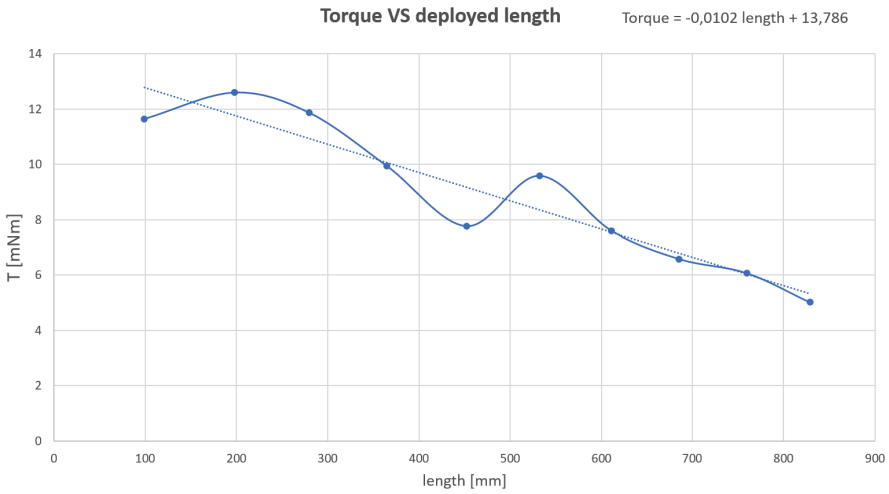

Figure 3.15: Torque VS deployed length measurements results.

as vital. It resulted that the maximum and minimum torques needed to keep the boom in the desired configuration is approximately between 5 and 12 mNm. Multiplying the highest value by a safety factor of 1.5 and multiplying by 2 to consider the presence of the second boom, it results that the motor needs to exert a minimum nominal torque of 18x2=36 mNm.

The measured force results about 10 times smaller than the theoretical force calculated with Equation 3.24, where friction, damping, microcracks and viscoelastic relaxation were neglected. Similar discrepancies were previously observed in [63] and the obtained results were compatible with the values presented in [63].

3.4.3 Test 3: shock loading at the end of the deployment

The purpose of this test was to preliminary measure effect of the shock loading at the end of the deployment on a supporting structure. This was done mounting the boom with its shaft and bearings on a 3D printed structure mounted on two load cells, as shown in Figure 3.16. The boom was positioned in horizontal during the tests, and kept in this position by 0.1 mm diameter cables that sustained its tip end. Since the purpose of this test was to measure only the loading at the end of the deployment and to simplify the experimental setup, reducing the length of the cables to suspend the tip end, the initial configuration for this test was a partially coiled boom.

Calibration of the 780g load cells

Two micro load cells (Phidget CZL616C, with max weight capacity = 780 g) were calibrated using precisely known masses (measured with a scale with 0.1 g of precision), and finding the constitutive law of each cell as it was done for the cells used in the test 2, presented in Section . A set of measurements have been carried out for each row of the table 3.4, where the average values and the standard deviations for each cell are reported. Also during this test, the cells were connected to the acquisition system Adlink USB-2401 that collected samples at 1000 samples/s.

# obj	m [g]	F [mN]	Average values #1 [mV]	Standard deviations #1	Average values #2 [mV]	Standard deviations #2
0	0	0	-4.8053	0.0017	-5.0038	0.0016
1	28.3	277.6	-4.7355	0.0018	-4.9293	0.0017
2	71.2	698.5	-4.6245	0.0016	-4.8167	0.0017
1+2	99.5	976.1	-4.5544	0.0017	-4.7435	0.0016

Table 3.4: Results of the calibration of the 780g load cell.

Measurements procedure and results

A series of measurements have been performed for this test, keeping the boom horizontal and free to move in its axial direction with a 0.1 mm diameter cord that suspended it on its tip free end.

The partially coiled boom was released at t=0 to reach its final extended configuration. A shock load was recorded by the two load cells with a sample rate of 1 kHz. The resulting torques can be seen in Figure 3.18, where the measurements of both the load cells are shown. From this chart, the static components relative to the mass of the system were subtracted from the original sensor output. In such a way, it is possible to compute the total torque generated by the deployment with the equation:

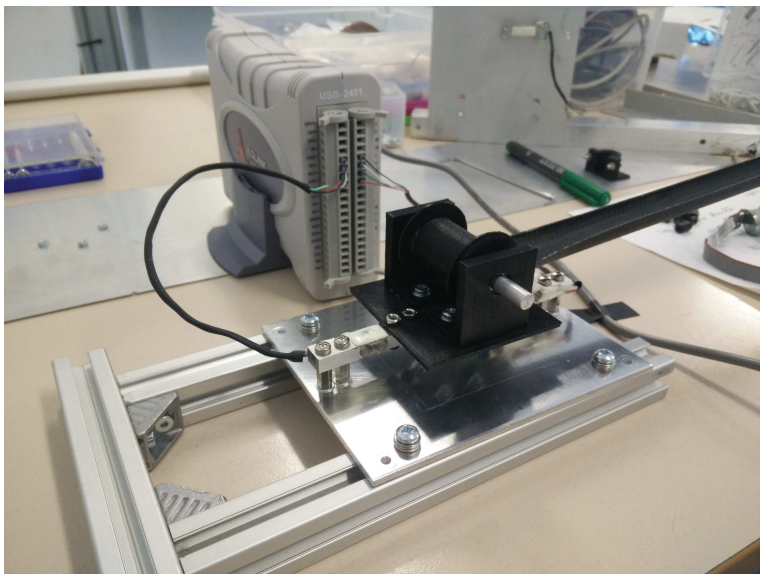

Figure 3.16: Experimental setup for test 3.

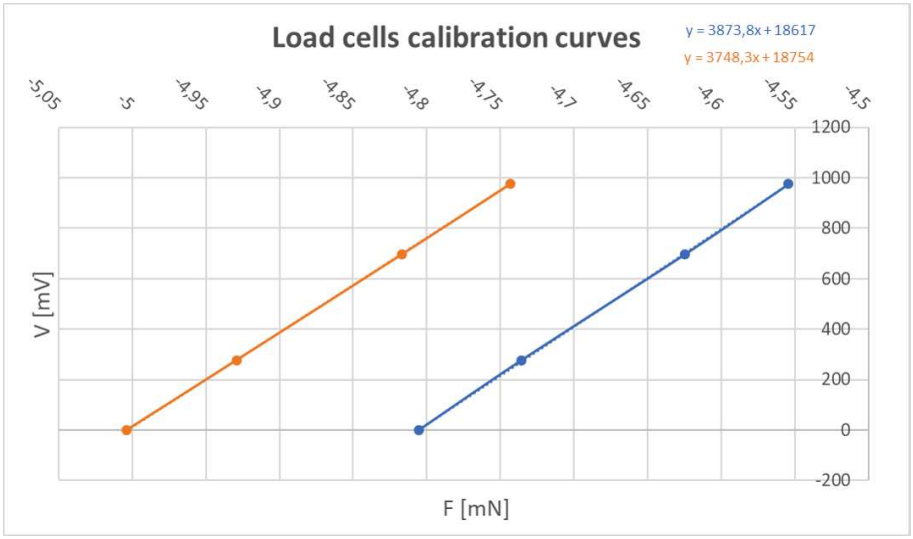

Figure 3.17: Calibration chart of the 780g load cells.

$$T = b_1 \times F_1 + b_2 \times F_2 \tag{3.34}$$

where F_1 and F_2 are the forces sensed by the load cells, and b_1 and b_2 are the moment arms relative to the two load cells with respect to the deployer, that in this case were $b_1 = b_2 = 3.5cm$. From both Figures 3.18 and 3.19, it is possible to see that the shock loading occurs after 0.17 s, which corresponds to an initial coiled length of 21.5 cm.

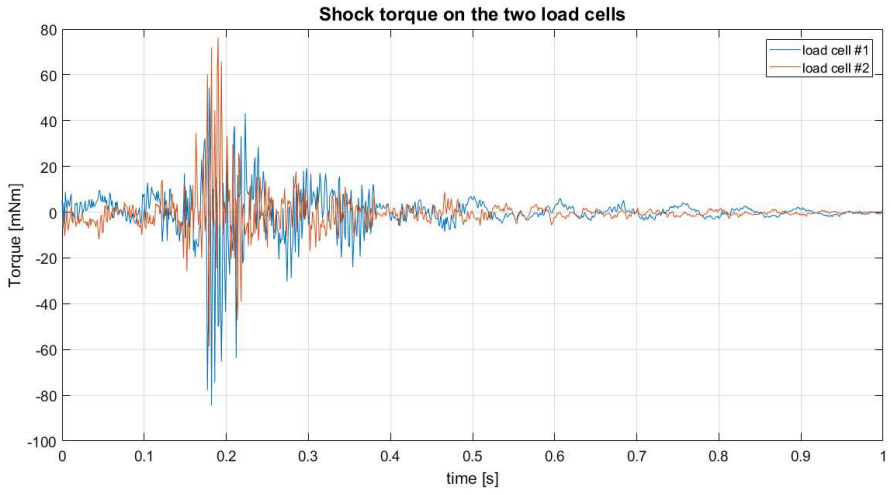

Figure 3.18: Sensors results for the two load cells.

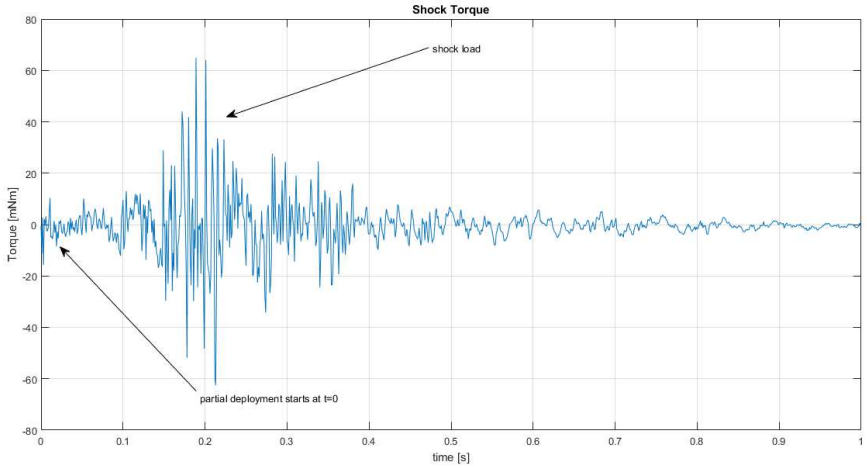

Figure 3.19: Torque during final stage of uncontrolled deployment.

This simple test shows the amount of torque load that can be transmitted to an external structure at the end of the deployment. In this case, torques can reach peaks of 60 mNm. Although the oscillations are damped in $\Delta t < 1$s, this load amount on a small satellite with low attitude control capabilities can potentially lead to uncontrolled rotations of the entire system.

3.5 System dynamic simulations during deployment

The numerical simulations presented in this section have been performed with the multi-body simulator Simscape Multibody® and Matlab®. These simulations investigate how a non-controlled deployment on a nanosatellite can affect its attitude. Comparisons are made with the case of a controlled extension of the appendages.

A 3U CubeSat is simulated in a circular equatorial orbit at 500 km of altitude. The satellite consists of a central body and two identical deployable solar panels that extend in the two opposite y-directions.

In the following paragraphs, details about the satellite, applied torques (due both to the orbital environment and the deployment) and attitude control system are presented in detail.

The satellite body. The central body is defined as a typical 3 units CubeSat, i.e. a 0.3x0.1x0.1 m^3 parallelepiped. Its symmetry axes coincide with the three principal

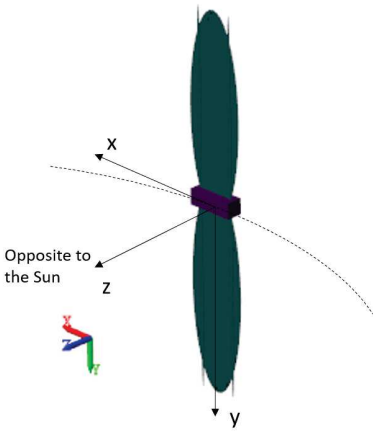

Figure 3.20: Satellite orientation at t=0, with inertial reference frame. At t=0 z points towards the center of the Earth, x is tangent to the orbit and y is perpendicular to the orbital plane.

axes x, y and z of the reference frame, where for t=0, x is in the positive direction of the velocity, z points towards the center of the Earth and y is orthogonal to the orbital plane (see Figure 3.20). Since the body is symmetric along the three axes, the center of the reference frame coincides with the center of mass of the satellite body. A frictionless gimbal joint with three rotational degrees of freedom is positioned on the center of mass of the system.

The solar panels. Each of the two solar panels is composed of three rigid elements: two deployable booms and a membrane. The variation of length of the panels during deployment is simulated employing three variable mass bodies: the center of mass and moments of inertia of the three elements change during the deployment phase of the simulation. Considering the booms rigid and the membrane kept in tension by them, these elements are attached to the body of the satellite through weld joints, that eliminate all the degrees of freedom. This means that the solar panels can only extend from the central body without oscillating around the x-axis.

Each element of a solar panel (membrane, booms) is assumed to be initially wrapped on the same spool as the opposite element of the other panel. The spool is considered for simplicity aligned with the x axis and its center of mass coincides with the center of mass of the whole system.

The orbital disturbances. External disturbances are considered, in particular the gravity gradient, the solar radiation pressure (considering the Earth's umbra period) and drag. These disturbances vary with the rotation of the satellite around its orbit, and with the rotation about its center of mass. The disturbances that depend on the exposed area are only calculated for the membrane, neglecting the components relative to the booms, being their exposed surface sensibly smaller.

Considering that the system is symmetric along the three axes and it can be considered as a single rigid body composed by multiple masses (booms, membranes and central body), the torque due to the gravity gradient was applied to the center of mass of the whole system with the following equation:

$$\vec{G}_{gg} = \frac{3}{2}\frac{\mu}{R^3}\begin{Bmatrix} (I_z - I_y)\sin(2\phi)\cos^2(\theta) \\ (I_z - I_x)\sin(2\theta)\cos(\phi) \\ (I_x - I_y)\sin(2\theta)\sin(\phi) \end{Bmatrix} \tag{3.35}$$

where μ is the Earth's gravitational constant, R is the radius of the orbit (constant if circular), I_x, I_y and I_z are sum of the principal moments of inertia calculated with respect to the center of mass of the system, ϕ, θ (and ψ) are the Euler angles in the body reference frame. The gravity gradient torque experienced by the system during one orbit is shown in Figure 3.21a.

Then, the force due to the solar radiation pressure applied on the center of mass of the two membranes was calculated with:

$$\vec{F}_{srp} = \nu C_R A_\odot P_{rad} \tag{3.36}$$

where $A_\odot$ is the projection of the surface of the panel on the perpendicular plane with respect to the Sun vector, ν is the shadow function, which varies between 0 (shadow) and 1 (light), C_R is a reflection factor that is assumed 1.21 for solar panels, while P_{rad} represents the pressure exerted by the solar radiation on a satellite in Earth orbit, its value being approximately 4.56E-6 N/m^2. The force due to the solar radiation pressure applied on the center of mass of one of the two membranes is shown in Figure 3.21b.

Lastly, the drag force was calculated with:

$$\vec{F}_{drag} = -\frac{1}{2} c_D A \rho_{atm} |v_s|^2 \hat{v}_s \tag{3.37}$$

where A is the projection of the membrane area perpendicular to the direction of the velocity vector, c_D is the drag coefficient assumed to be 1 as the projection of the surface in this case is a rectangle, ρ_{atm} corresponds to the atmospheric density at that altitude, vector $\vec{v}_s$ is the sum of the satellite velocity and the atmospheric velocity due to the winds, that was neglected for simplicity, and $\hat{v}_s$ is the corresponding unit vector. The force due to the drag applied on the center of mass of one of the two membranes is shown in Figure 3.21c.

The orbital attitude. The satellite orbits the Earth with inertial attitude, with the solar panels always perpendicular to the direction of the Sun. The system is shown in Figure 3.22. In normal conditions, the drag and the force due to the solar radiation pressure do not influence the motion of the satellite because their components acting on the two membranes have the same value but opposite sign, thus the sum of their contributions is equal to zero.

Control system. A basic control system was applied to the center of mass of the central body, to represent three ideal reaction wheels actions around the three perpendicular symmetry axes. A PID control system was implemented to counteract the disturbance torques and reduce the pointing errors due to the deployment of the solar panels. The control system scheme is shown in Figure 3.23.

Optimal coefficients K_p, K_d and K_i have been tuned based on automatic calculations made by Simulink®, taking into account the entire system plant. An example of tuning is shown in Figure 3.24.

The reference signals, i.e. the three angles $\phi = \theta = \psi$ were set to zero along all the three axes. The disturbance torques depend on the instantaneous attitude of the satellite.

The torque that the reaction wheels can exert was limited to 0.1 mNm, that is a typical value for CubeSat-sized reaction wheels.

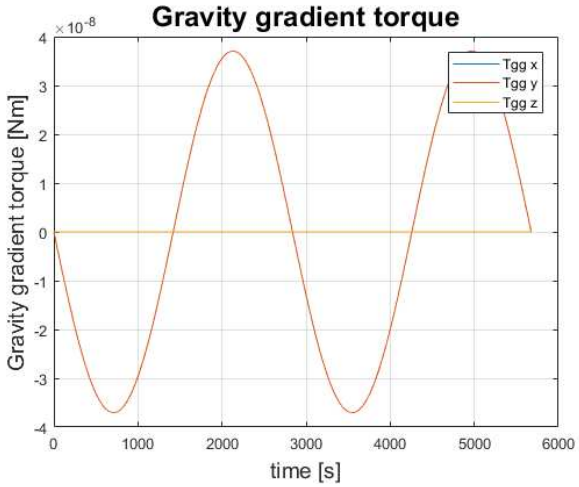

(a) Gravity gradient torques during one orbit. The profile of T_{gg} along x is overlapped by T_{gg} along z.

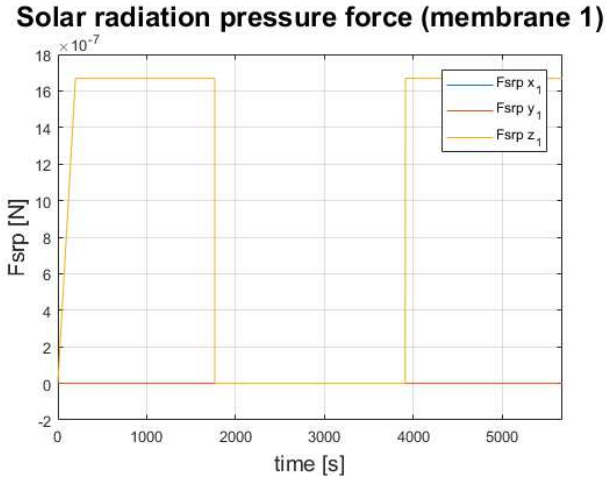

(b) Solar radiation pressure acting on one of the two membranes. The profile of F_{srp} along x is overlapped by F_{srp} along y.

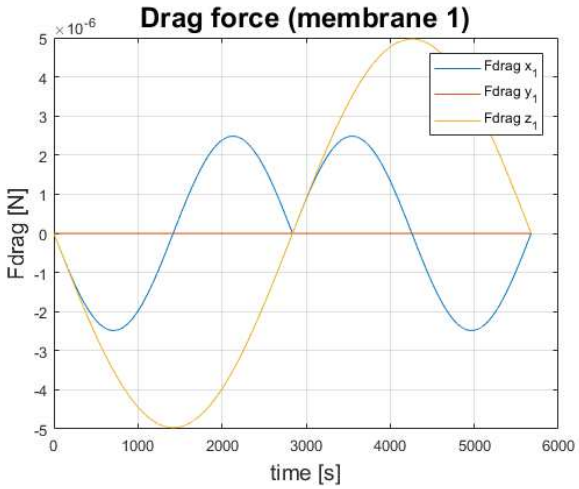

(c) Drag force acting on one of the two membranes.

Figure 3.21: Plot of the orbital disturbances acting on the system.

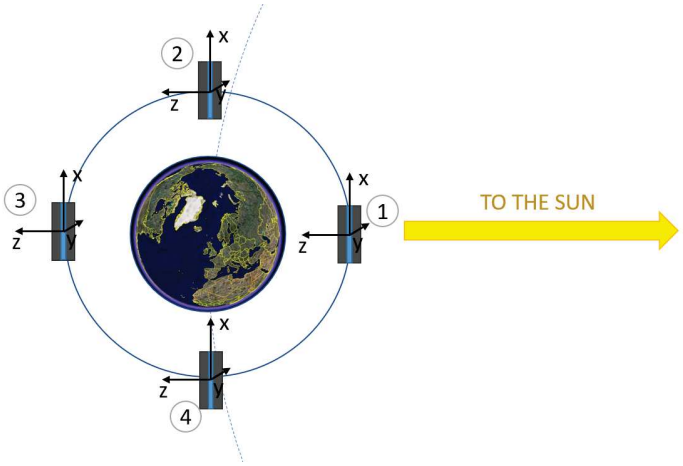

Figure 3.22: Schematic of the satellite orbit around the Earth.

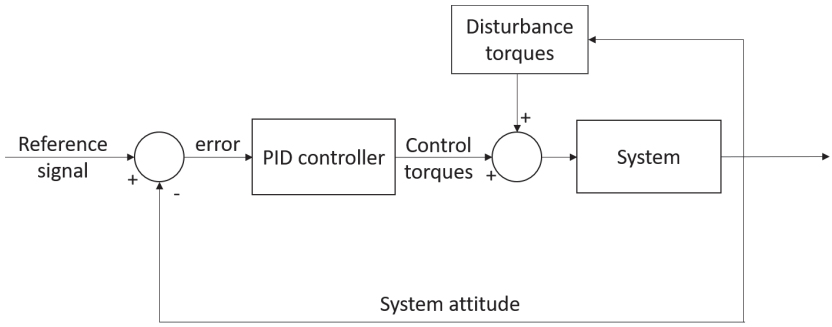

Figure 3.23: Control system deployment scheme.

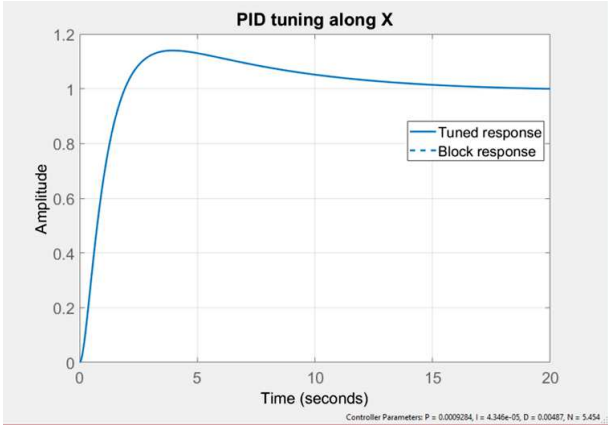

Figure 3.24: Example of PID coefficients tuning around x.

Disturbances due to the deployment. Two disturbance torques that can influence the attitude of the satellite during the deployment phase were identified:

- torque due to the rotation of the shafts inside the satellite;
- torque caused by the shock load at the end of the deployment (only during uncontrolled deployments).

The first component was calculated as:

$$T = I_{xx}\dot{\omega} \tag{3.38}$$

where $\dot{\omega}$ is the angular acceleration during deployment of the rotational elements and I_{xx} is the moment of inertia of the deployer along the x axis. Simplifying the system in Figure 3.26 as a cylinder of 2 cm of diameter and radius r = 30 cm, having the same mass of the corresponding portion of the prototyped system (m = 120 g), it results:

$$I_{xx} = \frac{m \cdot r^2}{2} = 2.4 \cdot 10^{-5} kg \cdot m^2. \tag{3.39}$$

In the controlled case, the linear velocity of deployment of the appendages was assumed to be constant (in this case v = 5 mm/s), with an initial acceleration and final deceleration, as it is shown in Figure 3.25a. With this velocity, the total deployment time resulted 216 s. Considering that the diameter of the wrapped portion of the boom reduces during the deployment, the angular velocity of the shaft will have to increase to maintain a constant deployment rate, as shown in Figure 3.25b. For simplicity, the angular velocity was considered to increase linearly between t and t_1 (end of deployment acceleration) and to decrease linearly between t_2 (start of deployment deceleration) and t_{depl}. Since the angular acceleration between t_1 and t_2 would have been much smaller compared to the angular acceleration during the beginning and end phases of the deployment, it was assumed to be zero.

In the uncontrolled case, since the angular acceleration was not known, knowing the angle that the spool needs to rotate to deploy the panels (θ=66.51 rad) and the deployment time ($t_{depl} = 1s$), it was assumed to be constant during the deployment, calculating it with equation:

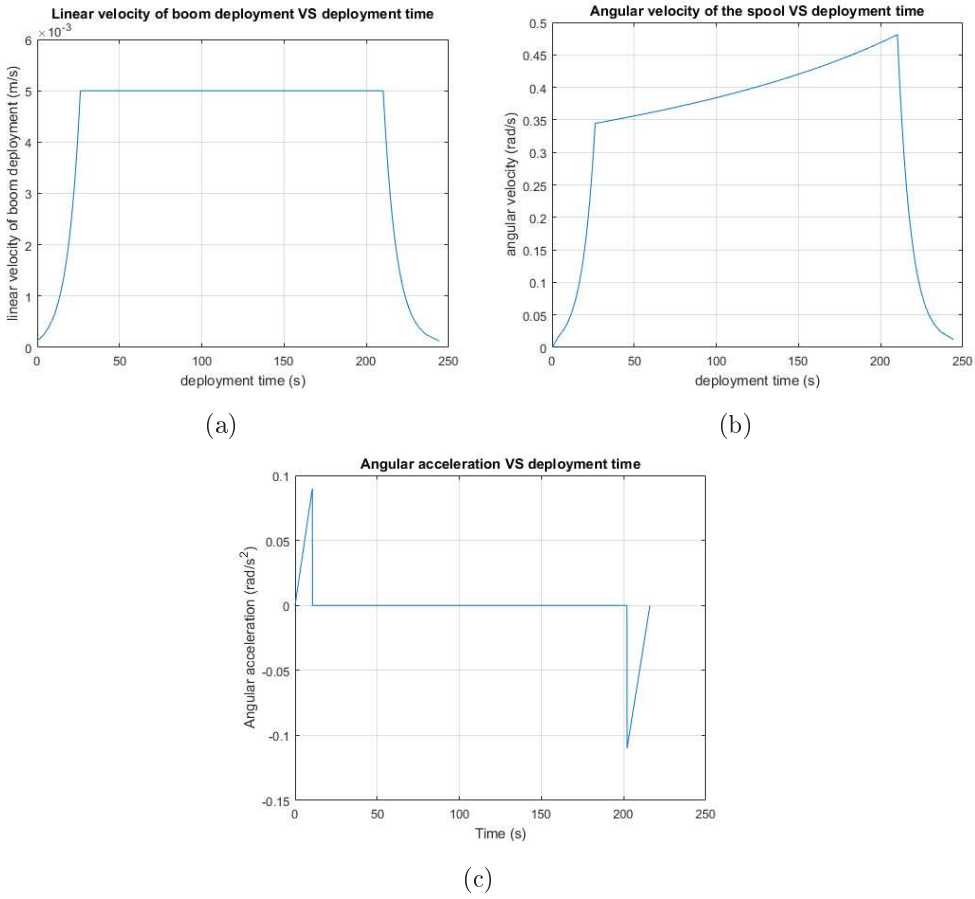

(a) (b)

(c)

Figure 3.25: (a) Linear velocity of deployment of the panels, (b) spool angular velocity and (c) the angular acceleration during deployment in the controlled case.

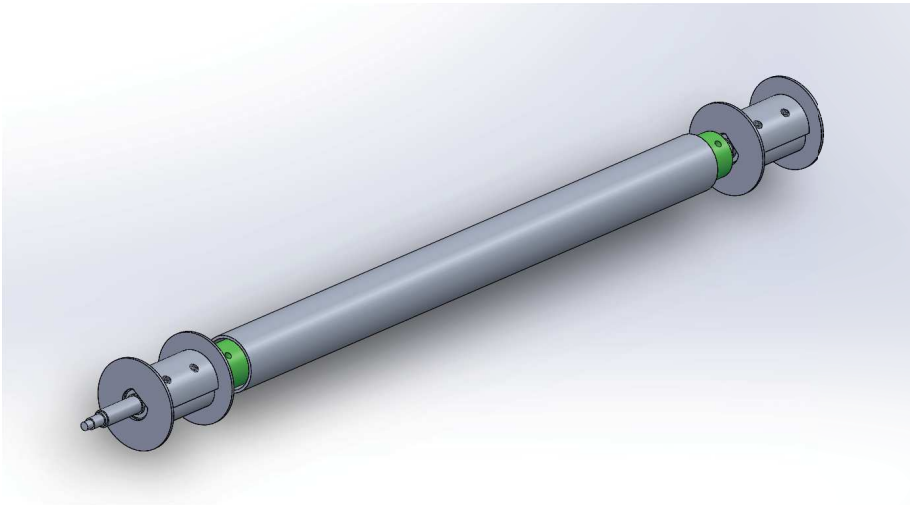

Figure 3.26: Rotating elements during the deployment.

$$\alpha_{nc} = \frac{2\theta}{t^2}. \tag{3.40}$$

The second component was extracted from the data reported in Figure 3.19. An integral of the data between t = 0.15 s and t = 0.21 s gives a total torque due to the shock load that corresponds to $T_1 = 0.0629$ mNm that are given in input to the simulation at the end of the deployment, when $t = t_{depl}$. T_1 is given for one boom: in the simulations, this value has to be multiplied by 4 to take into account the 4 booms, i.e. 2 for each membrane: $T_4 = 4 \cdot T_1$.

An example of deployment sequence is shown in Figure 3.27.

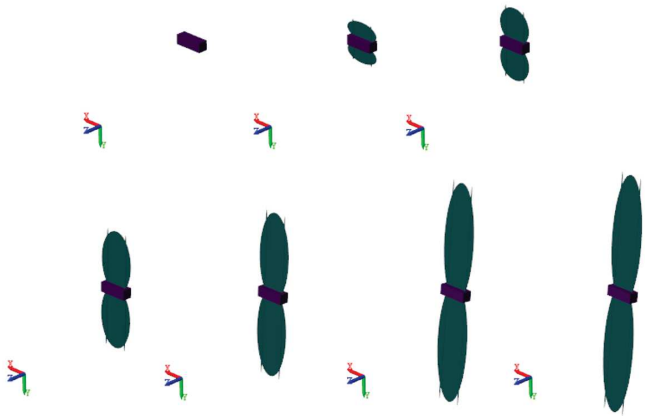

Figure 3.27: Simulated deployment sequence: the membrane and booms are represented by inertial ellipsoids.

3.5.1 Uncontrolled deployment results summary

The results of the simulations carried out for the uncontrolled case demonstrate that the effects that the disturbance torques exert on the satellite cannot be controlled with a typical set of three Cubesat-sized reaction wheels of 0.1 mNm. Even though the disturbance torques due to the deployment last only for $t_{depl} + t_{shock}$ ($\simeq 1s$), the satellite starts to rotate in an uncontrolled way, with the saturation of the controller. During the uncontrolled rotations around its center of mass, the external disturbances become very influent, adding a destabilizing action to the system.

Figure 3.28 shows the attitude of the satellite in terms of angles between the inertial reference frame and the body frame that in this case is fixed with the satellite orientation. Figure 3.29 shows the torques that are transmitted by the solar panel during the deployment. Figure 3.30 shows the control torques limited to 1 mNm, that are not sufficient to stabilize the system. The following Figures 3.31, 3.32 and 3.33 show respectively the torque due to the gravity gradient and the components of the forces due to the drag and the solar radiation pressure. Clearly, being the entire system a rigid body, the forces applied to the two membranes result the same.

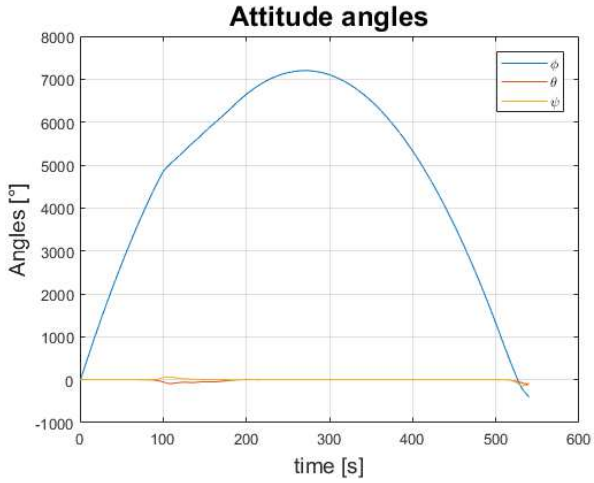

Figure 3.28: Attitude of the satellite with uncontrolled deployment.

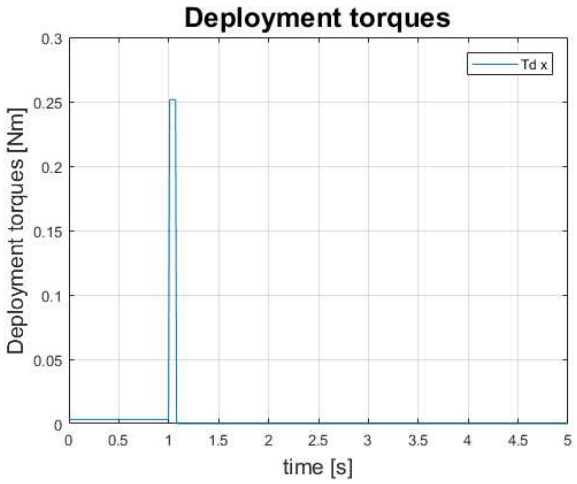

Figure 3.29: Deployment torque during uncontrolled deployment.

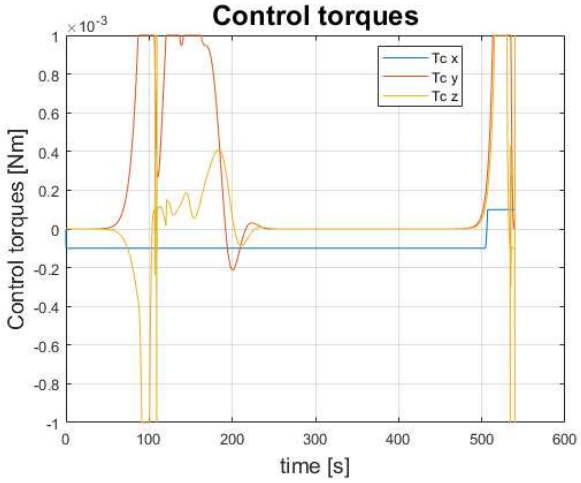

Figure 3.30: Control torques during uncontrolled deployment.

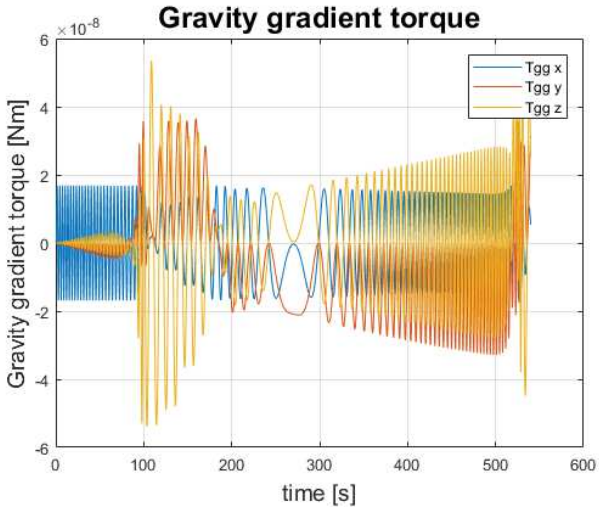

Figure 3.31: Gravity gradient torques during controlled deployment.

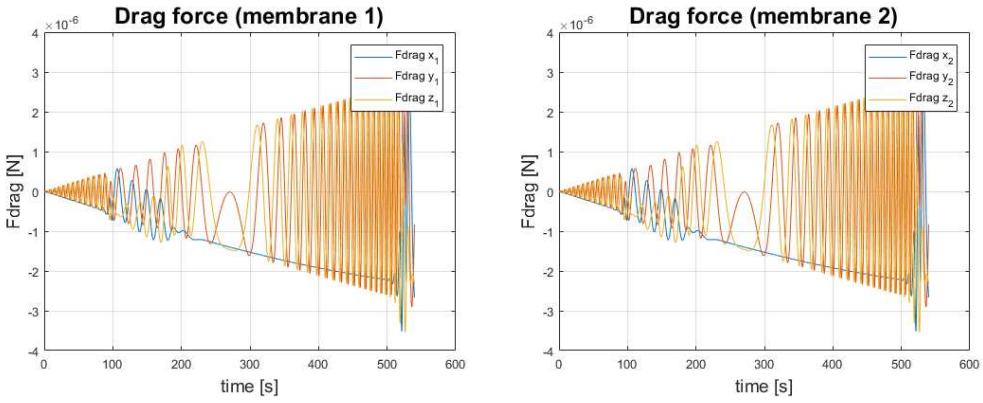

(a) (b)

Figure 3.32: Drag forces applied to the two membranes.

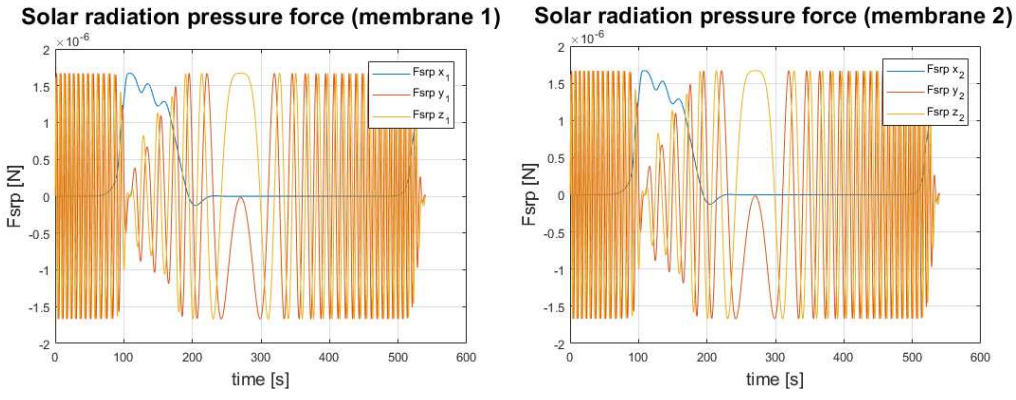

(a) (b)

Figure 3.33: Solar radiation pressure forces applied to the two membranes.

3.5.2 Controlled deployment results summary

The results of the simulations of the controlled deployment show that the torques exerted during the extension of the solar panels can be efficiently controlled with the considered control system. As previously mentioned, the only component of the disturbance in this case is due to the angular acceleration of the shaft.

Figures from 3.34 to 3.39 report the results obtained during one quarter of an orbit, to better show the effects of the deployment and control torques during t_{depl}. Figure 3.34 shows the attitude of the satellite in terms of angles between the inertial reference frame and the body frame that in this case is fixed with the satellite orientation. The torques applied to the satellite at the beginning and at the end of the deployment can be controlled (shown in Figure 3.35) very efficiently with the ideal reaction wheels, that in this case need to exert very small torques with a magnitude of about 2 E-6 Nm. These torques are shown in Figure 3.36. This Figure shows also a smaller sinusoidal control torque around the y-axis to counteract the gravity gradient contribution. The following Figures 3.37, 3.38 and 3.39 show respectively the torque due to the gravity gradient and the components of the forces due to the drag and the solar radiation pressure. As before, being the entire system a rigid body, the forces applied to the two membranes result the same.

Similar numerical simulations based on a system that can control the deployments and retractions of the panel were performed to evaluate the feasibility of controlling the attitude of a 3U CubeSat subjected to typical orbital disturbances in LEO through morphing, i.e. changing the size of the solar panels ideally rolling and unrolling them with a motor. The simulations and their results are reported in Appendix B.

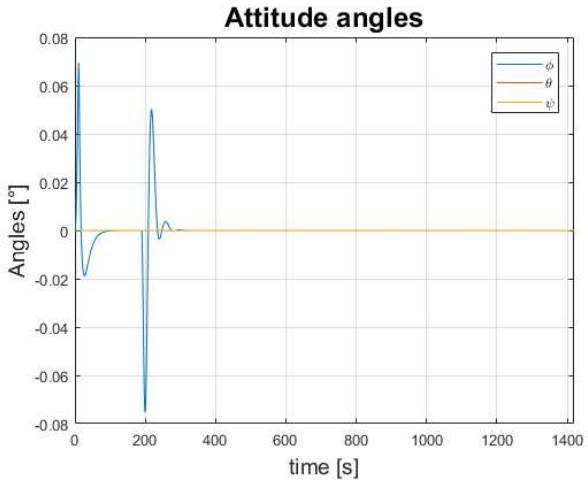

Figure 3.34: Attitude of the satellite with controlled deployment in one quarter of an orbit.

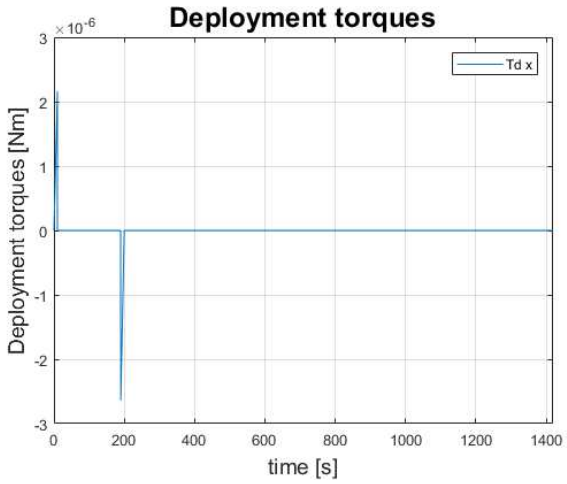

Figure 3.35: Deployment torque during controlled deployment in one quarter of an orbit.

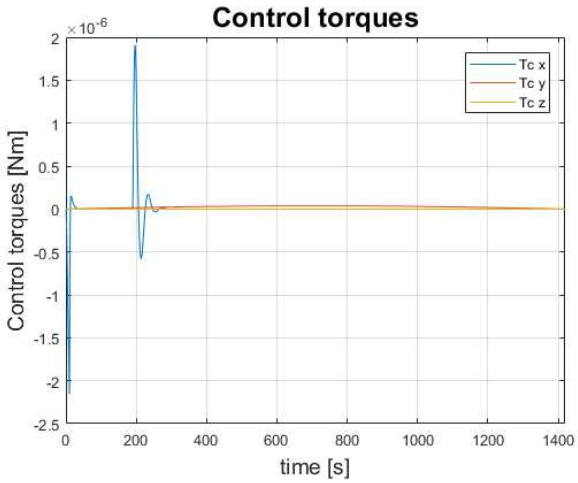

Figure 3.36: Control torques during controlled deployment in one quarter of an orbit.

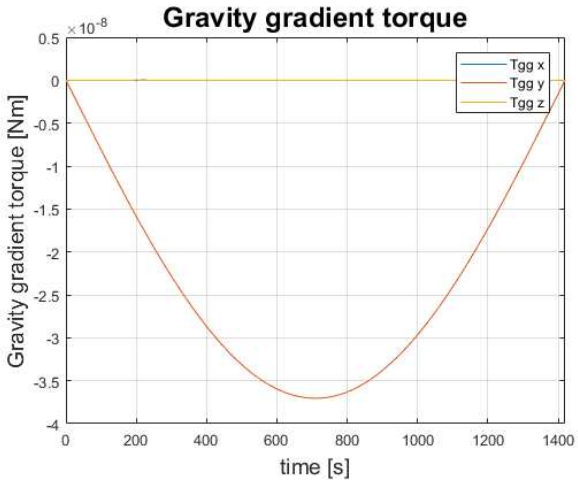

Figure 3.37: Gravity gradient torques during controlled deployment in one quarter of an orbit.

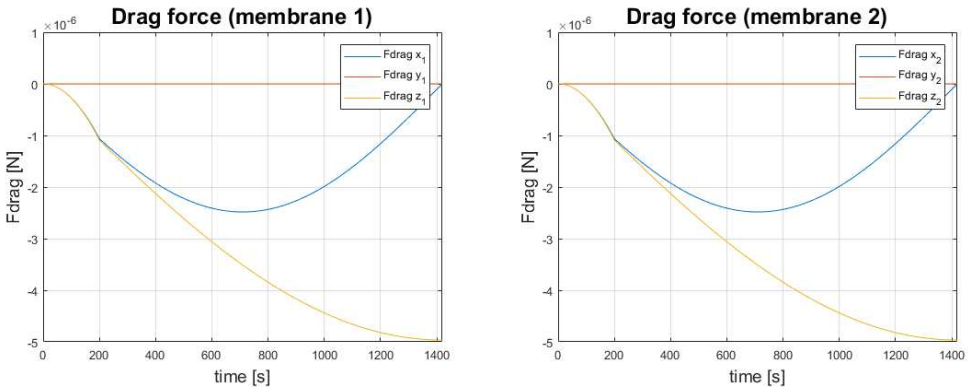

(a) (b)

Figure 3.38: Drag forces applied to the two membranes in one quarter of an orbit.

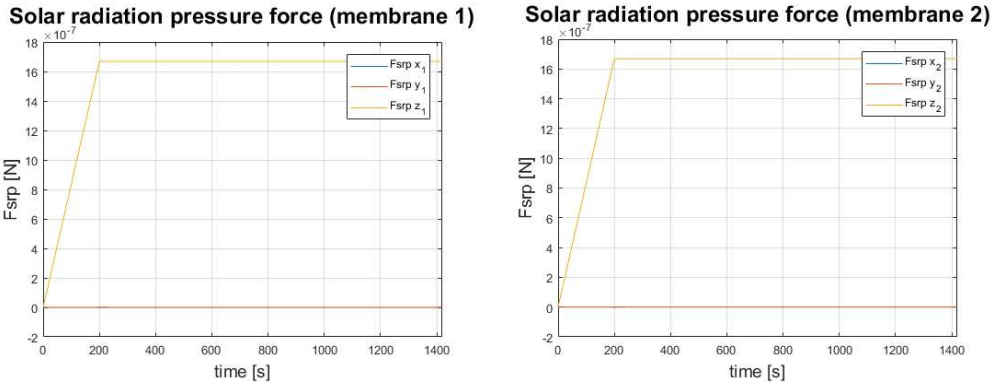

(a) (b)

Figure 3.39: Solar radiation pressure forces applied to the two membranes in one quarter of an orbit.

3.6 Numerical simulations with control system applied to the boom

Using the results of the preliminary test 1 presented in Section 3.4.1, numerical simulations have been performed using the software Matlab® and Simscape Multibody®, the same multi-body simulator used for the simulations in 3.5. The aim of these numerical simulations is to study a possible controller to reduce the oscillations of the boom in case of large oscillations, in order to reduce the external disturbance that can be transmitted to the central body, especially in the case of a small spacecraft.

3.6.1 Numerical simulations

Firstly, the real prototype has been approximated with a mass-spring-damper model respectively fixed and free on the two tip ends. The mass and moments of inertia of the body were given in input from a SolidWorks® model, where semi-cylindrical shells of different lengths replicated portions of the real prototype in terms of dimensions and density (d = 1510 kg/m^3). Figure 3.40 shows the symmetry axes of the half-cylindrical shell. In the simulations, the boom has a total length of 1 m and is divided in 11 elements as shown in Figure 3.41:

- the 2 elements near the fixed side, with length of 5 cm;
- 9 elements with length 10 cm.

The first mass is fixed to the "ground", while all the other masses are connected to the adjacent with a rotational joint, that is defined in terms of its bending stiffness and damping coefficients. This model is equivalent to a cantilever beam, with semi-circular section. The bending stiffness can be calculated with:

$$k = \frac{EI}{L} \tag{3.41}$$

where E is the Young's Modulus of the material, I is the second moment of area (in m^4) and L is the length of the element. Being the section of the elements the same along the length L, I remains the same for beams with different length, E is a

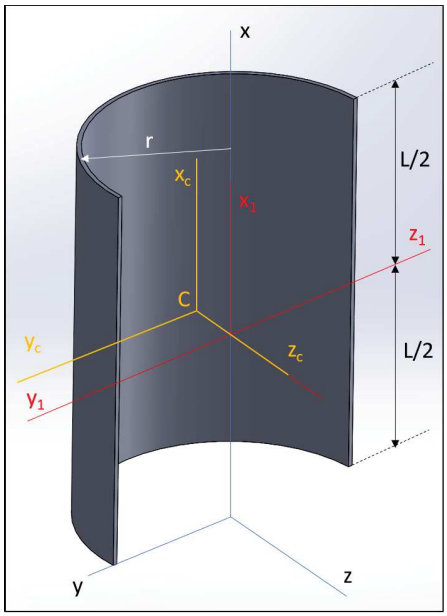

Figure 3.40: Half cylindrical shell symmetry axes.

property of the material, hence k varies with the length: a shorter element will have joints with higher elasticity coefficients. In this case,

- $k_5 = 10.60$ N · m/rad, for the two 5-cm long elements,
- $k_{10} = 5.30$ N · m/rad for the nine 10-cm long elements.

while the damping coefficient resulted d=0.012 N · m /(rad/s). Figure 3.42 shows how the behavior of the simulated boom approximates well the oscillations measured in Test 1 with the actual prototype when the same initial displacement was applied.

A PD controller was tested and its performances in the reduction of the oscillation forced by different loads at t = 0 s were evaluated. The direction of the applied force load was perpendicular to the tip of the boom in the z-direction, upwards. A force that balanced the displacement in z-direction was applied to the boom to counteract this displacement. This force was applied 6 cm from the fixed tip, that is equivalent to 1 cm from the first revolute joint. This point was chosen because applying it to any point of the element fixed to the ground would not have sorted any effect and in a possible real application this force is required to be applied the closest possible to the fixed end. The PD controller was tuned for the force to be

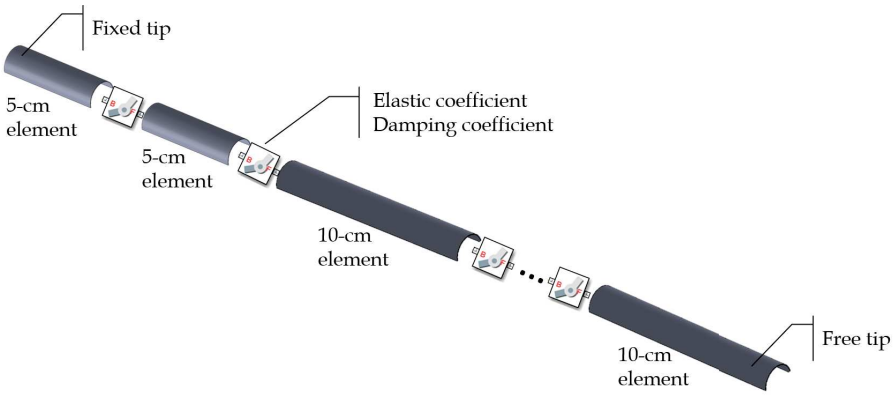

Figure 3.41: Sketch of the simulated system.

applied to this specific point, and if the application point changed the K_p, K_i and K_d coefficients would have to be properly tuned. In this case, optimal PD coefficients were found with a trial and error method (often used in the tuning of PID controllers). Figures 3.43 and 3.44 show a comparison in terms of oscillations at the tip end (left) and the force application point (right) between the uncontrolled case (in blue) and three different combinations of proportional and derivative coefficients, when a 0.2 N force was applied for 0.01 s at the tip end. In Figure 3.43, the results were obtained varying K_p (K_{p1}=0,K_{p2}=80,K_{p3}=800) and keeping K_d fixed (K_{d1}=K_{d2}=K_{d3}=20). On the contrary, in Figure 3.44, K_p is fixed (K_p = 800) while K_d varies (K_{p1}=5,K_{p2}=10,K_{p3}=20). For K_d>25 the system does not converge to zero.

Figures 3.45 show the behavior of the system when different forces were applied to the tip end, and the corresponding uncontrolled responses both at the tip end and at the force application point. In this case, the load force was F_1=0.2 N, F_2=0.5 N, F_3=1 N and the same PD coefficients K_p=800 and K_d=20 were used.

3.6.2 Summary of the results

In conclusion, from the numerical results, it is possible to see that the oscillations can be reduced very efficiently with a simple PD controller that simulates the application of a force load to counteract the external forced load at the tip end. However, with the incrementation of the two controller coefficients also the force that is needed to control the displacement at the force application point increases.

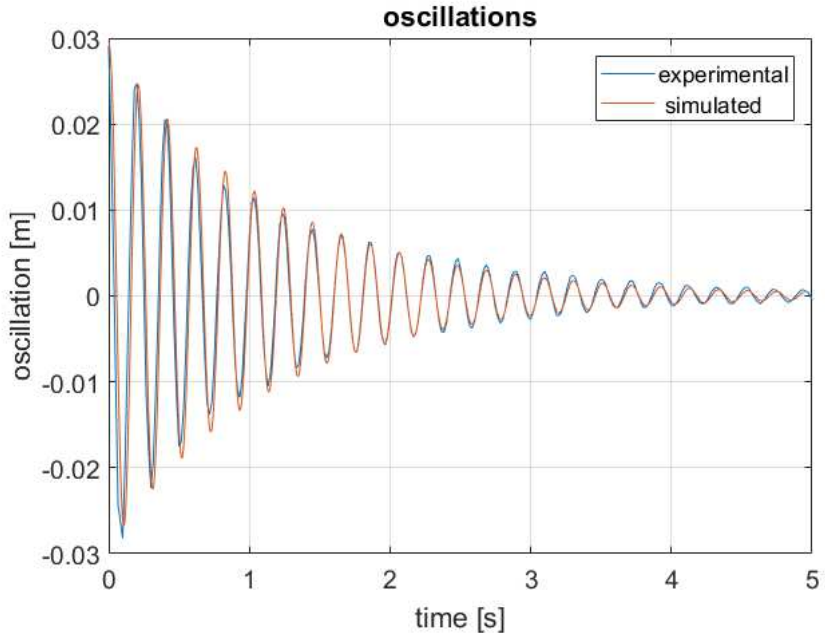

Figure 3.42: Comparison of simulated and experimental behavior.

Therefore, a trade-off has to be made, based on the available actuator. An example of actuator could be a micro linear piezoelectric motor, that is typically very precise and fast.

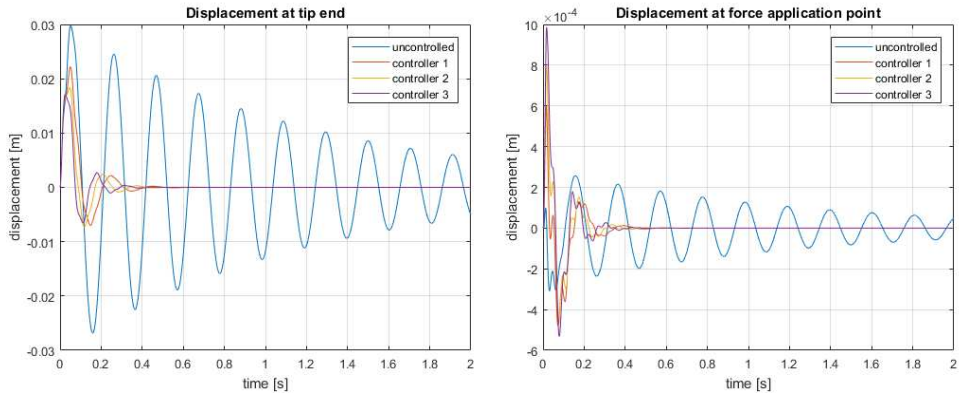

(a) (b)

Figure 3.43: Comparison of tip end displacement (a) and at the control force application point (b) with different K_p coefficients keeping K_d fixed.

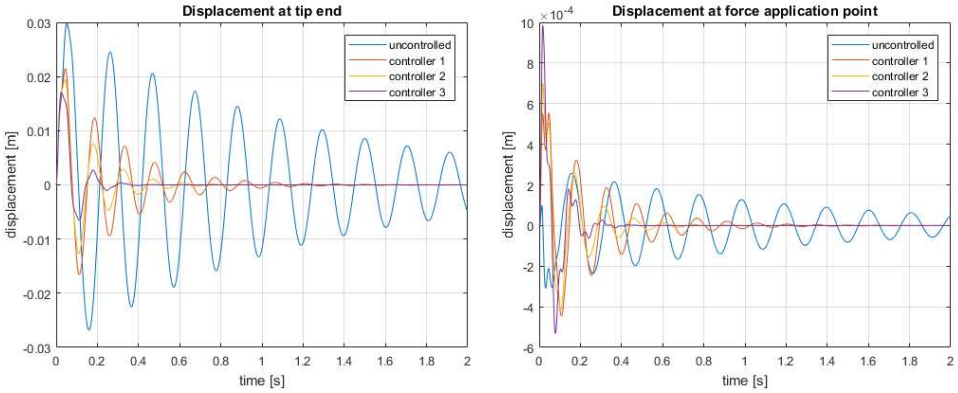

(a) (b)

Figure 3.44: Comparison of tip end displacement (a) and at the control force application point (b) with different K_d coefficients keeping K_p fixed.

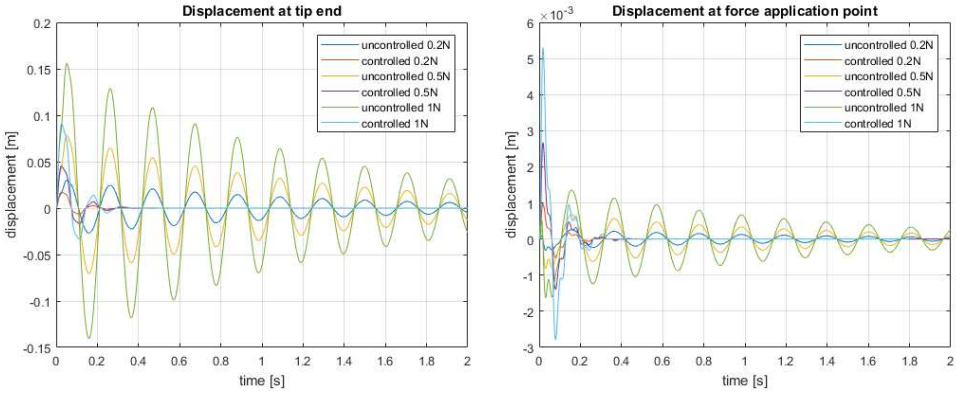

(a) (b)

Figure 3.45: Comparison of tip end displacement (a) and at the control force application point (b) fixed K_p and K_d coefficients and different applied forces at the tip end.

Chapter 4

Experimental tests

This chapter presents the experimental setups and tests performed in the laboratory. The main experimental setup is presented in Section 4.1, with the description of its electronics, mechanical and structural components, and the GOLS, a suspending system with cables and flying beams that allows to carry out tests with the compensation of the influence of the gravity force on the prototype structure. Then, the results of the tests are presented in Section 4.2, divided in tests with uncontrolled and controlled deployment. Their aim is to experimentally study the dynamic behavior of the different configurations. Lastly, a preliminary test where the oscillations of a free boom are compensated with a PID control on the motor is presented in Section 4.3.

4.1 Design of the main experimental setup

The experimental setup is composed by a deployer system and a dummy solar panel. The main components of the deployer include a rotational element (previously shown in Figure 3.26) composed by two spools where the boom is wrapped, that are connected by a shaft to a central cylinder where a dummy Kapton membrane is rolled up. In addition, two small gearwheels are use to transmit the rotation provided by the motor. The dummy solar panel includes two booms, a membrane and a tip end that connects the three elements and keeps in tension the membrane.

In this section, the main components of the experimental setup are presented. They are divided into electronics and structural elements.

4.1.1 Electronics components and sensors

All the electronics and sensors used are all components readily available off-the-shelf.

Arduino UNO microcontroller board

The Arduino Uno R3 board [78] is a 8-bit microcontroller board based on the ATmega328P, with 32 KBytes of In-System Programmable Flash memory where the sketch is stored, 1 KByte of Electrically Erasable Programmable Read-Only Memory (EEPROM) i.e. memory space that programmers can use to store long-term information, and 2 KBytes of Static Random Access Memory (SRAM), where the sketch creates and manipulates variables when it runs.

This board was powered via USB at 5V. This board can transfer data both via classical serial communication and through Inter Integrated Circuit (I^2C) protocol. During the tests, I^2C communication was used between the Arduino Uno and both the Motor Shield, that controls the motor, and the MPU-6050 sensors.

MPU-6050 sensor

InvenSense MPU-6050 sensor [79] contains a MEMS accelerometer and a MEMS gyroscope in a single chip, mounted on a GY-521 breakout board. It is very accurate, as it contains 16-bits analog to digital conversion hardware for each channel. Therefore it captures the x, y, and z channels at the same time. The sensor uses the I^2C-bus to interface with the Arduino via its SDA (A4) and SCL (A5) pins and needs to be powered via the VCC 5V pin and connected to the ground pin. The sketch of the connections can be seen in Figure 4.2. This sensor was chosen because it is very accurate, despite being inexpensive. The data read by the sensor and collected by Arduino is sent via USB port to the Arduino software IDE. An instruction in the IDE program sends the data via serial port to a Matlab® program that reads and analyzes the values. This process is shown in Figure 4.3.

The output of the sensors is a raw value that has to be calibrated in order to correspond to an acceleration value. To do so, measurements were taken with the sensor placed on a flat horizontal surface. The offsets could be calculated for each

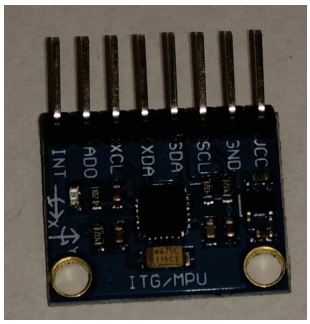

Figure 4.1: MPU-6050, low-cost 3-axes accelerometer and 3-axes gyroscope used in the experimental setup.

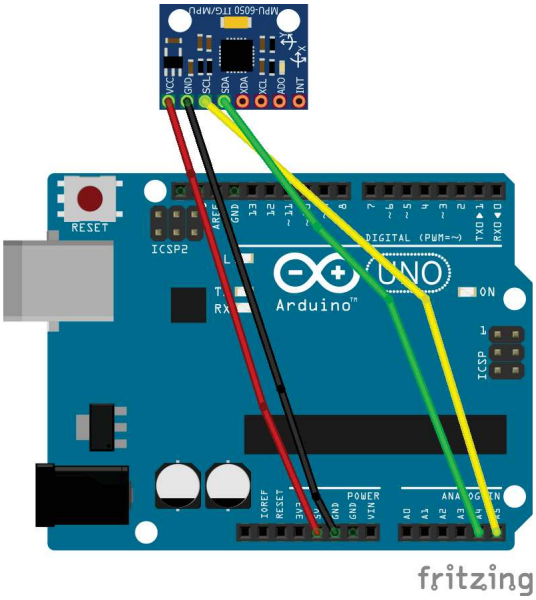

Figure 4.2: Schematic of the circuit with the MPU-6050 and the Arduino board.

of the three axes dividing the raw value by the module of the local gravity vector g.

One of the two sensors was positioned directly attached to the structure of the deployer, while the second one was placed on an external structure mounted on it. The purpose was to measure the difference in accelerations if the external structure was not isolated from the deployer and with a passive damping system between them. Since the mass of each of the two accelerometers is only 1.8 grams and placed on the part of the structure that moves only a very small distance during deployment, with the cables suspended in such a way to avoid any disturbance on the dynamics of the system, their influence in the deployment dynamics was neglected, considering it very small.

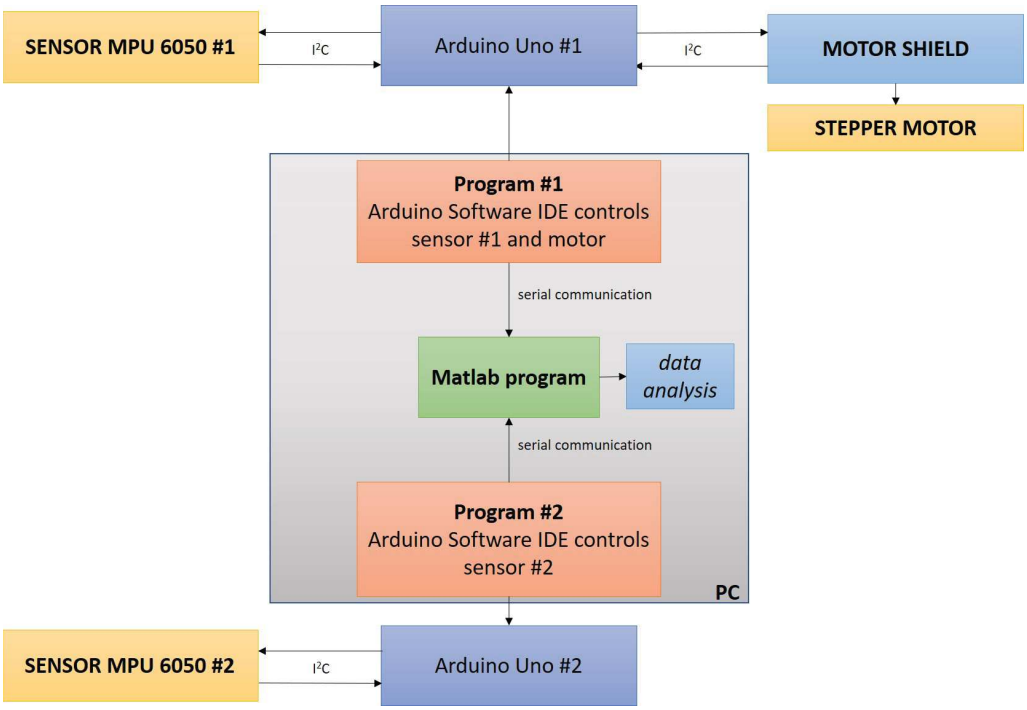

Figure 4.3: Schematics of Arduino IDE and Matlab® environments with sensors and motor.

Motor Shield

The Adafruit Motor Shield [80] is a powerful board that can be stacked on the Arduino board to easily control motors. It has the capability to control up to 2 stepper motors at the same time or 4 DC motors, and one servo motor. It includes 4 H-Bridges: each TB6612 chipset provides 1.2A per bridge, thermal shutdown protection, internal kickback protection diodes. This board can run motors from 4.5 VDC to 13.5 VDC. It can control both unipolar or bipolar stepper motors, in single coil, double coil, interleaved or micro-stepping mode. During the tests, the board was powered with ∼5 VDC from the PC through the Arduino board and was interfaced with the microcontroller via I^2C-bus.

4.1.2 Mechanical and structural components

Motor

The motor used in the experiments is a Faulhaber AM-1524-V12-150 [81], that was already available in the laboratory. The holding torque at nominal current

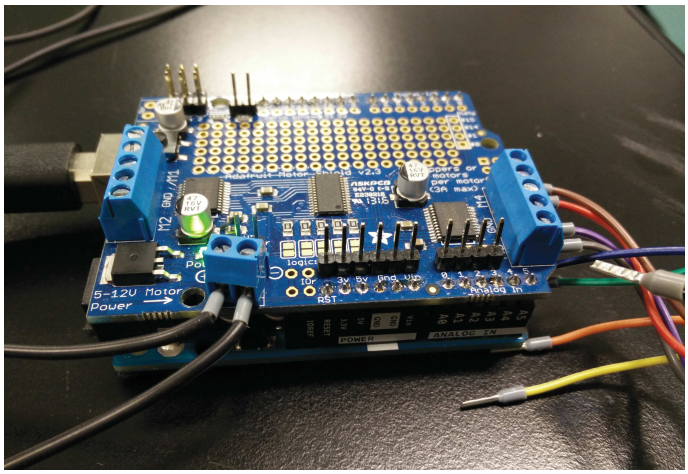

Figure 4.4: Motor shield stacked on the Arduino Uno board.

(0.075 A) of this stepper motor is 6 mNm. Its nominal voltage is 12 V. A gearhead with a reduction ratio of 141:1 is mounted on the motor. The (ideal, without dissipations) torque of the motor becomes then: 6 mNm x 141 = 846 mNm. This torque value is sufficient to deploy both the booms at the same time and to overcome frictions due to the rotation of the gearwheels, and the non-perfect shape of the boom prototypes. The motor was commanded to run at its maximum speed during controlled deployment and retraction tests. In order to measure the effective speed, considering that the deployment time was 420 s for a commanded total number of 40000 steps (experimentally determined value), it results that the velocity of the motor was v_{g2}=95.2 steps/s, that is equal to about 5700 steps/min. This value depends on the provided voltage, which was about 5V during the tests, because the motor was powered from the PC via USB cable through the Arduino Uno board and the Motor Shield.

In order to determine the influence of the motor in the results of the experiments where the motor was used, a preliminary test was done to extract the typical frequencies of vibration of the motor. The FFT of the signal recorded by a MPU-6050 sensor with the motor functioning in single mode, the one used during the tests, is shown in Figure 4.5. Although the microstep mode is the one that influences less the dynamics of the system, the provided torque was experimentally found to be not sufficient to deploy the booms.

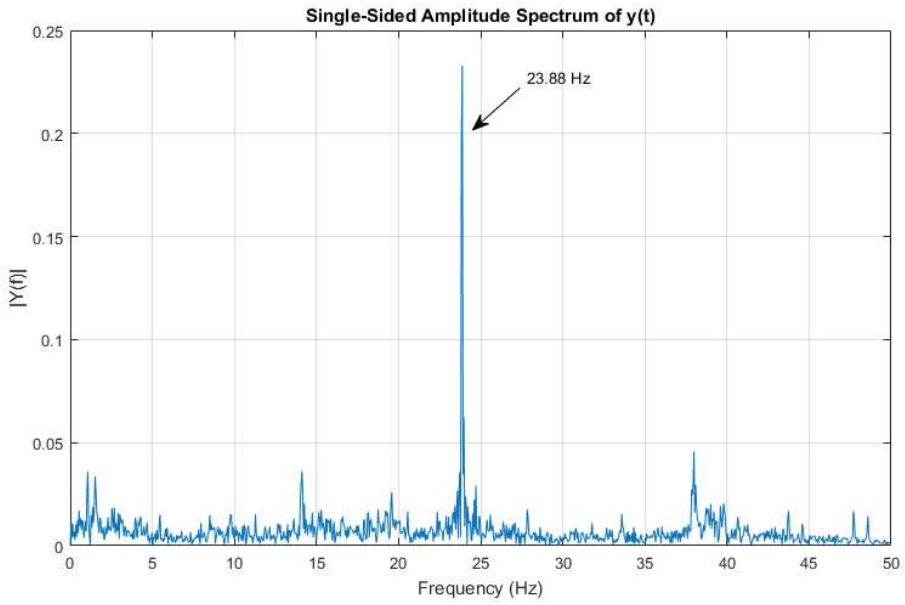

Figure 4.5: FFT of the vibrations of the motor in single mode.

Structure

The deployer structure was made of aluminum, as well as all the rotational elements (shafts). The two spools were made with the 3D printer in PLA. The booms were coiled and fixed on them with two small grub screws. The transmission of the motion from the motor to the boom was possible thanks to two small gearwheels. A sketch of the deployer system and the photo of the system used for the tests (without external structure) are shown respectively in Figure 4.6 and 4.7.

An external structure made of two steel plates connected with four long screws, weighting in total 721 g, was enveloping the deployer during part of the tests with the system appended to the GOLS. Adding mass to the deployer system, this structure represents the interface with a dummy central body of a spacecraft. Accelerations were measured with the MPU-6050 attached on this external element to see how effectively small passive dampers placed between it and the deployer could reduce the transmission of vibrations. The distance between the two plates and the deployer was adjusted blocking the plates in the desired position with nuts on the screws. The lower steel plate that composes the external structure and the 4 screws used to connect it to the upper steel plate is shown in Figure 4.8.

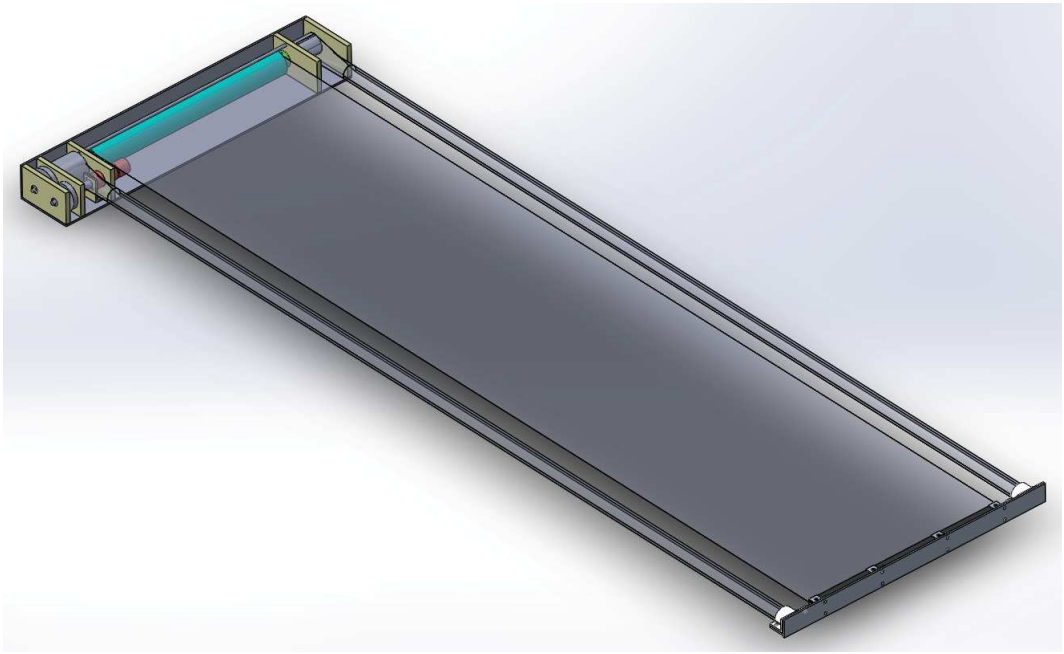

Figure 4.6: Mechanical system.

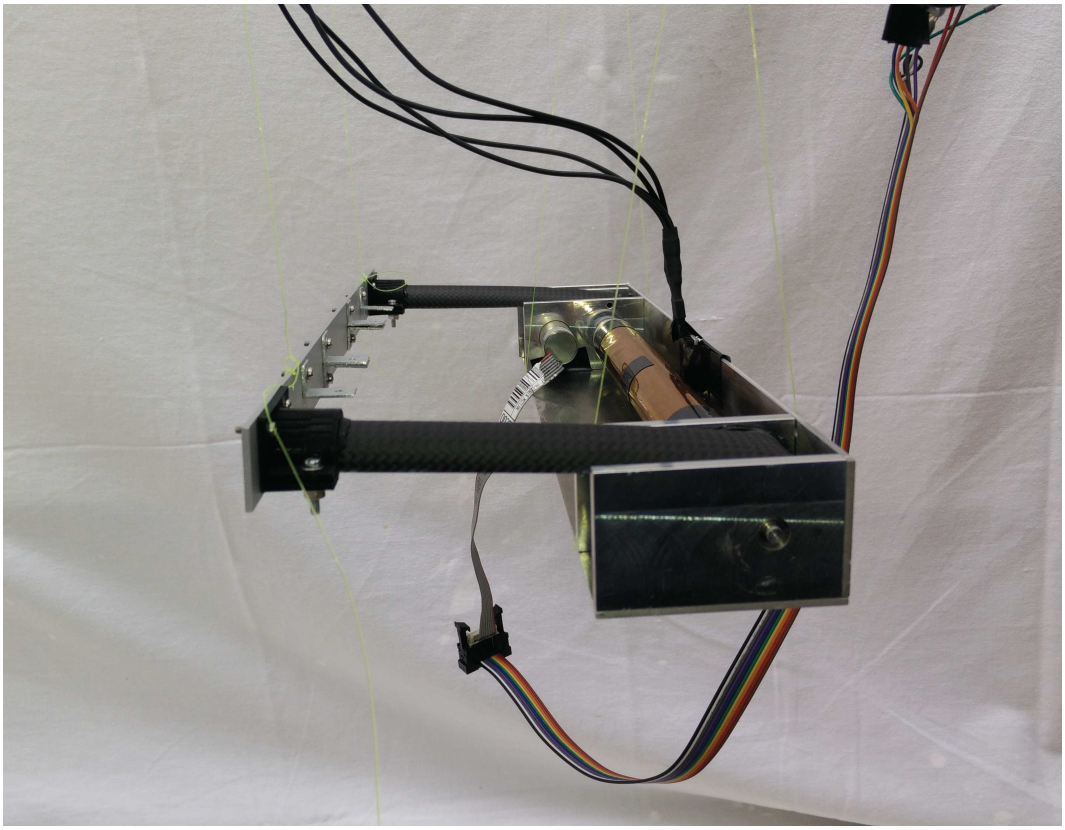

Figure 4.7: Deployer with coiled booms (without external structure).

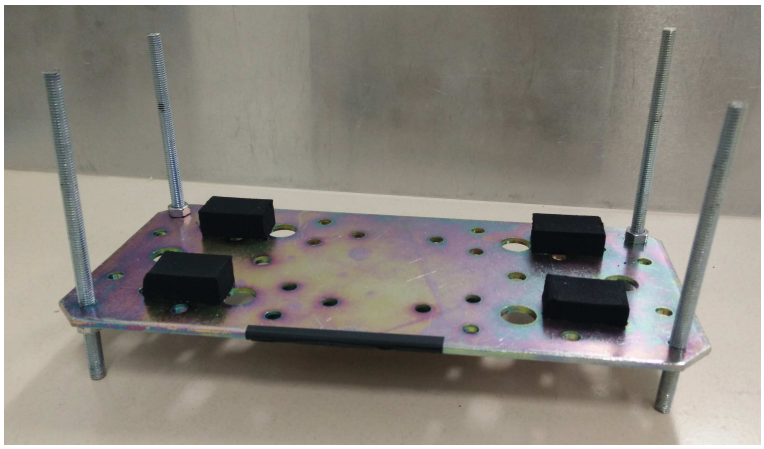

Figure 4.8: Dampers and lower part of the external structure, with connecting screws.

Passive dampers

Some passive dampers made of Ethylene-Propylene Diene Monomer (EPDM) rubber [82] acted as isolators between the deployer and the external structure. They were chosen because they were readily available materials with damping capabilities. This rubber is typically used as sound and electrical insulator, in seals, radiators, tubing, etc. Although this polymer rubber is not typically used as vibration isolator, it showed quite good performances in damping the vibrations transmitted from the deployer to the external structure. The four rubber dampers that were attached to the lower steel plate are shown in Figure 4.8.

4.1.3 Gravity Offloading System

A GOLS was employed to simulate the absence of gravity that can be found in space. This system is based on the Marionette Paradigm theorized by Greshnick and Belvin [83]. In this system, the object is suspended by long cables, where the vertical component of their tensions counteracts the gravity force.

Differently from [63] where the deployer mass was symmetrically distributed in the direction of the spool axis, in this case it was necessary to take into account also the component of the mass distribution in the spool axis direction, since the motor and gearwheels were placed in a non-symmetrical position. Since it was not easy to determine the center of mass of the complex system, a configuration with two

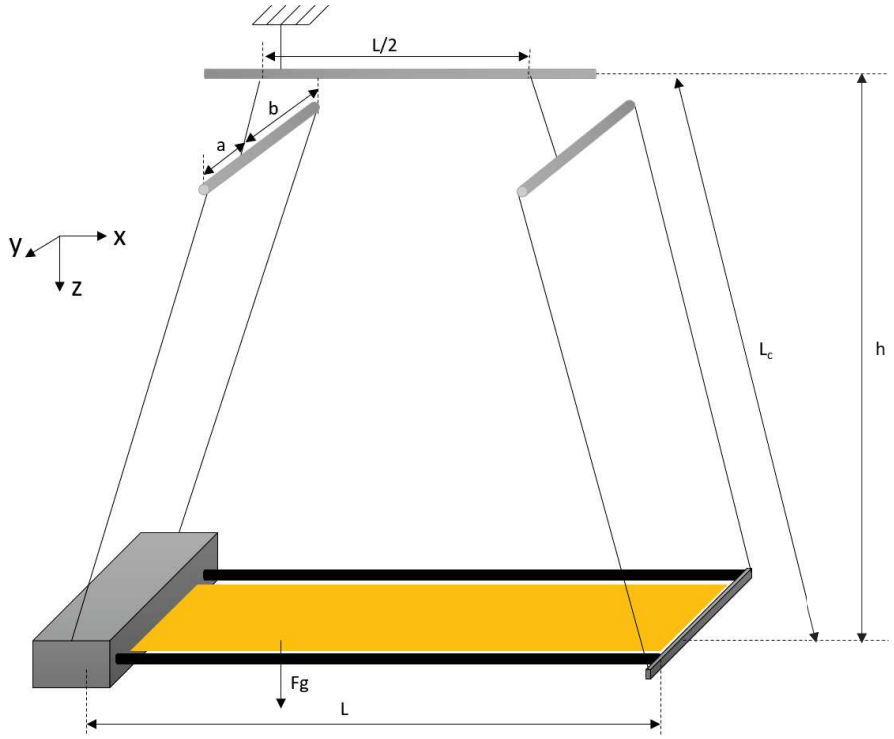

Figure 4.9: Gravity Offloading System.

suspending cables for the deployer side and two for the tip side was preferred. In such a way, it was easier to correct possible misalignments just adjusting the length of a and b along y (see Figure 4.9). The flying beam along x axis was connected to the ceiling with another short cable. Point G is positioned vertically on top of the center of mass of the system during all phases, as can be seen in Figures 4.9 and 4.10. In other words, the center of mass of the system falls always along the vertical line passing through point G.

The system experiences two static equilibrium states: when the booms are fully coiled and at the end of their deployment. This occurs when the vertical component of the tension in the cables equals the weight of the suspended objects.

In this system, the longer the cables, the smaller the angles β_A and β_B. Assuming that β_A is very small compared to β_B because the mass of the deployer m_A= 1222 g (deployer + external structure) is 22.6 times m_B=54 g (including the tip mass and the two booms), the distance along x axis between the points A and B was taken as half the length of the fully deployed booms, L/2, with L_{AB}=94 cm.

Assuming that h is much greater than the length of the booms and that the mass

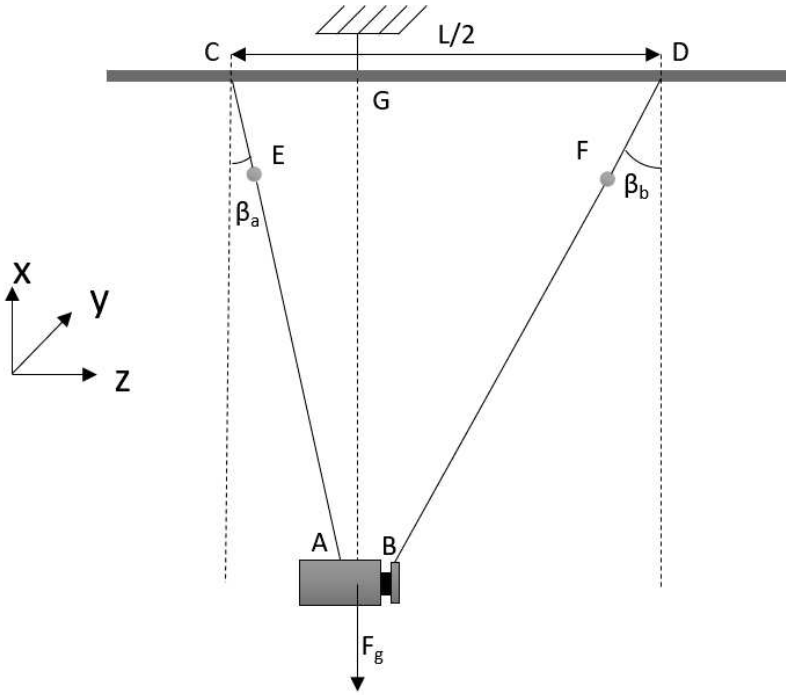

(a)

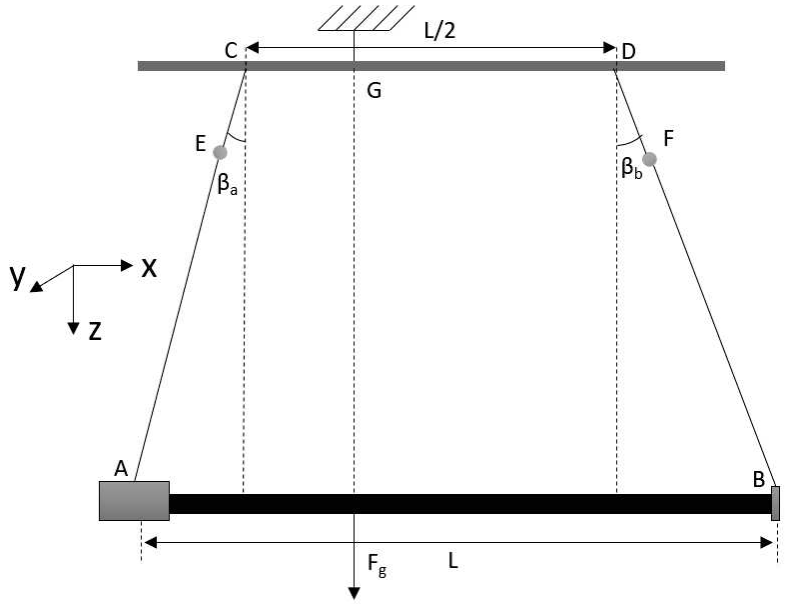

(b)

Figure 4.10: Gravity Offloading System before deployment (a) and after deployment (b).

of the cords was negligible, from the equation of conservation of the momentum it results that the center of gravity of the system will not move during deployment:

$$m_A x_A + m_B x_B = x_G(m_A + m_B) \tag{4.1}$$

where x_A, x_B and x_G are respectively the position along x axis of A, B and G. Assuming $x_G = 0$ and that the length of the fully deployed assembly L^e_{AB} is 0.94 cm, the equilibrium position results:

$$\begin{aligned} x^e_A &= \frac{-m_B L^e_{AB}}{m_A - m_B} \\ x^e_B &= L^e_{AB} + x^e_A \\ y^e_A &= y^e_B = 0 \end{aligned} \tag{4.2}$$

Considering the cords as infinitely stiff springs, the forces of the cords can be calculated as:

$$\begin{aligned} F_{CA} &= \frac{m_A g}{\cos(\beta_A)} \\ F_{DB} &= \frac{m_B g}{\cos(\beta_B)} \end{aligned} \tag{4.3}$$

where

$$\begin{aligned} \beta_A &= \arctan\left(\frac{x_A}{h}\right) \\ \beta_B &= \arctan\left(\frac{L_{AB}/2 - x_A}{h}\right) \end{aligned} \tag{4.4}$$

The elasticity of the 0.4 mm diameter cables used to hang the system to the ceiling was neglected, considering them inextensible. The total length of the cables $L_c \simeq h$ was 4.94 m. Therefore, neglecting the movement of the deployer along x axis x_A:

$$\beta^{simpl}_B \simeq \arctan\left(\frac{L_{AB}/2}{h}\right) = 5.43° \tag{4.5}$$

When the tip of the boom passes under the suspending point D during the deployment, considering that the cables are inextensible, the mass moves downwards in z direction by:

$$l = \tan\left(\frac{\beta_B}{L_{AB}/2}\right) = 0.045\text{m} \tag{4.6}$$

In principle, this length difference could be compensated with very soft extension springs. For this particular case, the necessary spring stiffness was calculated to be k = 0.12 N/m. However, considering that l corresponds only to the 4.78% of the total length of the boom and for simplicity, the springs were not used.

During an uncontrolled deployment, the tip end extends thanks to the stored strain energy in the transition zone of the tape springs. Some factors such as friction, the GOLS, and non uniform viscoelastic relaxation due to long term stowage influenced the deployment reducing the acceleration imparted by the stored strain energy.

The equation that allows the calculation of the deployment force in x-direction during an uncontrolled deployment results:

$$F_B^x = F_{AB}^x - F_{DB}^x \tag{4.7}$$

where F_{AB}^x is the component relative to the tape spring force, and F_{DB}^x is relative to the tension of the cord. In particular,

$$\begin{aligned} F_B^x &= m_B \ddot{x}_B \\ F_{AB}^x &= F_{AB}\cos(\theta_B) \\ F_{DB}^x &= F_{DB}\sin(\beta_B) \end{aligned} \tag{4.8}$$

where

$$\theta_B = \arctan\left(\frac{y_B - y_A}{x_B - x_A}\right) \tag{4.9}$$

The instantaneous length of the booms can be calculated as:

$$L_{AB} = \frac{x_B - x_A}{\cos(\theta_B)} \tag{4.10}$$

Since $m_A \gg m_B$ it is assumed that x_A and β_A are small, as well as θ_B, considering $h \gg L_{AB}/2$.

4.2 Experimental tests

4.2.1 Tests without deployment rate control

A number of tests were carried out to evaluate the effect of an uncontrolled deployment on the deployer and external structure. Before each test, a 0.4 mm diameter cord was circled around the prototype assembly to avoid self-deployment. This cord was cut at each test at t=0 to let the boom self-deploy.

Two opposite cases were observed during the experimental tests:

- the booms did not have enough deployment force to reach the end of the deployment (test 1);
- the structure would deploy completely with a shock load at the end of the deployment (test 2).

The difference between the two cases was noticed to be linked to the time that passed between the full coiling operation and the release: the shortest the time, the highest the deployment force that was available to extend the booms. This demonstrates how the boom prototypes that have been used for about 10 months before these tests have lost part of their self-deployment capability.

Test 1

Analyzing a video that was taken during one of the tests where the booms did not fully deploy, it was possible to extract the coordinates for the deployer A and the tip mass B, and compute the deployment force that was experienced using Equations 4.8. Figure 4.11 shows the coordinates of A and B. It can be seen that the initial length of the boom was 13.4 cm, the final one was 88.4 cm. Therefore, 5.6 cm of booms were still wrapped on the spool at the end of the deployment. Figure 4.12 shows the force behavior with the variation of boom length: F_{AB} is the deployment force from the tape spring to the tip mass, F^x_{DB} is the component along x-axis given by the GOLS, and F_B corresponds to the total force acting on the tip mass including viscoelastic and frictional effects.

Compared to the theoretical calculations, these values result one order of magnitude smaller, as expected considering that the theoretical model does not take

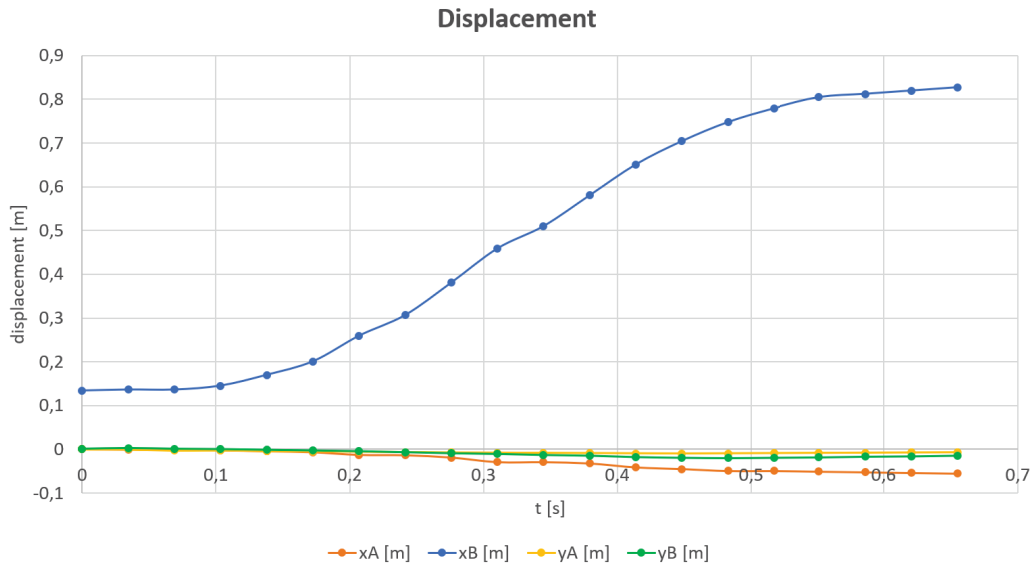

Figure 4.11: Coordinates of points A (deployer) and B (tip end) during deployment extracted from the video.

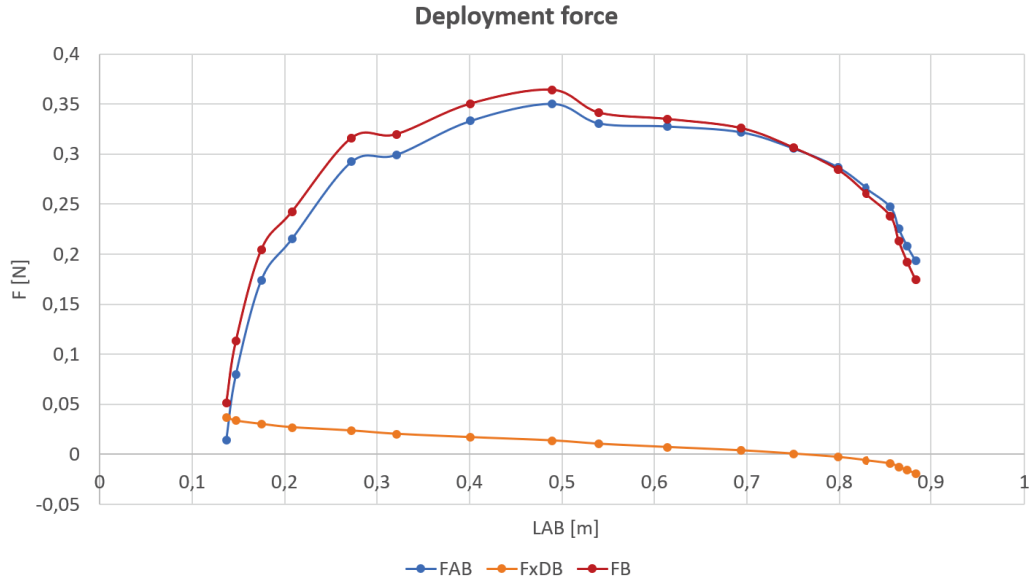

Figure 4.12: Deployment sequence in non-controlled conditions. The booms do not fully deploy, and the membrane is not in tension.

into account all the dissipations. These values are also compatible with the results obtained in [63]. The accelerations read by the accelerometers are shown in Figure 4.13, with z in the direction of the gravity force, x along the length of the deployable structure and y in the transversal direction. As expected, the largest accelerations

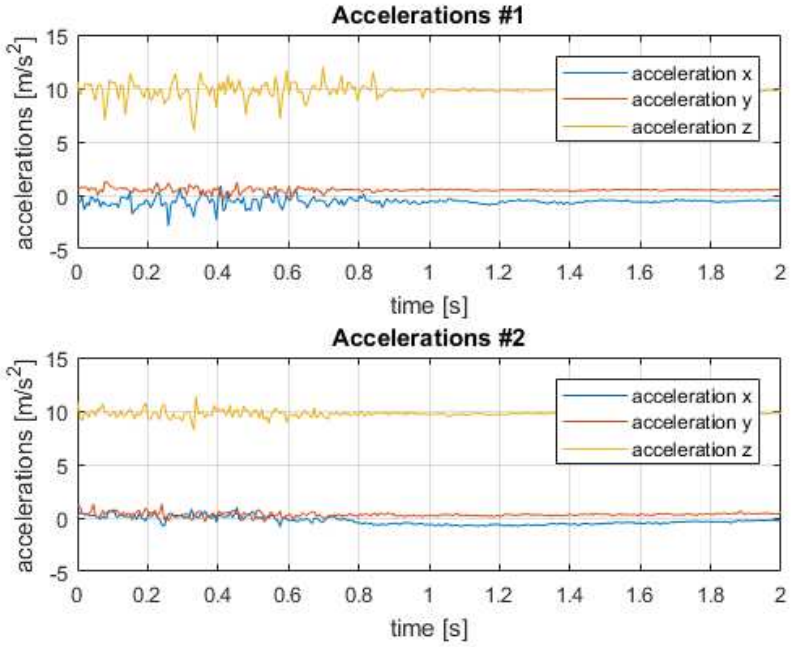

Figure 4.13: Accelerations read by the two accelerometers.

are found along the z and x directions. Comparing the two charts in Figure 4.13, the accelerations measured in the first second (corresponding to the deployment time) by the accelerometer attached to the external structure are reduced with respect to the accelerations that are experienced by the deployer. Computing the FFT of the signal, the resulting curves are shown in Figure 4.14. Although the deployment did not produce any shock load, the signal was very noisy as expected.

According to Figure 4.14, the intensity of the signal seen by the accelerometer on the external structure is attenuated by about half for the most of the frequencies with the use of the passive dampers. These two charts will be compared with the results in Test 2 and the controlled case.

Test 2

Following tests showed the typical behavior of bistable structures: the shock load at the end of the deployment. As previously mentioned, in the tests that were carried out for this thesis, the shock loads were noticed to occur only when the deployable structure was released shortly after rolling it up. In the other cases, the shock did not occur as shown in Test 1 because of internal viscoelastic relaxation and frictional

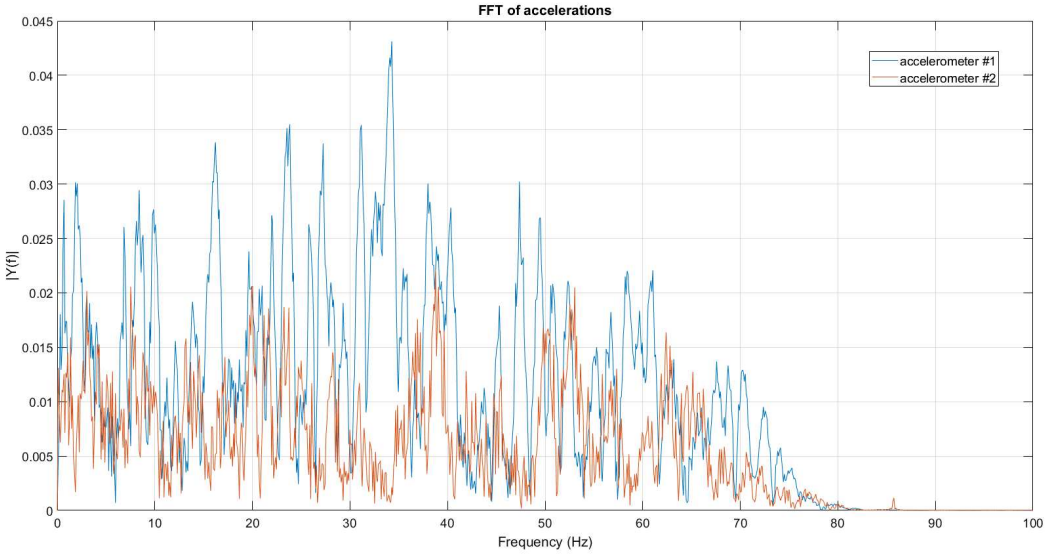

Figure 4.14: FFT of the signal read by the two accelerometers with no final shock.

forces that prevented full deployment. The tests were carried out about 10 months after manufacturing the boom prototypes. It is expected that this situation does not occur when using newly manufactured booms.

As during test 1, cables were used to retain the system before deployment and were cut at t=0 to release the deployable portion of the structure. At the end of a full deployment with shock load, the situation showed in Figure 4.15 occurred: the spool oscillates around the equilibrium angle at the end of the deployment, making the boom axially oscillate, generating relevant disturbances in the deployer

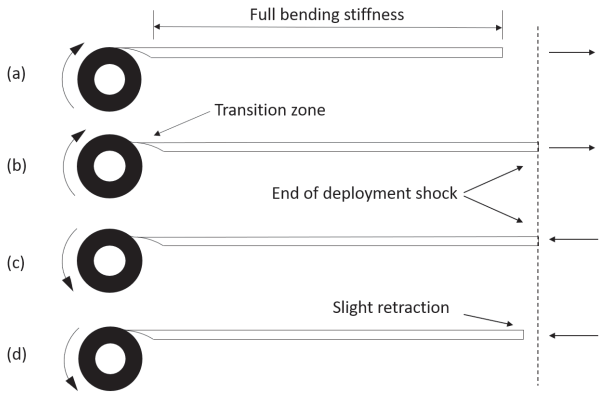

Figure 4.15: Rotating spool at the end of the deployment. Modified from [63] to reflect the current configuration.

and external structure. From the top, (a) shows the moment just before the end of the full deployment, and the fact that the deployed portion of the boom has full bending stiffness (this applies in all cases), while the transition zone pointed in (b), on the other hand, is less stiff, and bends more easily. When the boom reaches full deployment, the shock load makes the boom revert its axial movement (c) and slightly retract as shown in (d), making the spool counter-rotate and oscillate around an equilibrium angle until the oscillations are damped.

Figures 4.16 and 4.17 show respectively the components of the acceleration as they were read by the two accelerometers and the combination of the three components of the acceleration recorded by the two sensors (MPU-6050) in the same plot. It is clear from the curves that the shock load occurs t=0.8 s after cutting the retaining cable, and that oscillations are induced after the deployment to the rest of the structure. The oscillations recorded in blue are completely damped in about 1 second. The red curve shows that the shock load is not transmitted to the external structure, however the low frequency vibrations due to the counter-rotation of the spool make the whole structure oscillate.

Figure 4.18 shows the FFT of the combination of the three components of the accelerations. The highest peak in blue at f = 6.64 Hz is compatible with the oscillations of the system at the end of the deployment that are shown in Figure 4.17. However, the signal is very noisy, making it difficult to individuate specific vibration modes as expected (except for the one of the oscillation after the shock load), similarly to the previous case examined in Test 1.

4.2.2 Tests with deployment rate control

Deployments and retractions with a motor to drive the spool and extend/retract the booms were performed to compare their dynamical behavior with the results of the uncontrolled tests. As it was mentioned in 4.1.2, the motor was driven at the maximum possible rotational speed, that was based both on the load and on the power in input. From experimental calculations, the speed was 95.2 steps/s, for a total deployment and retraction time of 420 seconds, that corresponds to 40000 steps of the motor. Very similar results were obtained in the deployment and in the

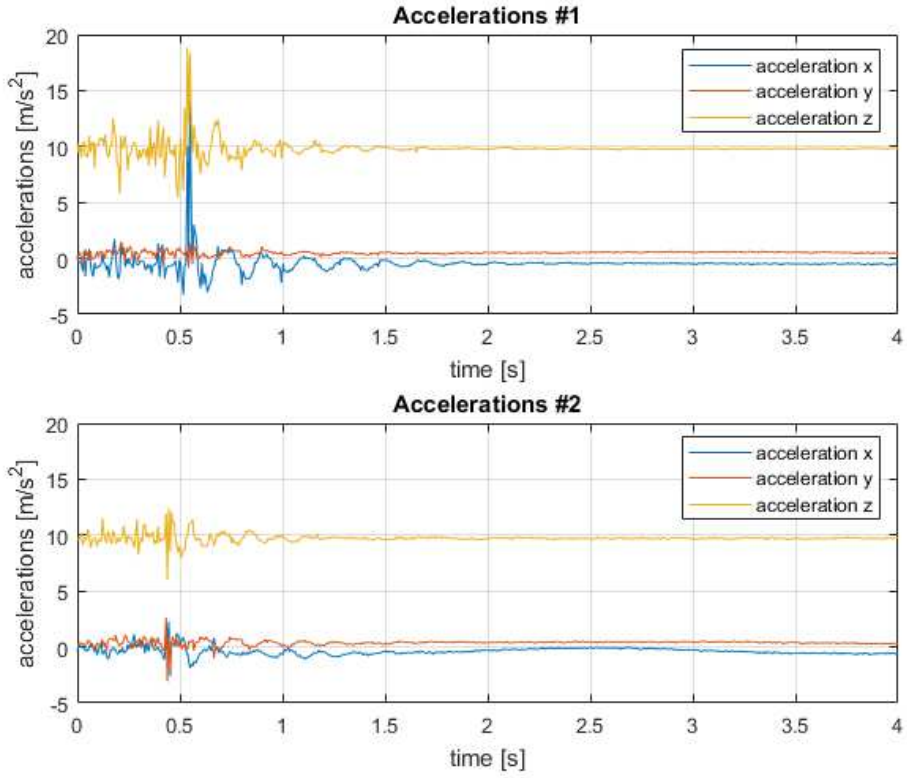

Figure 4.16: Results of the measurements: modulus of the accelerations for the two sensors along the x-y-z axes.

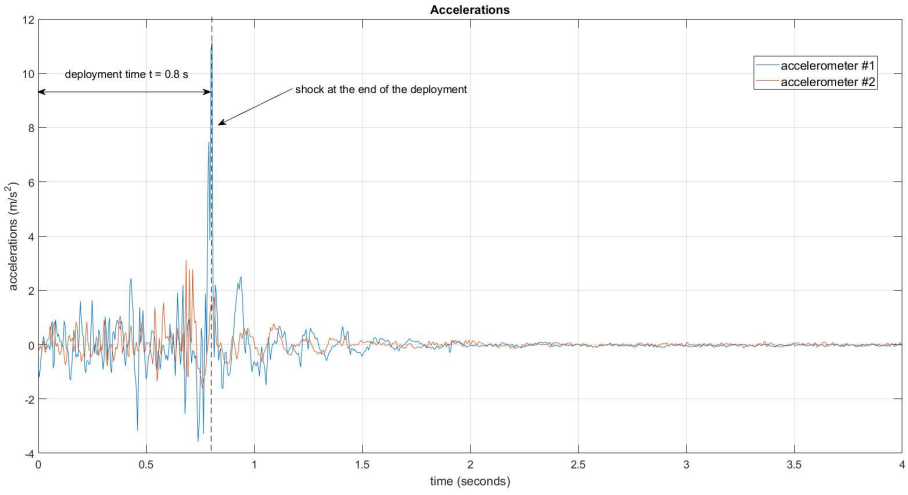

Figure 4.17: Results of the measurements: modulus of the accelerations for the two sensors combined and referenced to zero.

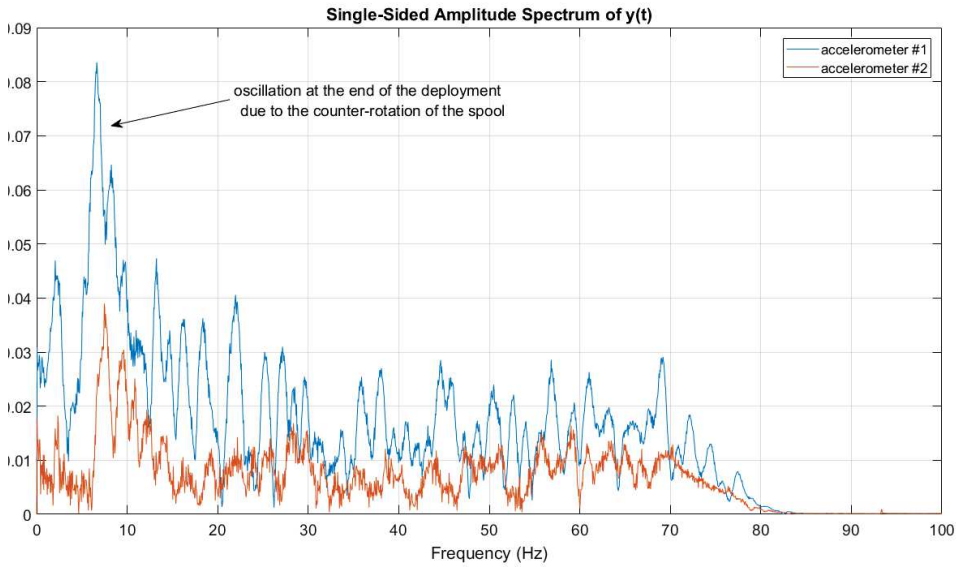

Figure 4.18: FFT of the measurements of a non controlled deployment.

retraction tests, so only one case in presented here.

Figure 4.19 shows the system during a controlled deployment.

Also in this case, the oscillations were focused on the x (horizontal) and z (vertical) axes. During the deployment/retraction phases, small oscillations were seen to originate from 'non-smooth' deployment of the boom because of micro-cracks that formed on the borders of the booms after months of use, or friction on the external parts of the spool that were used to provide a straight deployment and retraction even if the booms had some small manufacturing inaccuracies. The main source of vibration was due to the motor rotation and the mechanical transmissions (espe-

Figure 4.19: Photo taken during deployment.

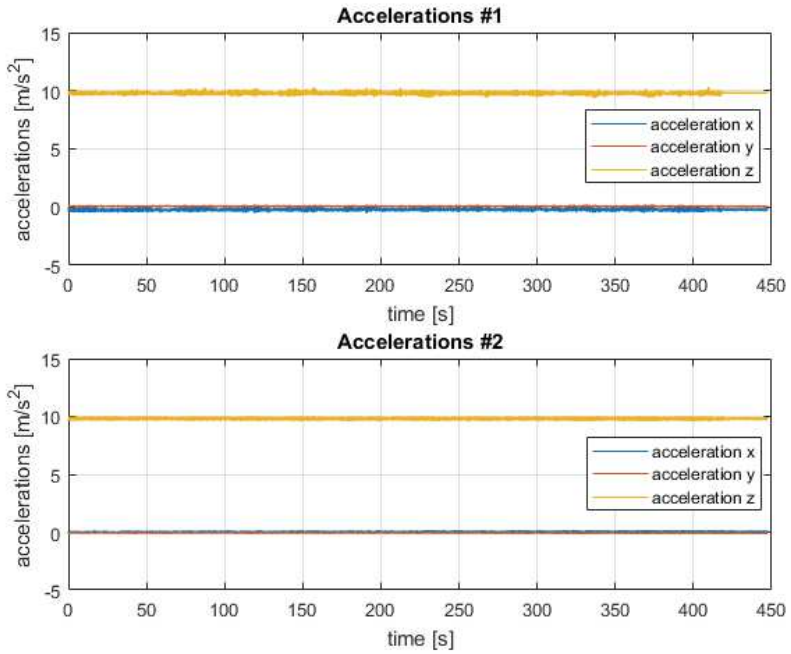

Figure 4.20: Results of the measurements, accelerations in the three axes for the two sensors during controlled deployment.

cially the gearwheels). Analyzing the resulting chart in Figures 4.20 and 4.21, it is possible to see a quite smooth signal, with accelerations that are not larger than 1 m/s^2 except for one peak at t = 343.5 s that is due to the reasons previously mentioned.

Also in this case, the FFT of the accelerations was computed in order to see which frequencies of vibrations were excited during controlled deployment/retraction. The FFT is shown in Figure 4.22. One dominant peak can be seen in the results. Comparing Figure 4.22 to Figure 4.5, it is clear that the peak frequency is the natural frequency of the motor. The passive damper works well in reducing the transmission of vibrations to the external structure, cutting off almost completely the vibrations due to the motor.

4.2.3 Discussion

After singularly examining the results of two uncontrolled and one controlled deployment, some conclusions are reported.

In general, uncontrolled deployments are considered unreliable because of their

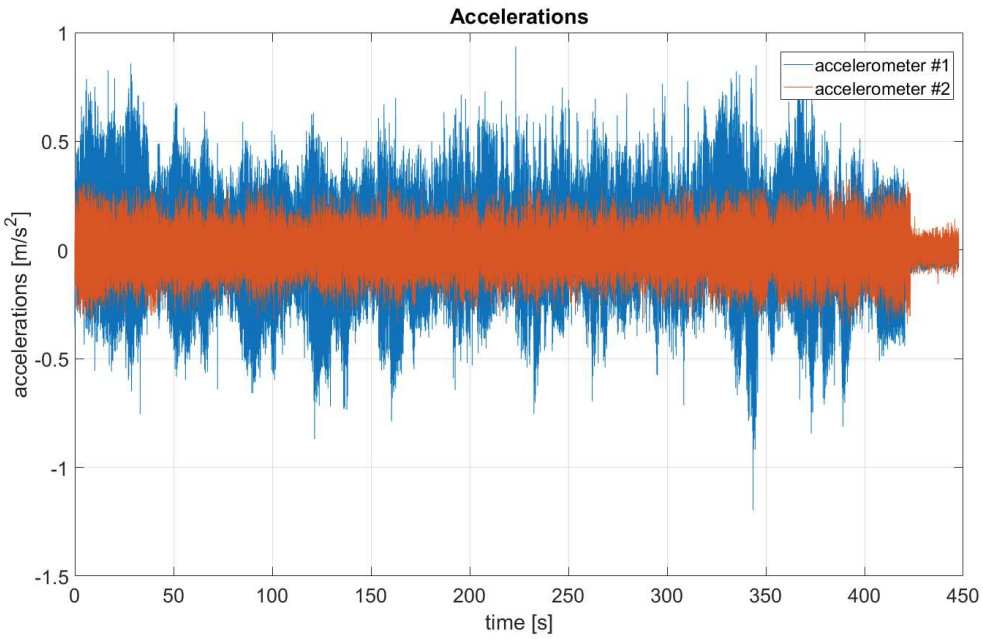

Figure 4.21: Results of the measurements, modulus of the accelerations for the two sensors during controlled deployment.

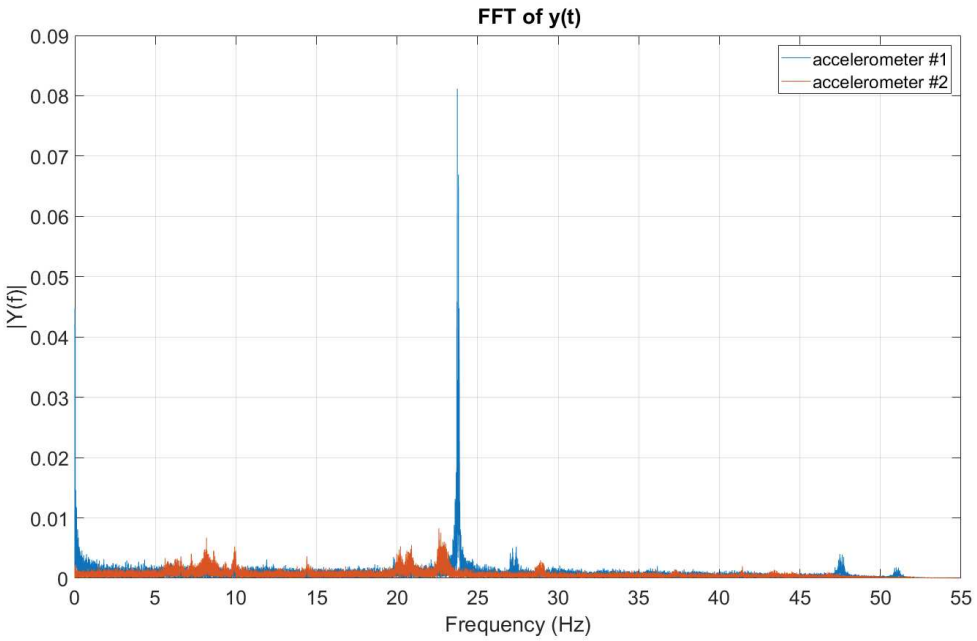

Figure 4.22: FFT of the measurements.

lack of repeatability. The first reason refers to the fact that the tape springs did not fully extend during some of the deployments. This situation can lead to mission failures, in the case that an appendage such as solar panels do not completely deploy, for example because it might not be able to provide the necessary power to the satellite. A shock load, typical of this type of structures, was seen to happen only during deployments initiated immediately after the tape springs had been rolled up. This was explained because the booms were manufactured about 10 months before the tests, and viscoelastic relaxations were becoming influent in the behavior of the system. This repeatability issue due to energy relaxation over long stowage confirms the findings of [57]. Even though research has been done to reduce the viscoelastic energy losses over time [54, 58], the studied models are difficult to implement and computationally expensive when the entire system is studied. Moreover, taking into account the results of the simulations reported in Section 3.5, uncontrolled deployments that cause final shock loads are considered not suitable for small-sized satellites, because they destabilize the attitude of the spacecraft. In addition to this, the vibrations that are experienced during uncontrolled deployments are very "noisy". The fact that they are spread in a broad range of frequencies makes them very difficult to control.

Conversely, a controlled deployment is needed when deploying structures of this type from small satellites, although this only possible with the overall increase of mass of the system due to the controller and the motor. In this case, as can be seen from Figure 4.23 that shows the different components of the accelerations as well as from Figures 4.24 (sensor on the deployer) and 4.25 (sensor on the external structure) where a comparison between the FFTs resulting from the two extreme cases is reported, the accelerations that are experienced in the controlled case are lower in magnitude, and more controllable since there is only one definite frequency peak relative to the motor. The transmission of these oscillations was efficiently reduced using simple passive rubber elements.

In addition to these advantages, even though the motor was supplied with V = 0.4 V_{nom}, it was able to deploy and retract efficiently and smoothly the whole structure with low power consumption. In particular, the maximum power that it

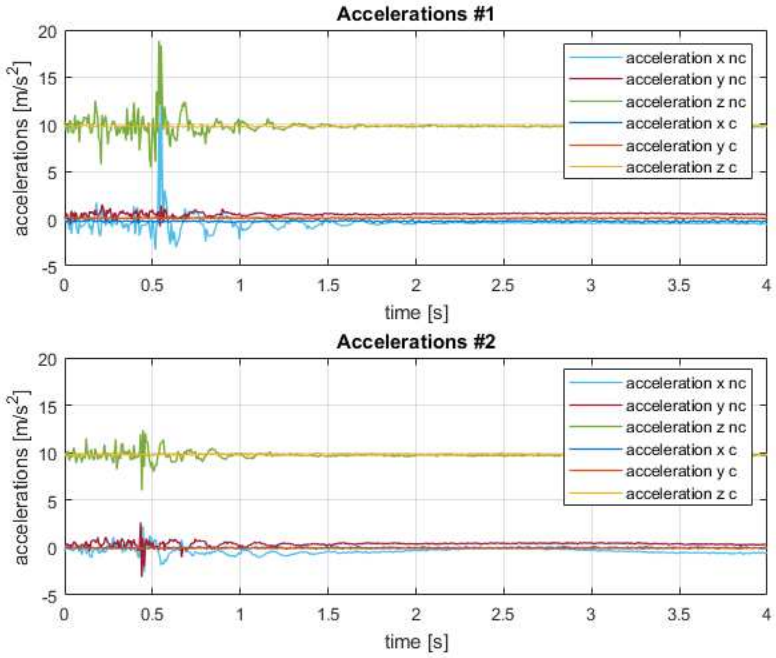

Figure 4.23: Comparison between the accelerations from t=0 to t=2 s in the case with shock load and controlled deployment (nc denotes the uncontrolled results, c the controlled ones).

could draw from the power supply was roughly 5V x 0.45 mA = 2.25 W, which is a small value compared to the power that can be produced by a satellite of the studied size (about 50-100 W).

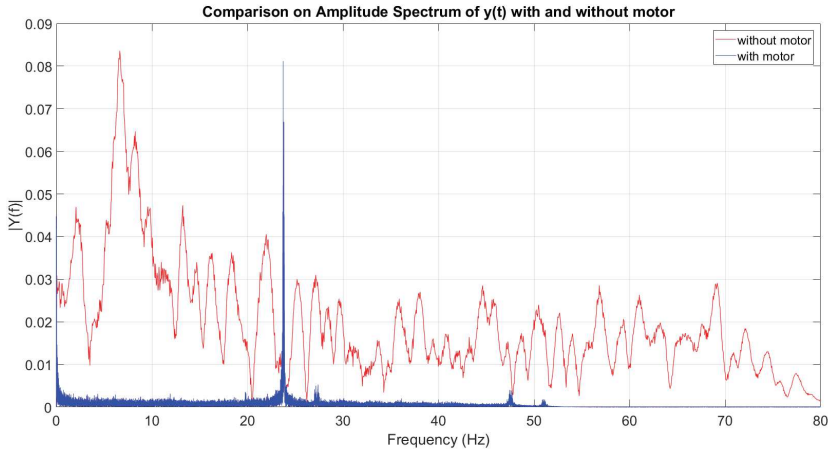

Figure 4.24: Comparison between the values of the FFT in the two cases with and without motor for accelerometer 1.

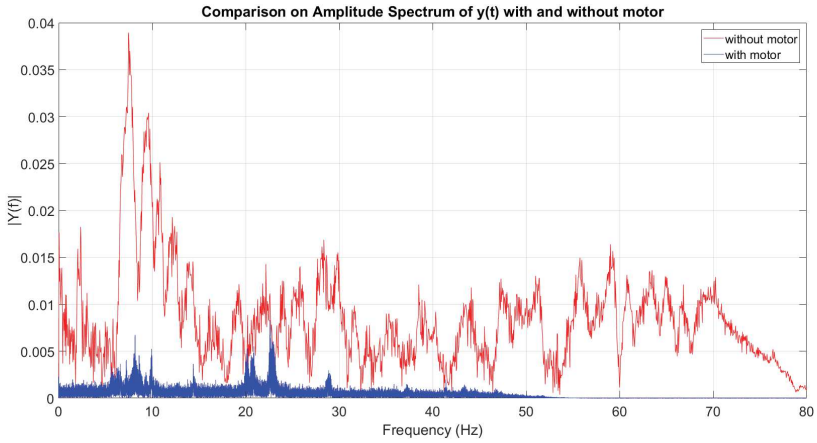

Figure 4.25: Comparison between the values of the FFT in the two cases with and without motor for accelerometer 2.

4.3 Controlling the system with the motor

Rolling up and deploying the boom without the use of any physical constraints to control its direction made it possible to notice that the boom tip followed a specific trajectory and showed a specific behavior during the two phases when deployed in vertical, i.e. near its equilibrium position. In particular, this is possible thanks to the elasticity of the boom in the transition area between the deployed and the rolled-up portion of the boom. Being this area of the boom very complicated to model, this control system was only tested with some preliminary experiments.

The idea at the base of this experiment is shown in Figure 4.26. When the motor rotates as in the sketches at the center and right-hand-side to respectively deploy and retract the boom, the boom oscillates around its initial angular position simply rolling up or deploying, with a tendency to follow the rotation of the hub, rotating in the same direction. This is due to the elasticity of the transition portion of the boom that is in contact with the coiled portion. This effect can be seen in Figure 4.27, where two set of measurements are reported as an example, to show the variation of angle y when the motor is commanded with a loop of ± 20 steps (in blue) and ± 50 steps (in red). As can be seen, the boom oscillates around an equilibrium position at $-11.8°$, with an oscillation that depends on the commanded number of steps and the length of the booms.

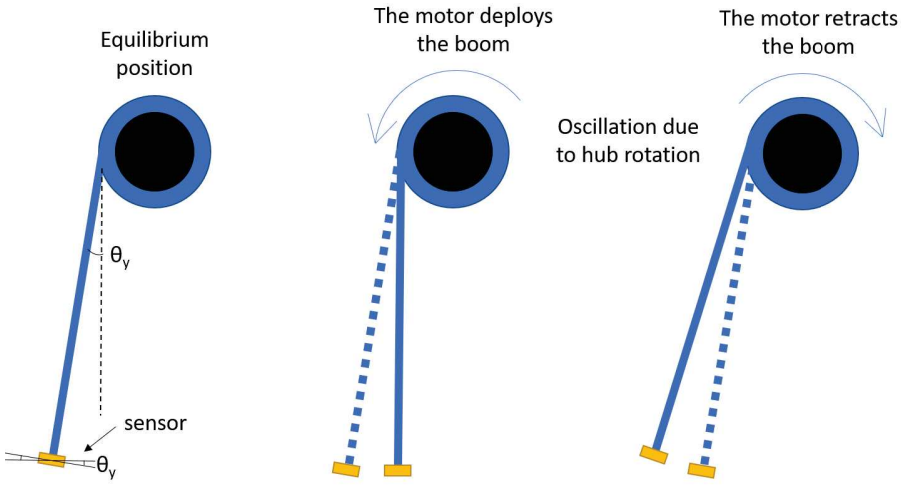

Figure 4.26: Idea at the base of this experiment.

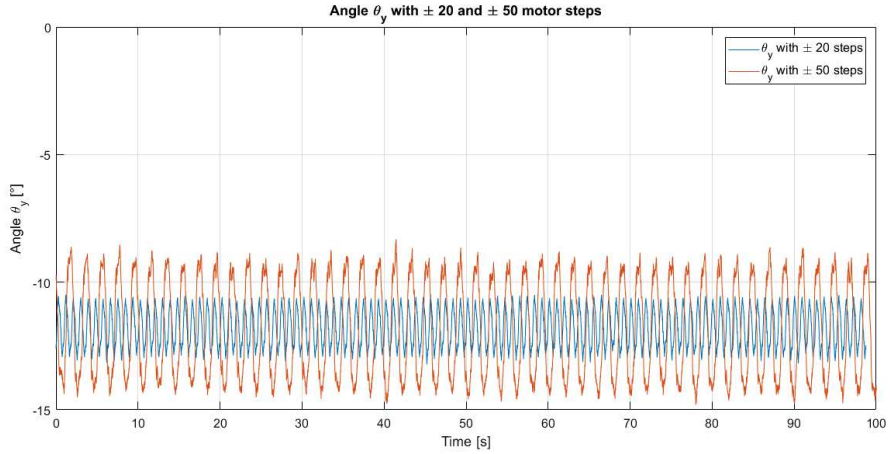

Figure 4.27: Example of oscillations of the boom around y axis with ±20 and ±50 commanded steps.

4.3.1 Experimental setup and measurement process

The experiment was set up as follows: the deployer was placed on the table, so that the boom could freely deploy downwards (see Figure 4.28). In this vertical configuration, the boom was free to oscillate around the angular position at rest. Equilibrium positions in terms of angle θ_y were measured for different boom lengths with the boom at rest, and are shown in Figure 4.29.

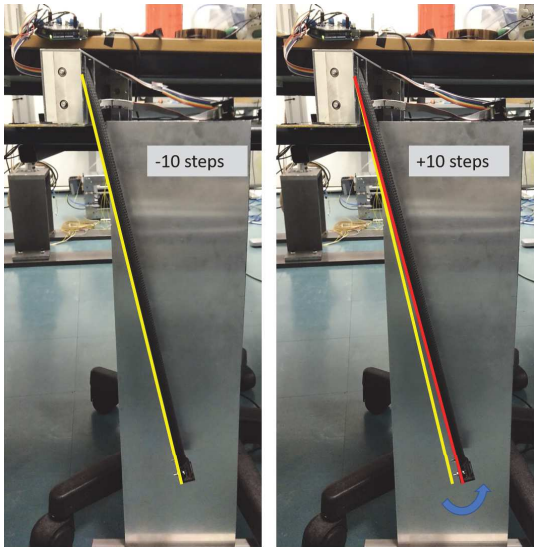

Figure 4.28: Oscillations with the motor running to -10 steps (left) and to +10 steps (right).

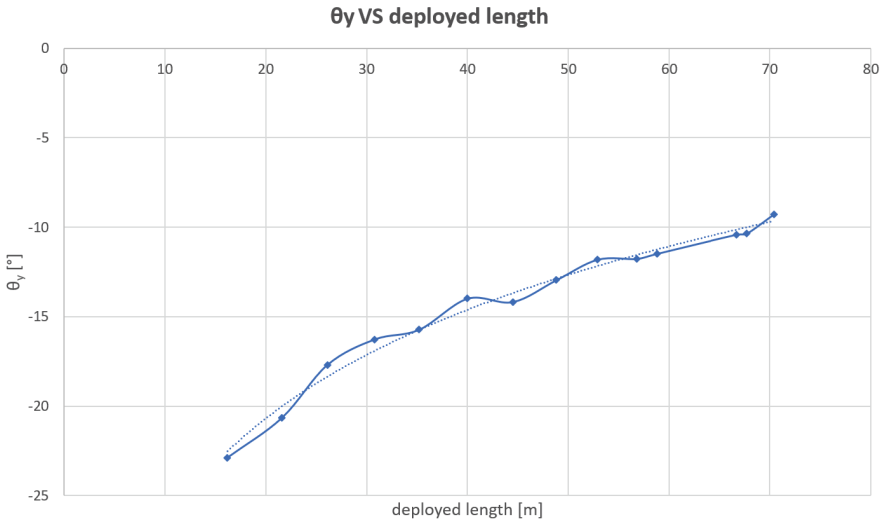

Figure 4.29: Angle θ_y VS deployed length.

The test was made with the boom deployed length set to 55 cm. A single MPU-6050 was placed at the boom tip to measure the oscillations of the boom. In this case, $m_{tip} = 0.01$ kg (including a supporting structure for the sensor). Both the motor and the sensor were connected to the same electronics board. Also in this case, a single Arduino Uno with an Adafruit Motor Shield V2.3 was used both to control the motor and to power and receive the signals from the sensor. Using a single Arduino made it possible to use a single code for controlling the motor (in this test, the same motor as the one used in the experiments presented in section 4.3 was used) and receiving the signals from the MPU-6050. After loading the code on the Arduino Uno, the data received from the sensor was directly processed in the microcontroller. After processing the data from the accelerometer and the gyroscope to obtain the angle θ_y (the input for the PID controller), the Arduino computed the output of the PID control in terms of step number that had to be performed by the motor. Then, the data received from the sensor was given as input to a Matlab® code to generate the final plots. The process scheme is schematized in Figure 4.30.

The controlled variable was the angle θ_y read by the sensor, obtained after the application of a *complementary filter* on the gyroscope and the accelerometer measurements and directly computed in the Arduino board. A filter is needed when computing an angle measurement using an accelerometer and a gyroscope. The

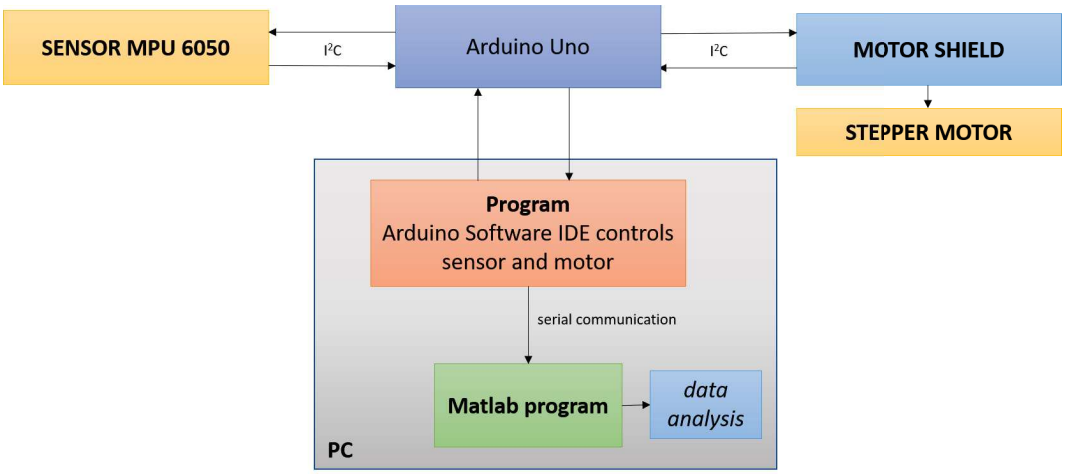

Figure 4.30: Experiment workflow.

complementary filter was chosen over a more complicated Kalman filter because it can be easily handled by a 8-bit microcontroller. In particular, from the gyroscope measurements it is possible to obtain the angular position with an integration of the angular velocity over time. However, because of the integration over time, the measurement tends to drift, not returning to zero when the system returns to its original position. Therefore, the gyroscope data is reliable only on the short term, and its data need to be filtered with a high-pass filter that filters the drift. On the other hand, it is always possible to determine the orientation with respect to the gravity vector with the accelerometer, with a simple atan2 function. However, every force acting on the system will disturb the measurements, making them very noisy. Therefore, accelerometer data is reliable only on the long term, so a low-pass filter needs to be used. The first order complementary filter uses a coefficient α that has to be tuned based on the system in use, to establish the weight of the angle computed with the integration of the gyroscope measurements and the angle computed from the accelerometer data.

Summarizing, on the short term, data from the gyroscope was used, because it is precise and not susceptible to external forces. On the long term, data from the accelerometer was used, as it does not drift. The equation that allows to calculate the angle is then:

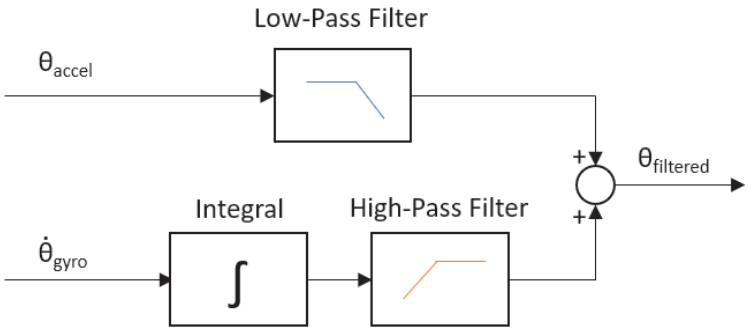

Figure 4.31: Complementary filter.

$$\theta = \alpha \cdot (\theta + data_{gyro} \cdot dt) + (1 - \alpha) \cdot data_{acc} \tag{4.11}$$

The gyroscope data is integrated every timestep with the current angle value. Then, it is combined with the low-pass data from the accelerometer. The process is shown in Figure 4.31.

The measurements were taken forcing the boom to oscillate around the rest position θ_{y0} that corresponded to that specific boom length. In the initial configuration the boom was forced to assume a perfectly vertical position, at $\theta_{yi} = 0°$. Releasing the boom, the stored energy available in the transition area would make it start to oscillate.

The coefficients of the PID controller were calculated using the Ziegler-Nichols' closed loop method. This method consists of the following steps:

- Increase K_p until there are sustained oscillations in the signals in the control system, e.g. in the process measurement, after an excitation of the system. (The sustained oscillations corresponds to the system being on the stability limit.) This K_p value is denoted the ultimate (or critical) gain, K_{pu}. K_{pu} must be the smallest K_p value that drives the control loop into sustained oscillations.

- Measure the ultimate (or critical) period Pu of the sustained oscillations.

- Calculate the controller parameter values according to Table 4.1, and use these parameter values in the controller.

K_p	T_i	T_d
$0.6 \cdot K_{pu}$	$\frac{Pu}{2}$	$\frac{Pu}{8}$

Table 4.1: Formulas for the PID controller parameters in the Ziegler-Nichols' closed loop method

With this method, sustained oscillations resulted with $K_{pu} = 20$, and the oscillation period was $Pu = 0.526$ s. Therefore, the tuned parameters for the system resulted:

- $K_p = 12$
- $T_i = \frac{K_i}{K_p} = 0.263$
- $T_d = \frac{K_d}{K_p} = 0.066$

4.3.2 Measurement results and discussion

First of all, some measurements were taken without an active controller. Repeating the tests, the behavior was very similar as expected, and can be seen in Figure 4.32, where five overlapping curves from different measurements are reported. The energy dissipation associated to these curves is linked to the gravity force that tends to return the system to its resting position and to the internal damping that is experienced in the transition portion of the boom. In practice, it is not possible to establish the amount of damping due to each component.

In addition to these two components, the experiments that included a control system added the component due to the motor. From a practical point of view, in order to compensate the errors:

- when $\theta_y > \theta_{y0}$, the motor rolled up the boom,
- when $\theta_y < \theta_{y0}$, the motor deployed the boom

with a certain number of steps that were commanded by the controller. A small error tolerance of $\pm 0.25°$ was given to the controller around the equilibrium position.

The K_p and K_i coefficients calculated with the Ziegler-Nichols' method were used in all the tests. Slightly different values were given to the K_d coefficient, in the

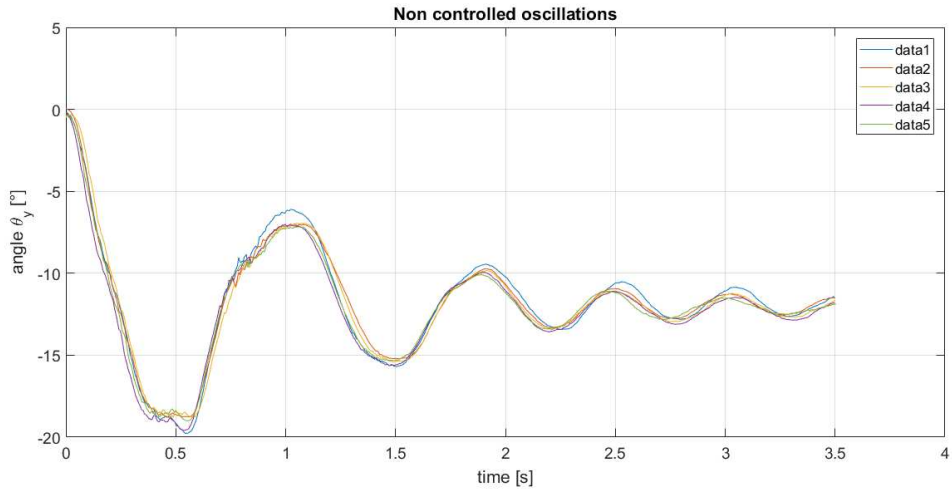

Figure 4.32: Measurements results in the non controlled case.

proximity of the one found with the Ziegler-Nichols' method. The most significant results are shown in Figure 4.33, where two overlapping resultant curves for two different controlled cases (denoted respectively with c1.1+c1.2 and c2.1+c2.2) are compared to the non controlled one (nc1 and nc2). In the first case (curves c1.1 and c1.2), the motor starts to control the oscillation after the first peak, while the second case (curves c2.1 and c2.2) it controls the oscillations more efficiently. In this case, the oscillations result completely damped after 1.5 s.

In conclusion, this control system that utilizes the motor to reduce the free oscillations results quite effective. Naturally, in order to be effective also in other orientations, a contact point between the transition area of the boom and the coiled part need to be always present in order to exploit its elastic properties. To do so, a roller with a very soft spring could be employed to keep it in that position. Further tests would be needed to find a relationship between the various components of the controller (PID control coefficients, θ, m_{tip}, etc.).

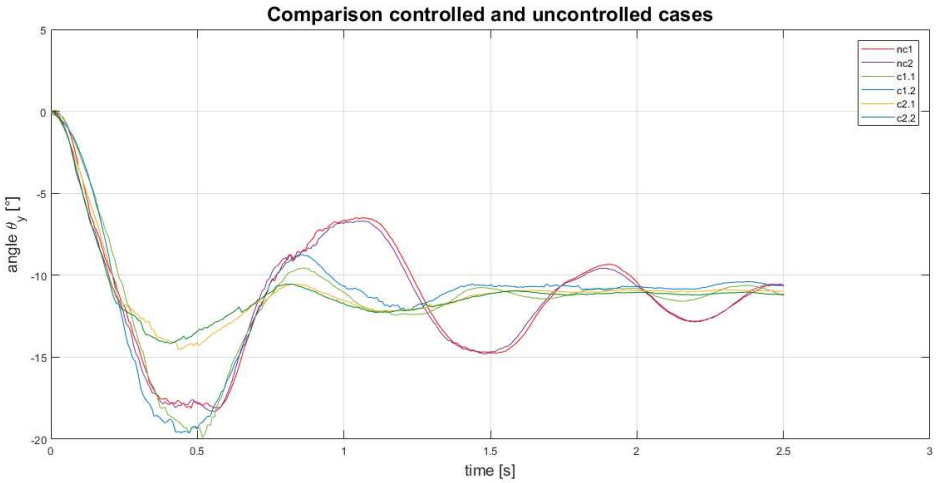

Figure 4.33: Comparison between uncontrolled case (nc1 and nc2) and controlled case 1 (c1.1 and c1.2) and controlled case 2 (c2.1 and c2.2).

Chapter 5

Conclusions

The aim of this dissertation has been (1) to study the dynamic behavior of highly flexible space structures as well as the effects that these deployable structures have on the dynamics of the whole satellite, and (2) to investigate the effectiveness of possible methods to control their oscillations, both in terms of damping techniques directly applied to the appendage, and vibrations transmission reduction at the interface between the deployed structure and the main body of the satellite. Two test cases have been examined in this work, both focusing on membrane solar panels.

The *first test case* investigated the behavior of a non-tensioned membrane not supported by an external structure. This membrane was subjected to a sinusoidal force on the order of magnitude of typical forces that can be experienced LEO, and non-flat initial conditions. Reducing the oscillations of the membrane would reduce possible disturbance transmissions to the central body of the satellite. Numerical simulations studied the effectiveness of controlling the oscillations using thin patches of piezoelectric material as actuators. This first study confirmed the feasibility of applying the robust H_∞ closed-loop algorithm to actuate a set of piezoelectric patches distributed on the surface of the membrane, in order to correct its initial bended shape and reach a flat deployed configuration. The results of the simulations suggested that applying such a control system to counteract the applied disturbance forces is feasible, and the forces that can be exerted by the actuators are sufficient to reduce the oscillations. In particular, varying the length and thickness of the panels in the simulations, two typical behaviors were identified. In the first case, when short and thick membranes were simulated, the results suggested that the

intrinsic damping and elastic behavior of the material is sufficient to counteract the applied external disturbances. On the contrary, when a thinner and longer panel is considered, the piezoelectric patches have more influence in the dynamic behavior of the membrane, and are an effective means to reach a flat deployed configuration in a reduced amount of time compared to a non controlled case.

The *second test case* examined the dynamics of a solar array structure deployed and kept in tension by two external composite tape springs. This structural element has two stable configurations: rolled-up and deployed. The spontaneous transformation between the coiled and the extended configuration can be triggered by mechanical loading. First, c-shaped bistable boom prototypes have been manufactured and their theoretical dynamic behavior was studied in detail from a mathematical perspective. In particular, after obtaining the ABD matrix that links the stresses and strains of a composite laminate, it was possible to calculate some physical quantities that were subsequently compared to the results of numerical simulations and experimental tests, such as forces and torques that are experienced by the tape spring or can be transmitted to an external structure, in particular during the deployment phase. Then, three preliminary tests on the boom prototypes were carried out to study:

1. the elastic and damping properties of the prototypes, exciting the first mode of vibration (bending) and studying the evolution of the oscillations. These data were needed to subsequently simulate the boom with a multibody simulator.

2. the torques needed to be exerted by a motor to perform deployments and retractions, keeping one boom's side fixed and sensing the resulting force with a load cell. This was needed for evaluating which motor to use for the experimental tests.

3. the torques transmitted to an external structure at the end of an uncontrolled deployment, when a shock load occurs. This result was used later in simulations of the behavior of a cubesat in LEO, taking into account the effects of the deployment on such a small-size satellite.

The outcomes of the numerical simulations mentioned in 3) confirmed the con-

cern that fast and uncontrolled deployment of deployable appendages on a nanosatellite. In particular, two torques components due to the deployment were identified: the torques due to the rotational elements (spools, shafts) where the booms and the membranes are wrapped, and the shock load at the end of the deployment. As predicted, an attitude control system that could exert limited torques (up to 0.1 mNm for each axis, a typical value for cubesat reaction wheels) saturates immediately, and it is not sufficient to counteract the torques that arise during the deployment, and this leads to uncontrolled rotations and mission failure. On the contrary, during a motorized smooth and slow deployment, disturbance torques can be counteracted efficiently with the considered control system, and the attitude of the satellite is not affected. Although mass and complexity is added to the system, this approach brings many benefits such as disturbance reduction and the possibility of retracting the deployed structure whenever needed.

Moreover, the effectiveness of two different strategies to control the oscillations of the booms was studied, respectively following a numerical and an experimental approach. The first case was based on the results of the first preliminary test. In these multibody simulations, the boom was replicated as series of masses (to take into account the mass and shape) and rotational joints (to simulate the elasticity and damping of the material) fixed on one side and free on the other. This study confirmed the feasibility of damping boom oscillations applying a force to counteract them near the boom's fixed side (where a real actuator can be placed) with a PD control loop. Damping the oscillations directly on the appendage would reduce the transmission of vibration to the central body of the spacecraft. The second, experimental approach studied the feasibility of an oscillation reduction with a PID directly applied to the motor, that was used as control actuator. The tape spring was forced to oscillate around its equilibrium position, while the motor provided slight and controlled extensions and retractions of the boom to counteract the oscillations. The results highlighted the feasibility of reducing the oscillations deploying or retracting the boom with a small number of motor steps.

The experimental tests presented in Chapter 4 refer to the analysis of the dynamic behavior of the system during uncontrolled deployments as well as controlled

extensions and retractions of a dummy solar panel (a kapton foil tensioned by means of the tape springs and fixed at the tip end). The effectiveness of vibration transmission reduction by means of passive dampers positioned at the interface between the deployer and an external structure was also investigated. The system was suspended with long cables and fly beams, to reduce the effect of gravity during the tests. The dynamic behavior of the system was recorded using two MEMS sensors that included a 3-axis accelerometer and gyroscope and processed with an Arduino Uno. Two uncontrolled cases were identified:

1. with final shock load: this resulted in axial oscillations of the boom, with accelerations frequencies spread in a broad frequency spectrum. Shock loads were noticed to occur only when the structure was released short time after being rolled up.

2. without final shock load: the boom did not have enough deployment force to fully self-extend. This happened because the tests were done many months after manufacturing the booms and viscoelastic relaxations became very influent. Also in this case, the accelerations were spread in a broad frequency spectrum, but without the peak relative to the oscillations due to the shock load at the end of the deployment.

In these two cases the passive rubber dampers were able to reduce the vibrations experienced by the external structure during the deployment phase by about half the intensity. Other tests were performed with a motorized deployment, using a small stepper motor. This controlled case showed a very smooth deployment (in 420 s), where the dominant frequency of oscillations was the one relative to the motor. In this case, the small amplitude vibrations generated by the motor during controlled deployment were reduced very efficiently with small and inexpensive passive dampers.

In conclusion, the work presented in this thesis analyzed the behavior of two deployable structures and their possible control systems. For what concerns the first test case, further work includes the experimental testing of the feasibility the control system based on piezoelectric patches, on a long and thin membrane. Regarding the

second test case, the simulations relative to Section 3.5 could be expanded varying the different parameters that were assumed for the study (orbit, shape of the different elements of the cubesat, deployment time...) and adding the possibility to the membranes to oscillate with respect to the central body and study how possible maneuvers of the small spacecraft can affect the dynamics of large appendages. Moreover, the simulations presented in Section 3.6 relative to the damping of oscillations of the boom by applying a control force directly on it could be further validated with the computation of the control law that relates the control input (application point, intensity) to the external disturbance.

Appendix A

Dynamic Model Formulation

In this section, the boom with its deployer is considered for writing the dynamic equations of the system. Considering the model in Figure A.1, that shows the boom partially wrapped and partially deployed, with a tip mass m_0, a deployed mass m_1 and wrapped mass m_2, where x is the only state variable of the system, that corresponds to the instantaneous deployed length of the boom, the two driving moments are given by:

- the driving motor provides the positive moment, T_m;
- the coiled portion of the boom provides strain energy per unit length along x direction due to its wrapping, U_w, and its flattening, U_f on the storage reel.

The following assumptions were made:

- the boom is tightly wrapped on the storage reel at all times;
- frictions are neglected;

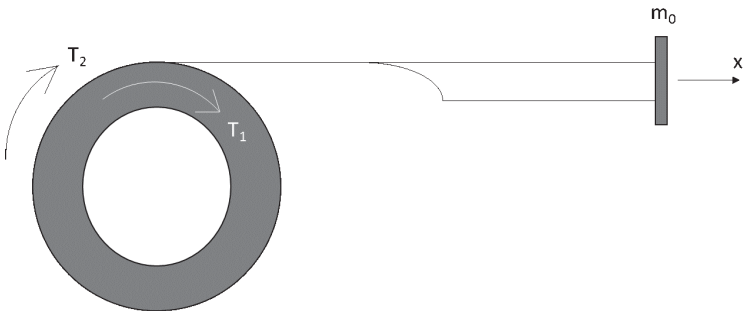

Figure A.1: Schematics of the components of the considered system.

- relaxation of the composite material over time, creep and hysteresis are neglected.

Lagrange Equations can be written as:

$$\frac{d}{dt}\left[\frac{\partial \mathcal{L}(x)}{\partial \dot{x}}\right] - \frac{\partial \mathcal{L}(x)}{\partial x} = Q \tag{A.1}$$

where $\mathcal{L}(x) = E(x) - U(x)$ with $E(x)$ corresponding to the kinetic energy and $U(x)$ to the potential energy of the system, and Q corresponds to the external moment provided by the motor T_m.

The total kinetic energy of the system consists of three parts:

- the kinetic energy of the tip mass, given by $E_0 = \frac{1}{2} m_0 \dot{x}^2$;
- the kinetic energy of the deployed portion of the boom, given by $E_1 = \frac{1}{2} m_1 \dot{x}^2$;
- the rotational kinetic energy of the storage reel, $E_{rot} = \frac{1}{2} J \left(\frac{\dot{x}}{R_x}\right)^2$.

Summing the three components, the total kinetic energy results:

$$E(x) = \frac{1}{2}(m_0 + m_1)\dot{x}^2 + \frac{1}{2} J \left(\frac{\dot{x}}{R_x}\right)^2 \tag{A.2}$$

In this equation, m_0 is the only constant parameter, while m_1, J and R_x are functions of x:

$$m_1(x) = \rho x \tag{A.3}$$

$$m_2(x) = \rho(L_b - x) \tag{A.4}$$

$$R_x(x) = R_0 + \frac{L_b - x}{2\pi R_0}\, t \tag{A.5}$$

$$J(x) = \frac{1}{2} m_2(x)(R_x(x)^2 + R_0^2) + J_0 \tag{A.6}$$

where ρ is the linear density of the boom along x, L_b is the total length of the boom, R_0 is the radius of the storage reel, t is the thickness of the boom, the first

term of $J(x)$ is the inertia moment of wrapped part and the second term is the polar inertia moment of the storage reel. Substituting the last equations in E, the final kinematic energy equation becomes:

$$E = \frac{1}{2} M_0(x) \dot{x}^2 \tag{A.7}$$

where $M_0(x)$ corresponds to the generalized mass of the system:

$$M_0(x) = m_0 + \rho x + \rho(L_b - x)\Big(\frac{R_x^2 + R_0^2}{2R_x^2}\Big) + \frac{J_0}{R_x^2} \tag{A.8}$$

The potential energy $U(x)$ of the system consists of two terms: the strain energy of the coiled portion of the boom, divided in wrapped strain energy (U_w) and flattened strain energy (U_f). The stored strain energy is stored only in the coiled part of the boom, as it can be demonstrated below. According to [44], the wrapped strain energy (U_w) and flattened strain energy (U_f) can be written as:

$$\frac{dU_x}{dl} = \frac{1}{2}\beta R\left[D_{11}\kappa_x^2 + 2D_{12}\kappa_x\left(\kappa_y - \frac{1}{R}\right) + D_{22}\left(\kappa_y - \frac{1}{R}\right)^2\right] \tag{A.9}$$

$$\frac{dU_y}{dl} = \frac{A_{11}}{2}\left[\frac{\beta R}{2}\left(\frac{\kappa_x^2}{\kappa_y^2}\right) + \frac{\sin(\beta R\kappa_y)}{2}\left(\frac{\kappa_x^2}{\kappa_y^3}\right) - \frac{4\sin^2(\beta R\kappa_y/2)}{\beta R}\left(\frac{\kappa_x^2}{\kappa_y^4}\right)\right] \tag{A.10}$$

where A_{11}, D_{11}, D_{12} and D_{22} are constant terms calculated in the ABD matrix, β is the angle subtended by the boom and R is its radius of curvature in its deployed configuration, κ_x and κ_y correspond to the curvature radii and l is the infinitesimal portion of the length. This notation is shown in Figures 3.5 and 3.6.

The total potential energy stored in the coiled portion of the boom is computed applying superposition, hence summing the two equations above:

$$\frac{dU}{dl} = \frac{dU_x}{dl} + \frac{dU_y}{dl} \tag{A.11}$$

The next step consists of integrating the equations over the length of the boom to calculate the total potential energy:

$$U(l) = \int_0^{L_b} \frac{\partial U}{\partial l} dl = \int_0^{L_b} \left(\frac{\partial U_x}{\partial l} + \frac{\partial U_y}{\partial l}\right) dl \tag{A.12}$$

This equation can be divided in two parts, related to the two different portions of the boom: coiled and deployed, where x corresponds to the length of the deployed part of the boom.

$$U(l) = \int_0^{L_w} \left(\frac{\partial U_x}{\partial l} + \frac{\partial U_y}{\partial l} \right) dl + \int_{L_w}^{L_b} \left(\frac{\partial U_x}{\partial l} + \frac{\partial U_y}{\partial l} \right) dl \tag{A.13}$$

where $L_w = L_b - x$ corresponds to the wrapped portion of the boom. Assuming that in the coiled part of the boom $R_y \longrightarrow \infty$, i.e. $\kappa_y \longrightarrow 0$, it is possible to approximate $\sin(\alpha) \approx \alpha$, and therefore equation A.10 becomes:

$$\frac{dU_y}{dl}(\kappa_y \longrightarrow 0) = \frac{A_{11}}{2} \left[\frac{\beta R}{2} \left(\frac{\kappa_x^2}{\kappa_y^2} \right) + \frac{\beta R}{2} \left(\frac{\kappa_x^2}{\kappa_y^2} \right) - \beta R \left(\frac{\kappa_x^2}{\kappa_y^2} \right) \right] = 0 \tag{A.14}$$

where the sum of the terms inside the parentheses is 0. Hence, the

$$U(l) = \int_0^{L_w} \left(\frac{\partial U_x}{\partial l} \right) dl + \int_{L_w}^{L_b} \left(\frac{\partial U_x}{\partial l} + \frac{\partial U_y}{\partial l} \right) dl = P(l) + Q(l) \tag{A.15}$$

Considering now the expression for $Q(l)$ that corresponds to the deployed configuration, the boom has $\kappa_x = 1/R_x = 1/\infty = 0$. Hence, the whole expression inside parentheses in equation A.9 becomes:

$$\frac{dU_x}{dl}(\kappa_x = 0) = \frac{1}{2} \beta R \left[D_{22} \left(\kappa_y - \frac{1}{R} \right)^2 \right] = const. \tag{A.16}$$

Therefore, integrating the expression above, it results:

$$U_x(\kappa_x = 0) = \frac{1}{2} \beta R \left[D_{22} \left(\kappa_y - \frac{1}{R} \right)^2 \right] [L_b - (L_b - x)] = \frac{1}{2} \beta R \left[D_{22} \left(\kappa_y - \frac{1}{R} \right)^2 \right] x \tag{A.17}$$

This expression becomes 0 in the deployed part of the boom because $\kappa_y = 1/R$ and the expression:

$$\kappa_y - \frac{1}{R} = 0 \tag{A.18}$$

$$\frac{dU_y}{dl}(\kappa_x = 0) = \frac{A_{11}}{2} \left[\frac{\beta R}{2} \left(\frac{\kappa_x^2}{\kappa_y^2} \right) + \frac{\beta R}{2} \left(\frac{\kappa_x^2}{\kappa_y^2} \right) - \beta R \left(\frac{\kappa_x^2}{\kappa_y^2} \right) \right] = 0 \tag{A.19}$$

This procedure demonstrates that the deployed portion of the boom has no stored energy, which is stored in the coiled portion and released during the deployment. Analyzing now the first integral $P(l)$ of the equation above, where $R_y \to \infty$, i.e. $\kappa_y \to 0$, and $\kappa_x = 1/R_x = f(x)$ because $R_x(x)$ is given by equation:

$$R_x(x) = R_0 + \frac{L_b - x}{2\pi R_0} t = R_0 + \frac{L_b - x}{R_0} k_0 \tag{A.20}$$

$$k_0 = \frac{t}{2\pi} \tag{A.21}$$

it results:

$$\begin{aligned} U(l) = \int_0^{L_w} \left(\frac{\partial U_x}{\partial L}\right) dl &= \int_0^{L_w} \frac{\beta R}{2} \left[D_{11}\kappa_x^2 - 2\frac{D_{12}}{R}\kappa_x + \frac{D_{22}}{R^2} \right] dl \\ &= \int_0^{L_w} \frac{\beta R}{2} \left[D_{11}\left(\frac{1}{R_x}\right)^2 - 2\frac{D_{12}}{R}\frac{1}{R_x} + \frac{D_{22}}{R^2} \right] dl \end{aligned} \tag{A.22}$$

Introducing the constants:

$$k_1 = \frac{\beta R D_{11}}{2} \tag{A.23}$$

$$k_2 = \beta D_{12} \tag{A.24}$$

$$k_3 = \frac{\beta D_{22}}{2R} \tag{A.25}$$

the equation to be integrated becomes:

$$U(l) = \int_0^{L_w} \left[k_1 \left(\frac{1}{R_x}\right)^2 - k_2 \left(\frac{1}{R_x}\right) + k_3 \right] dl \tag{A.26}$$

Integrating the expression above it results:

$$\begin{aligned} U(l) = &\left[-\frac{k_1 R_0^2}{k_0(k_0 l + R_0^2)} - \frac{k_2 R_0 \log(k_0 l + R_0^2)}{k_0} + k_3 l \right]_0^{L_w = L_b - x} \\ = &-\frac{k_1 R_0^2}{k_0(k_0(L_b - x) + R_0^2)} - \frac{k_2 R_0 \log(k_0(L_b - x) + R_0^2)}{k_0} + k_3(L_b - x) \\ &+ \frac{k_1 R_0^2}{k_0 R_0^2} + \frac{k_2 R_0 \log(R_0^2)}{k_0} \end{aligned} \tag{A.27}$$

The first three terms of the equation depend on the variable x, while the rest of the equation is a constant value, K. Hence, the final equation for the potential energy as a function of x can be written as:

$$U(x) = -\frac{k_1 R_0^2}{k_0(k_0(L_b - x) + R_0^2)} - \frac{k_2 R_0 \log(k_0(L_b - x) + R_0^2)}{k_0} + k_3(L_b - x) + K \tag{A.28}$$

where

$$K = \frac{k_1 R_0^2}{k_0 R_0^2} + \frac{k_2 R_0 \log(R_0^2)}{k_0} \tag{A.29}$$

Going back to the Lagrangian equation:

$$\frac{d}{dt}\left[\frac{\partial(E-U)}{\partial \dot{x}}\right] - \frac{\partial(E-U)}{\partial x} = Q \tag{A.30}$$

where the derivative of the potential energy with respect to the deployment rate $\dot{x}$ is:

$$\frac{\partial U}{\partial \dot{x}} = 0 \tag{A.31}$$

the derivative of the potential energy with respect to the state variable x is:

$$\frac{\partial U}{\partial x} = \frac{k_0^2 k_1 R_0}{(k_0^2(L_b - x) + R_0^2)^2} - \frac{k_2 R_0}{k_0((L_b - x) + R_0^2)} - k_3 \tag{A.32}$$

the derivative of the kinetic energy with respect to the deployment rate $\dot{x}$ is:

$$\frac{\partial E}{\partial \dot{x}} = M_0(x)\ddot{x} \tag{A.33}$$

while the derivative of the kinetic energy with respect to the state variable x is:

$$\frac{\partial E}{\partial x} = \frac{1}{2}\frac{\partial M_0(x)}{\partial x}\dot{x}^2 \tag{A.34}$$

Expanding $\frac{\partial M_0(x)}{\partial x}$ it results:

$$\frac{\partial M_0(x)}{\partial x} = \rho + \rho\frac{\partial}{\partial x}\left[(L_b - x)\left(\frac{R_x^2 + R_0^2}{2R_x^2}\right)\right] + J_0\frac{\partial}{\partial x}\left[\frac{1}{R_x^2}\right] \tag{A.35}$$

The second term, substituting $R_x(x)$ with its full expression, becomes:

$$\frac{\partial}{\partial x}\left[(L_b - x)\Big(\frac{R_x^2 + R_0^2}{2R_x^2}\Big)\right] = \frac{R_0^6}{(-k_0 L_b + k_0 x - R_0^2)^3} + \frac{R_0^4}{2(-k_0 L_b + k_0 x - R_0^2)^2} - \frac{1}{2} \tag{A.36}$$

The derivative of the third term becomes:

$$\frac{\partial}{\partial x}\left[\frac{1}{R_x(x)^2}\right] = \frac{2k_0 R_0^2}{(k_0(L_b - x) + R_0^2)^3} \tag{A.37}$$

In conclusion, the final expression of the Lagrange equations is:

$$M_0(x)\ddot{x} + \frac{1}{2}\frac{\partial M_0(x)}{\partial x}\dot{x}^2 - \left[\frac{k_0^2 k_1 R_0}{(k_0^2(L_b - x) + R_0^2)^2} - \frac{k_2 R_0}{k_0((L_b - x) + R_0^2)} - k_3\right] = Q \tag{A.38}$$

where Q can be written as:

$$Q = \frac{T_m}{R_m} \tag{A.39}$$

with R_m the radius of the gear that drives the spool where the boom is wrapped.

Appendix B

Morphing

Preliminary Matlab® simulations have been performed to evaluate the feasibility of controlling the attitude of a 3U CubeSat subjected to typical orbital disturbances in LEO through morphing, i.e. changing the size of the solar panels ideally rolling and unrolling them with a motor.

A 3U CubeSat was considered in these simulations, with a central body of 0.3 x 0.1 x 0.1 m^3 of volume and two solar arrays 0.3 x 1 m^2 in area (see Figure B.1) with a thickness of 6.7E-4 m to distribute the mass of the external frame on the whole solar panels area. The system was simplified by means of 3 rigid bodies connected rigidly to each other. The system is very similar to the one described and simulated in Section 3.5.

Also in this case, the three main orbital disturbances have been considered: solar radiation pressure, drag force and gravity gradient. To avoid motion singularities, the quaternions were used in the simulations to describe the attitude of the system.

In these simulations, for simplicity only one of the two solar arrays length was variable, but in principle using both panels, they would have to respectively roll and unroll of half the length that would be needed with only one solar array. Ideally rolling or deploying the panel would allow the control of the ϕ angle around x axis. The motion around θ and ψ, corresponding to rotations respectively around x and z axes, is controlled by two small reaction wheels. A customized PD controller was implemented to perform the control around the three axes and the control scheme can be seen in B.2.

The idea at the base of the control through morphing is based on the compen-

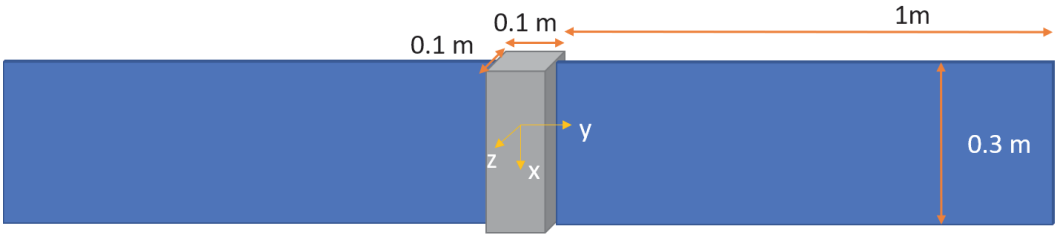

Figure B.1: Morphing - initial configuration of the system.

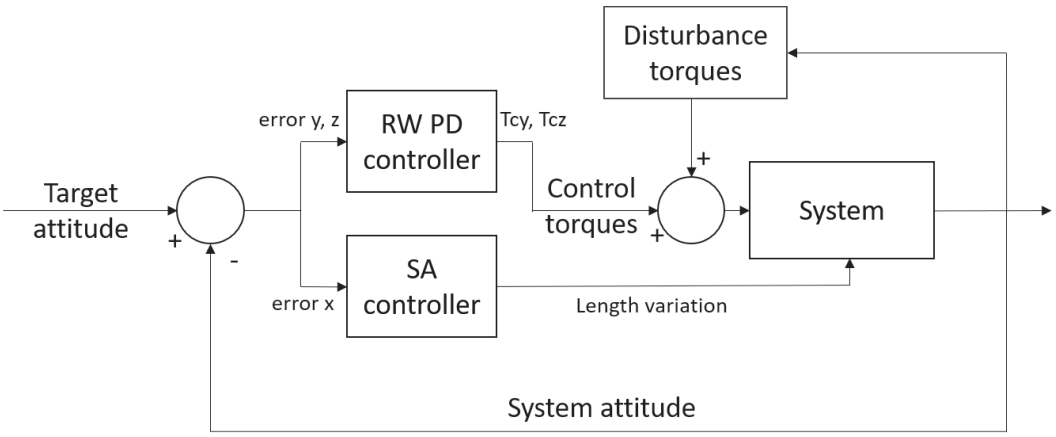

Figure B.2: PD controller scheme, where SA = solar array and RW = reaction wheels.

sation of the orbital disturbances with the variation of the length of the panel, that causes also a change in the moments of inertia of the entire system. A minimum and a maximum length respectively of 0.8 m and 1.2 m were imposed on the controller.

The selected orbit was a circular equatorial orbit at 500 km of altitude with the respective orbital disturbances. As in Section 3.5, the satellite was placed with such an attitude that the disturbances compensate and ideally do not generate any disturbance on the center of mass of the satellite. In this case, the inertial attitude would be $\phi = \theta = \psi = 0$ in all the axes.

The results of an example maneuver are now presented. In this case, the initial attitude of the satellite is zero along all the three axes, and the final desired attitude is ϕ_{obj}=10°, θ_{obj}=5° and ψ_{obj}=5°. The attitude in terms of angles and angular velocities is shown in Figure B.3. The angles corresponding to a rotation around the x axis are influenced by the variation in solar radiation pressure between the periods of Sun illumination and umbra, with a small variation of about 2°.

Since the attitude along x axis is highly influenced by the contribution of the solar radiation pressure and the atmospheric resistance, a customized PD controller was designed to more efficiently counteract these disturbances. In particular, from the equation of the solar radiation pressure and the drag, a coefficient K3 was estimated as follows:

$$K3 = 1.7 \cdot (0.5 \cdot d \cdot v^2 \cdot Cd)/(P_{rad}); \tag{B.1}$$

where d is the atmospheric density at that altitude, v is the velocity of the satellite in the direction of motion, Cd is the drag coefficient and P_{rad} is the solar radiation pressure. Two other gains were used:

$$\begin{aligned} K1 &= K10 \cdot (1 - K3 \cdot \sin(\omega_0 t - \phi_{obj})) \\ K2 &= K20 \cdot (1 - K3 \cdot \sin(\omega_0 \cdot t - \phi_{obj})) \end{aligned} \tag{B.2}$$

where K10 and K20 were two constant multipliers, ω_0 was the orbital velocity and t was the time. Considering the error in attitude:

$$\Delta\phi = (\phi - \phi_{obj}) \tag{B.3}$$

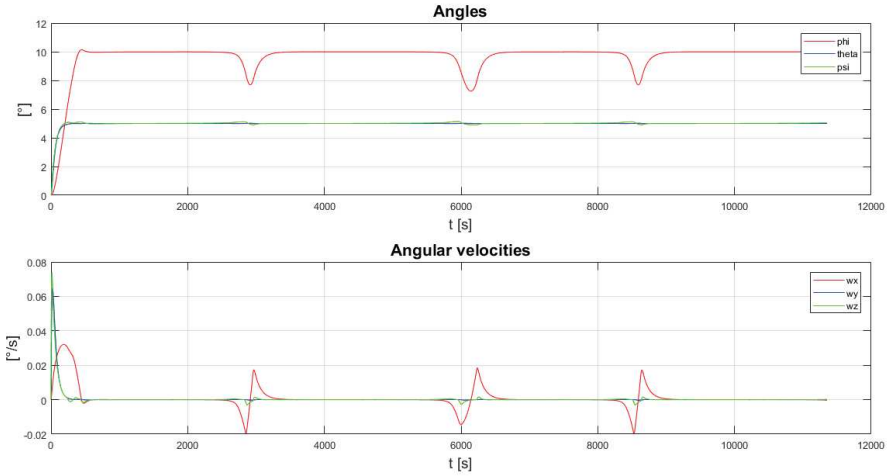

Figure B.3: Attitude of the system along the three axes.

the resulting instantaneous length l of the solar array was:

$$l(t) = l(t-1) - K1 \cdot \Delta\phi - K2 \cdot \omega_0^{bix}; \tag{B.4}$$

where ω_0^{bix} is the component around x of the angular velocity in the inertial frame. In addition, the value of l(t) was constrained between a maximum and minimum value. The variation of the length of the panel during the example maneuver is shown in B.4. In addition, the control torques relative to the reaction wheels, computed with a simple PD controller, are shown on the chart on the top in Figure B.5, while the disturbance torques due to the orbital environment are shown in the chart on the bottom. The single contribution of these external torques to the attitude of the satellite can be seen in Figures B.6, B.7 and B.8 respectively for the drag torques due to the atmospheric resistance on the two panels, the gravity gradient contribution on the center of mass, and the solar radiation pressure, where the effects of the illuminated and the umbra period are considered.

The results showed that changes in the length of one of the two panels could help in performing (mostly) small angles maneuvers, with the compensation of disturbances given by the external environment (solar radiation pressure, drag, gravity gradient).

Running a number of simulations varying the target attitude, with an initial orientation of the satellite of (0, 0, 0) around the three axes, acceptable combinations

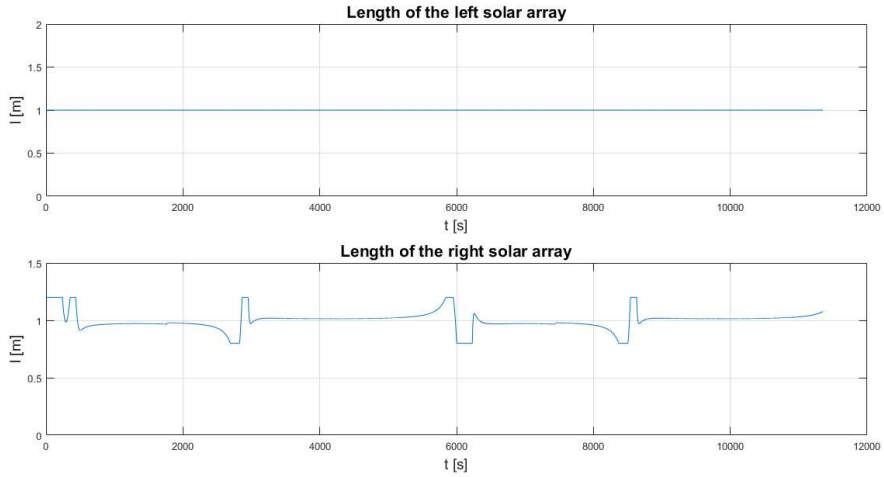

Figure B.4: Length of the panels during two orbits.

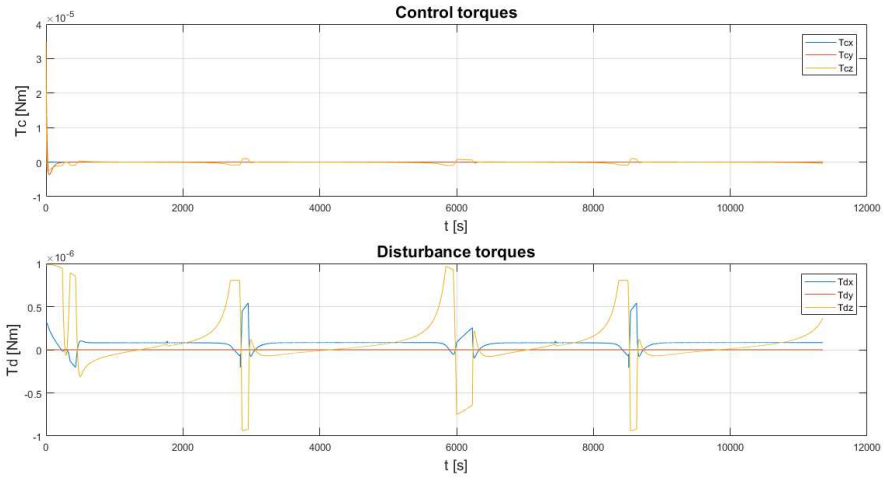

Figure B.5: Control torques and disturbance torques during two orbits

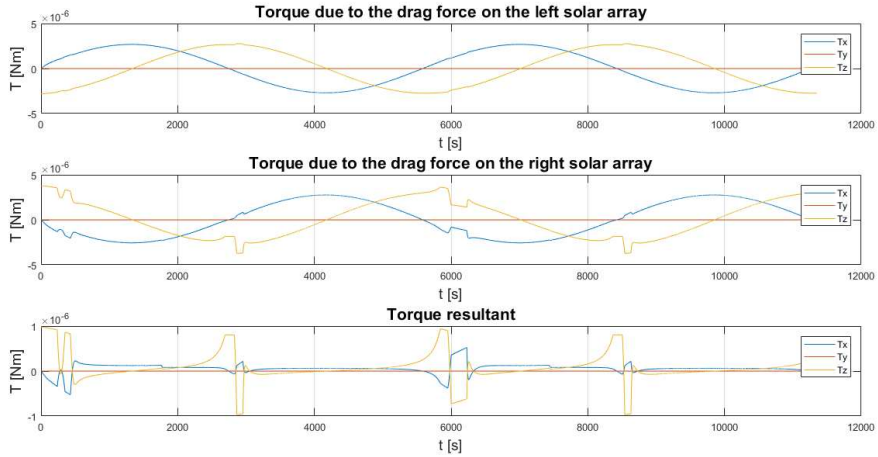

Figure B.6: Drag during two orbits.

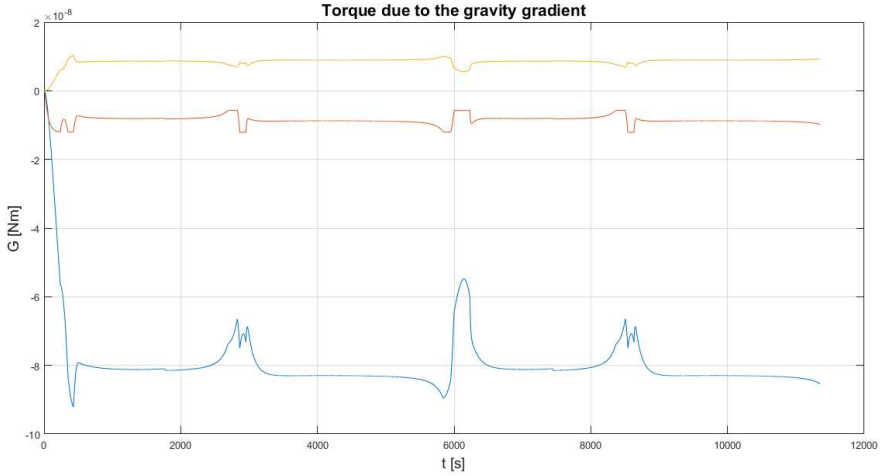

Figure B.7: Gravity gradient during two orbits.

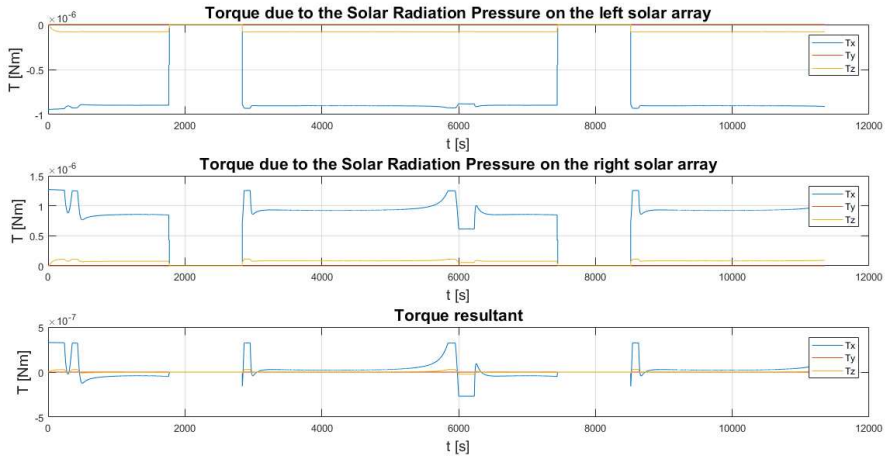

Figure B.8: Solar radiation pressure during two orbits.

of target angles (where also the maximum possible reaction wheels torques are T_{RW}^{max} = 0.1 mNm on the y and z axes) can be found when these limitations apply:

- imposing a maneuver where $\phi_{obj} \geq 0°$:
  - if θ_{obj} and $\psi_{obj} \geq 0°$, the maximum values for a stable maneuver are: $0° \leq \phi_{obj} < 12°$ and $0° \leq \theta_{obj}, \psi_{obj} \leq 3°$.
  - if θ_{obj} and $\psi_{obj} < 0°$, the maximum values for a stable maneuver are: $0° \leq \phi_{obj} \leq 60°$ and $-15° \leq \theta_{obj}, \psi_{obj} < 0°$.
- imposing a maneuver where $\phi_{obj} < 0°$:
  - if θ_{obj} and $\psi_{obj} \geq 0°$, the maximum values for a stable maneuver are: $-10° \leq \phi_{obj} < 0°$ and $0° \leq \theta_{obj}, \psi_{obj} \leq 14°$.
  - if θ_{obj} and $\psi_{obj} < 0°$, the maximum values for a stable maneuver are: $-3° \leq \phi_{obj} < 0°$ and $0° < \theta_{obj}, \psi_{obj} \leq -5°$.

Naturally, there can be an infinite number of configurations, varying the initial and target angles, control coefficients, maximum and minimum length of the controlled solar array, maximum allowed reaction wheels torques and orbital altitude. This section wants to demonstrate that there are some circumstances in which this low-order control can be effective, with only control of the the length of a panel to

perform simple maneuvers with the compensation of the external disturbances. This is especially true when applied on a satellite where high tolerances on its attitude are accepted.

Bibliography

[1] W Keith Belvin, Marco Straubel, W Keats Wilkie, Martin E Zander, Juan M Fernandez, and Martin F Hillebrandt. Advanced deployable structural systems for small satellites. 2016.

[2] Spacex - capabilities & services, `http://www.spacex.com/about/capabilities`, retrieved on 12.07.2017.

[3] Arianespace aims high in asia-pacific, `https://www.flightglobal.com/news/articles/arianespace-aims-high-in-asia-pacific-425928/`, retrieved on 08.08.2017.

[4] Christopher HM Jenkins. *Progress in astronautics and aeronautics: gossamer spacecraft: membrane and inflatable structures technology for space applications*, volume 191. AIAA, 2001.

[5] Sheila Bailey and Ryne Raffaelle. Space solar cells and arrays. *Handbook of Photovoltaic Science and Engineering*, pages 413–448, 2003.

[6] Ashok Chaudhari. Cigs/silicon thin-film tandem solar cell, 2016. US Patent App. 15/238,050.

[7] M Hall. Empa announces 20.4% efficient thin film cigs-on-polymer cell. *PV magazine*, 21, 2013.

[8] Martin A Green, Yoshihiro Hishikawa, Wilhelm Warta, Ewan D Dunlop, Dean H Levi, Jochen Hohl-Ebinger, and Anita WH Ho-Baillie. Solar cell efficiency tables (version 50). *Progress in Photovoltaics: Research and Applications*, 25(7):668–676, 2017.

[9] How hubble got its wings, http://www.esa.int/Our_Activities/Space_Engineering_Technology/How_Hubble_got_its_wings, retrieved on 12.07.2017.

[10] Mark S Grahne and David P Cadogan. Inflatable solar arrays: revolutionary technology? Technical report, SAE Technical Paper, 1999.

[11] John Huang. The development of inflatable array antennas. *IEEE Antennas and Propagation Magazine*, 43(4):44–50, 2001.

[12] Michael Lou, Houfei Fang, and Lih-Min Hsia. Self-rigidizable space inflatable boom. *Journal of spacecraft and rockets*, 39(5):682–690, 2002.

[13] Eni G Njoku, Yahya Rahmat-Samii, J Sercel, William J Wilson, and Mahta Moghaddam. Evaluation of an inflatable antenna concept for microwave sensing of soil moisture and ocean salinity. *IEEE Transactions on Geoscience and Remote Sensing*, 37(1):63–78, 1999.

[14] David P Cadogan and Mark S Grahne. Deployment control mechanisms for inflatable space structures. In *33rd aerospace mechanisms conference*, volume 5, pages 1–12, 1999.

[15] David Lichodziejewski, Gordon Veal, Richard Helms, Robert Freeland, and Mark Kruer. Inflatable rigidizable solar array for small satellites. *AIAA-2003-1898*, 2003.

[16] Roll-out solar array (rosa), https://www.nasa.gov/mission_pages/station/research/experiments/2139.html, retrieved on 21.10.2017.

[17] Rosa flight demonstration hardware successfully deploys on iss, http://www.dss-space.com/post/rosa-flight-demonstration-hardware-successfully-deploys-on-iss, retrieved on 21.10.2017.

[18] Zayan Guedim. Nasa tests flexible solar array, rosa, on iss for future solar propulsion, https://edgylabs.com/iss-rosa-nasa-solar-array-future-propulsion/, retrieved on 25.09.2017.

[19] Brian R Spence and Stephen F White. Directionally controlled elastically deployable roll-out solar array, April 1 2014. US Patent 8,683,755.

[20] Bao Hoang, Steve White, Brian Spence, and Steven Kiefer. Commercialization of deployable space systems' roll-out solar array (rosa) technology for space systems loral (ssl) solar arrays. In *Aerospace Conference, 2016 IEEE*, pages 1–12. IEEE, 2016.

[21] Hirotaka Sawada, Yoji Shirasawa, Osamu Mori, Nobukatsu Okuizumi, Yasuyuki Miyazaki, Saburo MATUNAGA, Hiroshi Furuya, Hiraku Sakamoto, Michihiro Natori, and Yuichi Tsuda. On-orbit result and analysis of sail deployment of world's first solar power sail ikaros. *The Journal of Space Technology and Science*, 27(1):1_54–1_68, 2013.

[22] Andrzej mirecki (`https://commons.wikimedia.org/wiki/File:IKAROS_solar_sail.jpg`), "ikaros solar sail", `https://creativecommons.org/licenses/by-sa/3.0/legalcode`.

[23] Joachim Block, Marco Straubel, and Martin Wiedemann. Ultralight deployable booms for solar sails and other large gossamer structures in space. *Acta Astronautica*, 68(7):984–992, 2011.

[24] Juan M Fernandez, Lourens Visagie, Mark Schenk, Olive R Stohlman, Guglielmo S Aglietti, Vaios J Lappas, and Sven Erb. Design and development of a gossamer sail system for deorbiting in low earth orbit. *Acta Astronautica*, 103:204–225, 2014.

[25] Marco Straubel. *Design and Sizing Method for Deployable Space Antennas*. PhD thesis, Deutsches Zentrum für Luft-und Raumfahrt eV, 2012.

[26] RE Freeland, GD Bilyeu, GR Veal, MD Steiner, and DE Carson. Large inflatable deployable antenna flight experiment results. *Acta Astronautica*, 41(4):267–277, 1997.

[27] *Piezo Film Sensors Technical Manual, downloaded from* `https://www.sparkfun.com/datasheets/Sensors/Flex/MSI-techman.pdf` *on 28.09.2017.*

[28] Sachin C Gajbhiye, Sanjay H Upadhyay, and Suraj P Harsha. Nonlinear vibration analysis of piezo-actuated flat thin membrane. *Journal of Vibration and Control*, 21(6):1162–1170, 2015.

[29] Zhi-cheng Qiu, Xian-min Zhang, Hong-xin Wu, and Hong-hua Zhang. Optimal placement and active vibration control for piezoelectric smart flexible cantilever plate. *Journal of Sound and Vibration*, 301(3):521–543, 2007.

[30] Zhi-cheng Qiu, Xian-min Zhang, Yue-chao Wang, Zhen-wei Wu, et al. Active vibration control of a flexible beam using a non-collocated acceleration sensor and piezoelectric patch actuator. *Journal of sound and vibration*, 326(3):438–455, 2009.

[31] Zhi-cheng Qiu, Hong-xin Wu, et al. Acceleration sensors based modal identification and active vibration control of flexible smart cantilever plate. *Aerospace Science and Technology*, 13(6):277–290, 2009.

[32] Zhi-cheng Qiu. Experiments on vibration suppression for a piezoelectric flexible cantilever plate using nonlinear controllers. *Journal of Vibration and Control*, 21(2):300–319, 2015.

[33] H Djojodihardjo and M Jafari. Vibration analysis of a cantilevered beam with piezoelectric actuator as a controllable elastic structure, paper iac-14, c2, 3, 8. In *Proceedings, The International Astronautical Congress 2014, Toronto*, 2014.

[34] Hiraku Sakamoto, KC Park, and Yasuyuki Miyazaki. Distributed and localized active vibration isolation in membrane structures. *Journal of spacecraft and rockets*, 43(5):1107–1116, 2006.

[35] Hiraku Sakamoto and KC Park. Localized vibration isolation strategy for low-frequency excitations in membrane space structures. *Journal of vibration and acoustics*, 128(6):790–797, 2006.

[36] Hiraku Sakamoto, KC Park, and Yasuyuki Miyazaki. Evaluation of membrane structure designs using boundary web cables for uniform tensioning. *Acta Astronautica*, 60(10):846–857, 2007.

[37] Xiaoyun Wang, Wanping Zheng, and Yan-Ru Hu. Active flatness control of space membrane structures using discrete boundary sma actuators. In *Advanced Intelligent Mechatronics, 2008. AIM 2008. IEEE/ASME International Conference on*, pages 1108–1113. IEEE, 2008.

[38] Kanjuro Makihara, Junjiro Onoda, and Masahiro Tsuchihashi. Investigation of performance in suppressing various vibrations with energy-recycling semi-active method. *Acta Astronautica*, 58(10):506–514, 2006.

[39] Shota Yamamoto, Yohsuke Nambu, and Masakatsu Chiba. Vibration control for membrane by smart dynamic vibration absorber, paper iac-12, c2, 3, 8. In *Proceedings, The International Astronautical Congress 2012, Naples*, 2012.

[40] Inderjit Chopra and Jayant Sirohi. *Smart structures theory*, volume 35. Cambridge University Press, 2013.

[41] Dimitri Bertsekas. *Dynamic programming and optimal control*, volume 1. Athena scientific Belmont, MA, 1995.

[42] Dupont Technical Information. Dupont^{TM} kapton® polyimide films - high performance flexible films for photovoltaic substrates.

[43] Joseph N Footdale and Thomas W Murphey. Mechanism design and testing of a self-deploying structure using flexible composite tape springs. In *Proceedings of the 42nd Aerospace Mechanisms Symposium, NASA Goddard Space Flight Center, May 14-16, 2014*.

[44] Sergio Pellegrino. *Deployable structures*, volume 412. Springer, 2014.

[45] E Kebadze, SD Guest, and S Pellegrino. Bistable prestressed shell structures. *International Journal of Solids and Structures*, 41(11):2801–2820, 2004.

[46] KA Seffen and S Pellegrino. Deployment dynamics of tape springs. In *Proceedings of the Royal Society of London A: Mathematical, Physical and Engineering Sciences*, volume 455, pages 1003–1048. The Royal Society, 1999.

[47] Thomas W Murphey, William Francis, Bruce Davis, Juan M Mejia-Ariza, Matthew Santer, Joseph N Footdale, Kevin Schmid, Omer Soykasap, Koorosh

Guidanean, and P Warren. High strain composites. In *2nd AIAA Spacecraft Structures Conference*, pages 2015–0942, 2015.

[48] K Iqbal and S Pellegrino. Bi-stable composite shells. In American Institute of Aeronautics and Astronautics, editors, *41st AIAA/ASME/ASCE/AHS/ASC Structures, Structural Dynamics, and Materials Conf. and Exhibit.*

[49] Thomas Murphey, Sungeun Jeon, Adam Biskner, and Gregory Sanford. Deployable booms and antennas using bi-stable tape-springs. 2010.

[50] Andrew J Daton-Lovett. Extendible member, 2001. US Patent 6,217,975.

[51] SD Guest and S Pellegrino. Analytical models for bistable cylindrical shells. In *Proceedings of the Royal Society of London A: Mathematical, Physical and Engineering Sciences*, volume 462, pages 839–854. The Royal Society, 2006.

[52] HMYC Mallikarachchi and S Pellegrino. Deployment dynamics of ultrathin composite booms with tape-spring hinges. *Journal of Spacecraft and Rockets*, 2014.

[53] Douglas S Adams and Mehran Mobrem. Lenticular jointed antenna deployment anomaly and resolution onboard the mars express spacecraft. *Journal of Spacecraft and Rockets*, 46(2):403, 2009.

[54] Kawai Kwok and Sergio Pellegrino. Viscoelastic effects in tape-springs. In *Proceedings of the AIAA/ASME/ASCE/ASC Structures, Structural Dynamics, and Material Conference, AIAA Paper*, volume 2022, 2011.

[55] Mehran Mobrem and Douglas S Adams. Deployment analysis of lenticular jointed antennas onboard the mars express spacecraft. *Journal of Spacecraft and Rockets*, 46(2):394, 2009.

[56] Alex Brinkmeyer, Sergio Pellegrino, and Paul M Weaver. Effects of long-term stowage on the deployment of bistable tape springs. *Journal of Applied Mechanics*, 83(1):011008, 2016.

[57] A Brinkmeyer, S Pellegrino, PM Weaver, and M Santer. Effects of viscoelasticity on the deployment of bistable tape springs. In *19th International Conference on*

Composite Materials (ICCM-19), Montreal, QC, Canada, July, pages 370–380, 2013.

[58] Kawai Kwok and Sergio Pellegrino. Folding, stowage, and deployment of viscoelastic tape springs. *AIAA journal*, 2013.

[59] HM Mallikarachchi. *Thin-walled composite deployable booms with tape-spring hinges*. PhD thesis, University of Cambridge, 2011.

[60] Sungeun Jeon and Thomas W Murphey. Design and analysis of a meter-class cubesat boom with a motor-less deployment by bi-stable tape springs. In *52nd AIAA/ASME/ASCEAHSASC Structures Structural Dynamics and Materials Conference*, 2011.

[61] Thomas W Murphey, Gregory E Sanford, and Sungeun Jeon. Deployable space boom using bi-stable tape spring mechanism, July 8 2014. US Patent 8,770,522.

[62] Pau Mallol and Gunnar Tibert. Deployment modeling and experimental testing of a bi-stable composite boom for small satellites. In *54th AIAA/ASME/ASCE/AHS/ASC Structures, Structural Dynamics and Materials Conference; Boston, MA; United States; 8 April 2013 through 11 April 2013*. American Institute of Aeronautics and Astronautics, 2013.

[63] Huina Mao, Pier Luigi Ganga, Michele Ghiozzi, Nickolay Ivchenko, and Gunnar Tibert. Deployment of bistable self-deployable tape spring booms using a gravity offloading system. *Journal of Aerospace Engineering*, 30(4):04017007, 2017.

[64] Joseph N Footdale and Thomas W Murphey. Structural design of a cubesat-based diffractive optic telescope. In *Proceedings of the AIAA/ASME/ASCE/ASC Structures, Structural Dynamics and Material Conference, AIAA Paper*, volume 1729, 2011.

[65] Joseph N Footdale, Thomas W Murphey, and Michael Peterson. Design and testing of self-deploying membrane optic support structure using rollable composite tape springs. In *Proceedings, 54th AIAA/ASME/ASCE/AHS/ASC Structures, Structural Dynamics, and Materials Conference, Boston, MA*, 2013.

[66] Overview of oss design approach and products, `https://oxford.space/#s-technology`, retrieved on 21.10.2017.

[67] Juan Reveles, Mike Lawton, Vincent Fraux, Vinoth Gurusamy, and Vicky Parry. In-orbit performance of astrotube: Alsat nano's low mass deployable composite boom payload. 2017.

[68] Oxford space systems astrotube boom on remove debris platform, `https://vimeo.com/227410826`.

[69] Juan Reveles, Mike Lawton, Vincent Fraux, and Vinoth Gurusamy. The development of a low mass extendible composite boom for small satellite applications. In *29th AIAA/USU Conference on Small Satellites, Logan, UT, USA*.

[70] Gregg E Freebury, William H Francis, and Neal J Beidleman. Deployment system for supported retractable extension of a composite boom, March 14 2017. US Patent 9,593,485.

[71] Bruce Davis, William Francis, Jonathan Goff, Michael Cross, and Daniel Copel. Big deployables in small satellites.

[72] Jakob Ekelöw. Design and manufacturing of thin composite tape springs. Master's thesis, KTH, School of Engineering Sciences (SCI), Aeronautical and Vehicle Engineering, Aerodynamics., 2014.

[73] Michael W Hyer. *Stress analysis of fiber-reinforced composite materials*. DEStech Publications, Inc, 2009.

[74] Pankar K Mallick. *Fiber-reinforced composites: materials, manufacturing, and design*. CRC press, 2007.

[75] A García-Carpintero, M Herráez, J Xu, CS Lopes, and C González. A multi material shell model for the mechanical analysis of triaxial braided composites. *Applied Composite Materials*, pages 1–21, 2017.

[76] Hexcel. *Datasheet HexTow AS4C*.

[77] Ö Soykasap. Analysis of plain-weave composites. *Mechanics of composite materials*, 47(2):161–176, 2011.

[78] Arduino website, https://www.arduino.cc/, retrieved on 25.09.2017.

[79] Mpu-6000 and mpu-6050 product specification, downloaded from https://store.invensense.com/datasheets/invensense/MPU-6050_DataSheet_V3%204.pdf on 25.09.2017.

[80] Adafruit motor shield v2 for arduino, downloaded from https://cdn-learn.adafruit.com/downloads/pdf/adafruit-motor-shield-v2-for-arduino.pdf on 25.09.2017.

[81] Faulhaber stepper motors am-1524 datasheet, downloaded from https://www.faulhaber.com/fileadmin/Import/Media/EN_AM1524_FPS.pdf, retrieved on 03.10.2017.

[82] Ethylene propylene rubbers – properties and applications of ethylene propylene diene (epdm) and ethylene propylene copolymers (epm), https://www.azom.com/article.aspx?ArticleID=1822, retrieved on 24.10.2017.

[83] Gyula Greschik and W Keith Belvin. High-fidelity gravity offloading system for free-free vibration testing. *Journal of Spacecraft and Rockets*, 44(1):132–142, 2007.